

学位論文

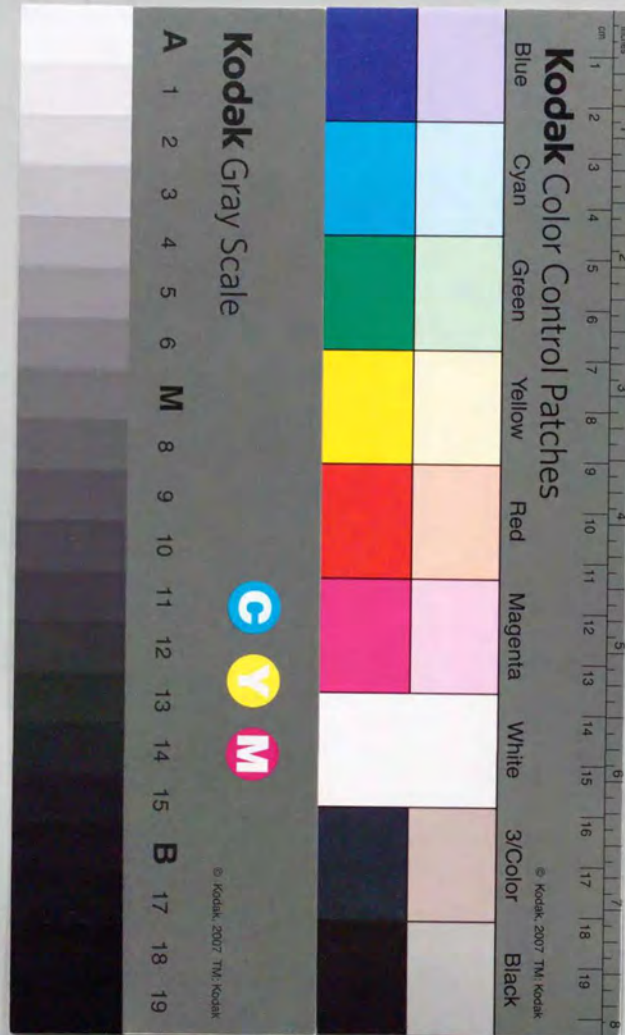
Study of reaction mechanisms for
(p, n) and (p, p') quasi elastic scatterings

(p, n) および (p, p') 準弾性散乱の反応機構の研究

平成 7 年 12 月 博士(理学) 申請

東京大学大学院理学系研究科
物理学専攻

大津 秀暁



Study of reaction mechanisms for
 (p, n) and (p, p') quasi elastic scatterings

Doctoral Thesis

by

Hideaki Otsu



Department of Physics, School of Science,
University of Tokyo
Bunkyo-ku, Tokyo 113, Japan

December, 1995, *revised in* March, 1997

Abstract

This thesis deals with the experiment of quasi elastic scattering using polarized proton beam at around 400 MeV. We have aimed at clarifying the systematic features, such as q dependence or A dependence, of the proton induced quasi elastic scattering by measuring the cross sections and the analyzing powers.

We measured these observables for the (p, n) reaction at 392(295) MeV and for the (p, p') reaction at 400 MeV. From the comparison with these observables for free NN scattering, we have derived the systematic deviations of those for quasi elastic scattering. The peak positions in the cross section spectra systematically shift towards high energy transfer for both the (p, n) and (p, p') reactions. The analyzing powers for the (p, p') reaction are reduced while those for the (p, n) reaction are enhanced.

We have discussed how simple models are able to give satisfactory explanations about these deviations simultaneously. We have tested a framework of the relativistic plane wave impulse approximation. It is found that the framework reproduces the tendency of the deviations qualitatively. We have concluded that the relativistic framework is one of the candidates available to explain simply the mechanism of the measured deviation of the observables for quasi elastic scattering.

Contents

1 Introduction	1
1.1 What is quasi elastic scattering	1
1.2 Response functions of the nucleus	2
1.3 How to probe the modification of the response function experimentally	2
1.4 Historical review	4
1.5 Thesis objectives	6
1.6 Thesis outline	7
2 Experiment and Data analysis	9
2.1 Overview	9
2.2 Experiment	11
2.3 Experimental setup for (p, n) measurement	11
2.4 Data analysis for (p, n) measurement	22
2.5 Experimental setup for the (p, p') measurement	28
2.6 Data analysis for the (p, p') measurement	32
2.7 Systematic errors	42
3 Experimental results	44
3.1 Spectra	44
3.2 Peak position and analyzing power at the peak position	57
4 Discussion	65
4.1 Standard reaction model	65
4.2 Fermi gas model	69
4.3 Kinematic effect of the Fermi motion	77
4.4 Relativistic PWIA	86
5 Summary	93
6 Conclusion	95
Reference	96
Appendix	100
A Response function by the Fermi gas model	100
B Projectile energy dependence of peak shifts by the PWIA calculation	106
C Parameterization of NN amplitude	109
D Expansion of the Glauber theory	111
E Other results : $^{13}\text{C}(p, n)$ reaction	113
Acknowledgement	115

List of Figures

1-1 Expected response of the quasi elastic scattering	1
1-2 Modification of R_L and R_T	3
1-3 Probe dependence of peak positions	5
1-4 Energy dependence of the total NN cross sections	7
2-1 RCNP ring cyclotron facility	10
2-2 Time of flight spectrum of the $^7\text{Li}(p, n)$ reaction at 0°	12
2-3 Beam line polarimeter	14
2-4 Beam polarization	15
2-5 Beam pulsing device	16
2-6 N0 room	18
2-7 Neutron polarimeter system	19
2-8 Circuit for neutron singles event	20
2-9 Schematic view for timing information	23
2-10 Timing monitor results	24
2-11 Calibration of the light outputs of the neutron detectors	25
2-12 Neutron detection efficiency	26
2-13 Subtraction of carbon contribution from the $\text{CD}_2(p, n)$ spectrum	27
2-14 LAS	28
2-15 Definition of the coordinate frames	30
2-16 Focal plane counter	31
2-17 Event selection by trigger counter	33
2-18 A cluster of one plane in the VDC	35
2-19 Method obtaining efficiency of the VDC planes	36
2-20 Efficiency of each plane	37
2-21 LAS solid angle	38
2-22 Cross section for the $^{12}\text{C}(p, p)$ elastic scattering	39
2-23 Consistency among three magnetic field sets	40
2-24 Subtraction of carbon contribution from the $\text{CD}_2(p, p')$ spectrum	41
3-1 $^2\text{H}(p, p')$ at proton energy of 400 MeV	45
3-2 $^2\text{H}(p, n)$ at proton energy of 392 MeV	45
3-3 $^6\text{Li}(p, p')$ at proton energy of 400 MeV	46
3-4 $^6\text{Li}(p, n)$ at proton energy of 392 MeV	46
3-5 $^7\text{Li}(p, p')$ at proton energy of 400 MeV	47
3-6 $^7\text{Li}(p, n)$ at proton energy of 392 MeV	47
3-7 $^9\text{Be}(p, p')$ at proton energy of 400 MeV	48
3-8 $^9\text{Be}(p, n)$ at proton energy of 392 MeV	48
3-9 $^{12}\text{C}(p, p')$ at proton energy of 400 MeV	49
3-10 $^{12}\text{C}(p, n)$ at proton energy of 392 MeV	49
3-11 $^{13}\text{C}(p, p')$ at proton energy of 400 MeV	50
3-12 $^{13}\text{C}(p, n)$ at proton energy of 392 MeV	50
3-13 $^{\text{nat}}\text{Ca}(p, p')$ at proton energy of 400 MeV	51

3-14 $^{nat}\text{Ca}(p, n)$ at proton energy of 392 MeV	51
3-15 $^{181}\text{Ta}(p, p')$ at proton energy of 400 MeV	52
3-16 $^{181}\text{Ta}(p, n)$ at proton energy of 392 MeV	52
3-17 $^{208}\text{Pb}(p, p')$ at proton energy of 400 MeV	53
3-18 $^{nat}\text{Pb}(p, n)$ at proton energy of 392 MeV	53
3-19 $^{nat}\text{Cu}(p, p)$ at proton energy of 400 MeV	54
3-20 $^2\text{H}(p, n)$ at proton energy of 295 MeV	54
3-21 $^{12}\text{C}(p, n)$ at proton energy of 295 MeV	55
3-22 $^{nat}\text{Ca}(p, n)$ at proton energy of 295 MeV	55
3-23 Peak position for the $^{12}\text{C}(p, n)$ spectrum at 20°	59
3-24 Peak position for the $^{12}\text{C}(p, p')$ spectrum at 28°	59
3-25 Momentum transfer dependence of peak positions and analyzing powers for ^{12}C	60
3-26 Momentum transfer dependence of peak positions and analyzing powers for ^{nat}Ca	61
3-27 Momentum transfer dependence of peak positions and analyzing powers for Pb	61
3-28 Momentum transfer dependence of peak positions and analyzing powers for ^2H	62
3-29 Mass number dependence of the peak positions at 20°	62
3-30 Mass number dependence of the analyzing powers at 20° and 28°	63
4-1 Schematic diagram of the impulse approximation for the quasi elastic scattering	65
4-2 Schematic picture for describing the Glauber model	67
4-3 The response function of Fermi gas model	69
4-4 The deviation of the peak position	71
4-5 Result of $\Delta\omega$ of the FGM	72
4-6 N_{eff}	75
4-7 A_{eff}	75
4-8 Schematic diagram of kinematics	77
4-9 Quasi-elastic scattering kinematics	79
4-10 NN cross section at 400 MeV	80
4-11 Energy dependence of the NN cross section around 400 MeV	81
4-12 Kinematic effects at 400 MeV	82
4-13 Peak position by the PWIA calculation	84
4-14 RPWIA calculation($m^*/m=0.7$)	91
4-15 NN amplitude for the (p, n) and (p, p') reaction	91
A-1 The response function with non-relativistic kinematics	101
B-1 NN cross section around 200 MeV	106
B-2 Kinematic effects at 200 MeV	106
B-3 NN cross section around 800 MeV	107
B-4 Kinematic effects at 800 MeV	107
E-1 Comparison between ^{13}C and ^{12}C	113

List of Tables

1-1 The QES measurements	6
2-1 Summary of experimental conditions	11
2-2 Beam energy for the (p, n) experiment derived from the time difference between the γ flush and the $^7\text{Li}(p, n)^7\text{Be(g.s.}+0.43\text{ MeV)}$ reaction.	12
2-3 Analyzing powers of the $\text{H}(p, p)$ reaction for the beam line polarimeter	15
2-4 The dynamic range of neutron energy	17
2-5 Target thickness and energy loss for the (p, n) experiment	21
2-6 Specifications of LAS and VDC counters	29
2-7 Target thickness for the (p, p') reaction measurement and calculated energy loss of the 400 MeV protons in the target.	32
2-8 Magnetic field set	40
3-1 Figure list for the reaction	44
4-1 The k_F , A_{eff} (N_{eff}), and $\Delta\omega$ results from the Fermi gas model.	73
4-2 Average masses and Fermi momenta	88
C-1 Parameters in matrix elements	108

1 Introduction

1.1 What is quasi elastic scattering

At intermediate energies where the bombarding energy E_N is greater than 100 MeV, the quasi free scattering (QFS) process becomes the dominant nucleon-nucleus scattering process. It is considered to be a one-step process where a projectile nucleon makes a single collision with a nucleon inside the nucleus. Because the wave length of the projectile at these energies is of the same order as the nucleon size (~ 1.2 fm), the projectile interacts directly with a nucleon inside the target nucleus.

The reaction process looks almost like a free nucleon-nucleon (NN) scattering process. In the QFS process, a process which does not excite nucleon degrees of freedom is called a quasi elastic scattering (QES) process. Besides the QES process, for example, a Δ excitation becomes possible at sufficiently high bombarding energies. This is called a quasi free Δ production (QF Δ) process.

Suppose the nucleus is excited with momentum transfer q and energy transfer ω , then the QES process is expected to be observed as a bump in the cross section spectrum as a function of ω . As shown in Fig. 1-1, the bump is expected to be located around the position predicted by the kinematics for free NN scattering. The position of the free NN scattering is denoted by

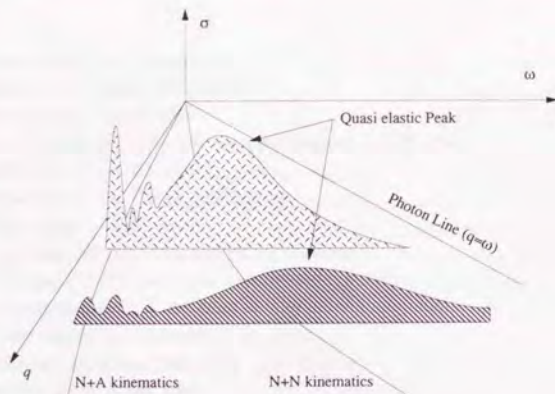


Fig. 1-1: Expected response of quasi elastic scattering in the (q, ω) plane. The vertical axis corresponds to the cross section. Experimentally, from the measurement at one reaction angle θ_{lab} the spectrum is obtained as a slice with respect to q approximately. In the slice, a bump is expected to be observed at positions accompanied by the kinematics for free NN scattering.

$\omega_f(q)$ throughout this thesis.

In the framework of the simple Fermi gas model (FGM), the centroid energy of the bump ω_{QE} coincides with the energy transfer ω_f predicted by the kinematics for free NN scattering. The energy transfer ω_f is given by

$$\omega_f = \sqrt{m^2 + q^2} - m = \frac{q^2}{m(1 + \sqrt{1 + (q/m)^2})} \approx \frac{q^2}{2m}. \quad (1-1)$$

The approximation in the last expression is provided by the non-relativistic limit as $q/m \rightarrow 0$. Here m is the nucleon mass in the nucleus. The width of the bump is given by qk_F/m where k_F is the Fermi momentum of the nucleon in the nucleus.

One of the direct ways to probe the interior of the nucleus is to measure the QES process, since QES corresponds to NN scattering in nuclear medium. The difference between QES and free NN scattering originates from existence of the nuclear medium. Consequently, the difference is expected to contain information on the nuclear medium. Such a difference may appear in several observables, not only the cross section but also the spin observables.

1.2 Response functions of the nucleus

In the beginnings of 1980's, Alberico and her collaborators[1] investigated the isovector spin longitudinal response $\sigma \cdot q$ and the isovector spin transverse response $\sigma \times q$ within the Fermi gas model with a random phase approximation(RPA) by using a $\pi + \rho + g'$ effective interaction. Here the g' term is the Landau-Migdal parameter which represents a short range interaction. Their study shows that the isovector spin-longitudinal response function R_L is enhanced and softened due to the attractive π correlations while the isovector spin-transverse response function R_T is quenched and hardened due to the repulsive ρ correlations at the momentum transfer $q = 1.0 - 2.5 \text{ fm}^{-1}$.

Figure 1-2 shows such modifications of the two response functions at momentum transfer $q = 1.3 \text{ fm}^{-1}$. Both the spin longitudinal and transverse response functions are strongly modified around the quasi elastic peak positions. As a result of the modification the peak position of the spin longitudinal (transverse) response shifts towards lower (higher) ω relative to the peak position of the free response. They predicted, therefore, that mesonic correlations in the nuclear medium might be obtained by measuring R_L and R_T .

1.3 How to probe the modification of the response function experimentally

The most direct way to investigate the response functions is to isolate each response function[2]. Experimentally, measurement of a complete set of the polarization transfer coefficients(D_{ij}) enables us to separate each response function, R_L and R_T . The polarization transfer coefficient D_{ij} relates the polarization of the incident particle with respect to the i -axis to that of the

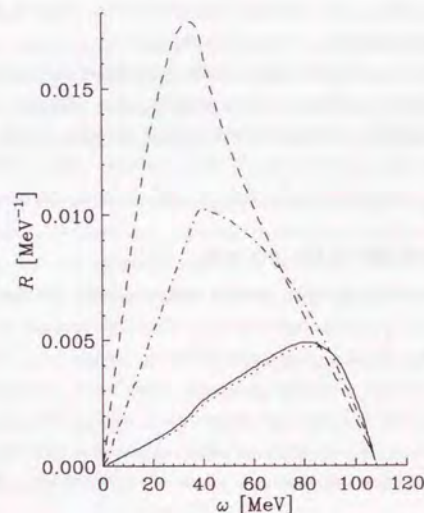


Fig. 1-2: Results of calculations with the RPA correlation at $q=1.3 \text{ fm}^{-1}$. The horizontal axis indicates the energy transfer ω . In the region around the bump, the spin longitudinal response (dashed line) is enhanced and softened relative to the free Fermi response while the spin transverse response (solid line) is reduced and hardened. The free Fermi gas response is indicated by a dot-dashed line. This figure was taken from reference [1].

scattered particle with respect to the j -axis. Such a complete set of D_{ij} provides us with information on the transferred spin direction relative to the \vec{q} direction.

Although polarization transfer coefficients have been measured for the (p, p') and (p, n) reactions, such measurements are too time consuming. Therefore it is difficult to do systematic surveys. An alternate way to study the response functions is to measure the cross section since it is easy to do systematic studies. The cross section is given by a linear combination of the response functions, R_L , R_T , and R_0 , where R_0 is the response function of the spin independent part. Therefore the cross section is also expected to be sensitive to the modification of the response functions.

The analyzing power A_y is another candidate for the systematic surveys because it is relatively easy to be measured. The experimental difficulty might depend on what kind of experimental equipment is needed. The cross sections and the analyzing powers can be measured when a polarized beam is available, while both a polarized beam and a polarimeter are required to measure the polarization transfer coefficients D_{ij} .

1.4 Historical review

1.4.1 cross section and analyzing power

In the beginning of 1980's, at the same time as the prediction by Alberico, the measurement of the cross section for proton induced quasi elastic scattering was already underway.

Chrien and his collaborators measured cross sections of the (p, p') reaction for several targets from ^6Li through Pb at a proton bombarding energy of 800 MeV[3]. They identified not only the QES peaks but also the $\text{QF}\Delta$ peaks. They investigated the peak position and mass number dependence of the cross section at the peak. It was found that the shift of the QES peak positions from ω_f predicted by the kinematics of the NN scattering is less than 2 MeV and that the integrated cross section at the peak has a mass dependence of $A^{0.4}$.

Carey and his collaborators measured analyzing powers for the (p, p') QES for the Pb and Ca targets[4]. They found that the analyzing powers at the quasi elastic peak are reduced to 60% of the free NN value both for the Pb and Ca targets.

The predicted values of the analyzing powers based on the non-relativistic model are essentially the same as those of the NN scattering[8]. Therefore the reduction of the analyzing powers for the (p, p') QES is not explained by the non-relativistic models. In the relativistic model[9, 10], on the contrary, the NN amplitudes are modified in the nuclear medium, and as a result, the analyzing powers are reduced from those for free NN scattering. This reduction of the analyzing powers for the (p, p') QES has been considered to be one of the clearest signals of relativistic effects.

The measurement of the QES process by the isovector probe, such as the (p, n) reaction, has been performed since the end of 1980's. The isovector probe excites purely the isovector

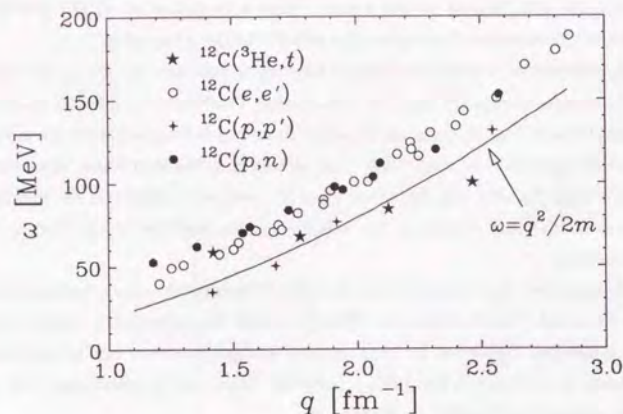


Fig. 1-3: The peak positions by the (e, e') (open circle), (p, p') (cross), $(^3\text{He}, t)$ (star), and (p, n) (solid circle) reactions. The solid line indicates the position predicted by the kinematics of the NN scattering. This figure was taken from reference [2].

responses while the (p, p') reaction excites both the isoscalar and isovector responses. For the (p, n) measurements [11, 12], the peak position is located at 20 MeV above ω_T . Such a shift of the peak position seems to indicate the strong repulsive correlation of the effective interaction.

The behavior of the peak shift is further complicated in the case of other probes such as the $(^3\text{He}, t)$ [19] or $(d, ^2\text{He})$ reactions [20, 21, 23]. The peak positions are shifted to higher ω in the regions of $q < 2.0 \text{ fm}^{-1}$ while they are shifted to lower ω in the region of $q > 2.0 \text{ fm}^{-1}$ as shown in Fig. 1-3. A similar behavior is observed in pion single charge-exchange reactions [22].

1.4.2 polarization transfer coefficients

A complete set of polarization transfer coefficients for the (p, p') reaction was measured at 500 MeV by Carey and his collaborators [4, 5]. They derived the response functions R_L and R_T separately. The ratio R_L/R_T is consistent with unity. The expected enhancement of the spin-longitudinal response is not observed from the results of the (\vec{p}, \vec{p}') measurements. The same conclusion has been derived from the results of (\vec{p}, \vec{n}) measurements. The ratio R_L/R_T is again close to unity [12, 17]. This result seems to indicate the significant modifications of either π or ρ correlation in nuclei.

E_p [MeV]	Facility	observables	Target	q [fm^{-1}]	Ref.
(p, p') QES					
290	TRIUMF	σ, A_y	^{208}Pb	0.8 — 2.5	[8]
400	RCNP	σ, A_y	$^2\text{H} - ^{208}\text{Pb}$	1.0 — 2.4	present data
420	TRIUMF	σ, A_y	^{208}Pb	0.8 — 2.5	[8]
500	LAMPF	$\sigma, A_y, P_y', D_{ij}$	$^2\text{H}, ^{12}\text{C}, ^{40}\text{Ca}, ^{208}\text{Pb}$	1.8	[4, 5]
800	LAMPF	σ	$^2\text{H} - ^{208}\text{Pb}$	0.8 — 3.0	[3]
(p, n) QES					
186, 200	IUCF	σ, A_y	$^2\text{H} - ^{13}\text{C}$	1.0 — 2.4	[15]
290	TRIUMF	σ, A_y	$^{12}\text{C}, ^{54}\text{Fe}$	1.4	[16]
295	RCNP	σ, A_y	$^2\text{H}, ^{12}\text{C}, ^{40}\text{Ca}$	1.0 — 2.5	present data
346	RCNP	$\sigma, A_y, P_y', D_{ij}$	$^2\text{H}, ^6\text{Li}, ^{12}\text{C}, ^{40}\text{Ca}, ^{208}\text{Pb}$	1.7	[17]
392	RCNP	σ, A_y	$^2\text{H} - ^{208}\text{Pb}$	1.0 — 2.4	present data
420	TRIUMF	σ, A_y	^{12}C	2.1	[16]
495	LAMPF	σ, A_y	$^2\text{H}, ^{12}\text{C}, ^{208}\text{Pb}$	1.0 — 2.1	[11]
		$\sigma, A_y, P_y', D_{ij}$	$^2\text{H}, ^{12}\text{C}, ^{40}\text{Ca}$	1.75	[12]
795	LAMPF	σ, A_y	$^2\text{H}, ^{12}\text{C}, ^{208}\text{Pb}$	1.0 — 3.5	[11]
other isovector probes					
170 (n, p)	LAMPF	σ	^{12}C	1.5	[24]
1600 (d, ^2He)	LNS	σ, A_y, A_{ij}	^{12}C	2.1	[23]
2000 ($^3\text{He}, t$)	LNS	σ	^{12}C	1.4 — 2.5	[19]

Table 1-1: Summary of the QES measurements

1.4.3 summary of the historical review

The measurements of the QES process which have been reported up to now are listed in table 1-1. Until now, questions related to proton induced QES may be categorized into three issues.

- For the (p, n) QES, why are the peak positions located at higher energy transfer relative to the position predicted by the kinematics for free NN scattering?
- For the (p, p') QES, why is the reduction of the analyzing powers reduced relative to that for free NN scattering.
- Why is the R_L/R_T ratio consistent with unity, which contradicts with the RPA prediction.

1.5 Thesis objectives

In this thesis, we focus on a study of the QES process for both the (p, n) and (p, p') reactions. The main aim is to answer the issues A and B by systematic measurements of the cross sections

and analyzing powers. We have measured the cross sections and the analyzing powers of the QES region for the (p, p') reaction at 400 MeV and the (p, n) reaction at 295 and 392 MeV. The advantage of these incident energies is that the total cross sections of the NN scattering have their minimum values. Using the protons of such an initial energy, the one-step process becomes dominant because the mean free path gets longer depending on the decrease of the total cross sections. Fig. 1-4 shows the energy dependence of the total cross sections of the $p + p$ and $n + p$ scatterings. It clearly shows the minimum around 200-400 MeV.

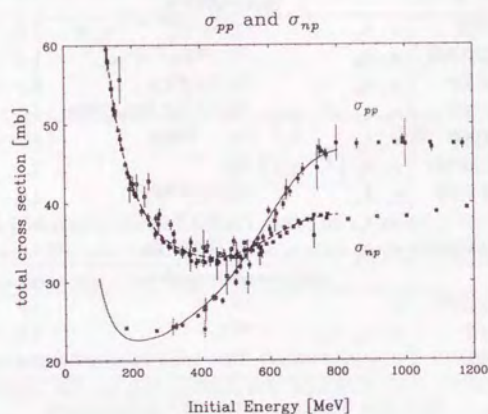


Fig. 1-4: As a function of the initial laboratory energy of protons, the total cross section σ_{pp} (σ_{np}) of the $p + p$ ($n + p$) reaction is indicated by solid (dashed) line. The total cross sections have minimum values around 200 - 400 MeV.

Using the results of the cross sections and analyzing powers of the (p, n) and (p, p') QES, we investigate the q and A dependence of the peak positions and the analyzing powers at the peak positions. We discuss how simple models are able to explain simultaneously the characteristic features extracted from this investigation.

1.6 Thesis outline

We describe the experimental procedures and data analyses in section 2.

In section 3, all spectra taken in the measurements are shown. From the spectra we derive peak positions and analyzing powers at the peak positions.

In section 4, three models in which the target nucleus is regarded as the Fermi gas are discussed. The results of the calculations of the models are compared with the experimental data. We search for a model which describes the cross sections and analyzing powers for both

(p, n) and (p, p') reactions simultaneously. We summarize this work in section 5. Finally the conclusions are given in section 6.

2 Experiment and Data analysis

In this section experimental methods for both the (p, n) and (p, p') measurements are described. Firstly, an overview of the experiments is given. Then instruments for measuring the (p, n) reaction and methods of data analyses are described. Lastly, instruments for measuring the (p, p') reaction and methods of data analyses are described.

2.1 Overview

All experiments were carried out at the ring cyclotron facility at Research Center for Nuclear Physics (RCNP). A schematic representation of cyclotrons, beam lines, and experimental halls is shown in Fig. 2-1.

The experiments measuring the (p, n) reaction were carried out at the N0 beam line. The N0 beam line consists of a target system in a swinger magnet, Neutron Time-Of-Flight (NTOF) tunnel, and a neutron detector complex in the tunnel. The neutron detector complex was developed as a Neutron POLarimeter (NPOL) for measurements of polarization transfer coefficients. In the measurement described in this thesis, the NPOL was operated just as an efficient neutron detector.

Polarized protons are transported from an ion source to a beam dump as follows. The protons (\vec{p}) are produced by the polarized ion source, then are accelerated by the AVF cyclotron and then by the ring cyclotron up to energies of 295 or 392 MeV. In an injection line to the ring cyclotron a low energy beam-line polarimeter is located. This low energy polarimeter was used for calibrating beam line polarimeters for high energy protons which are located at beam lines downstream from the ring cyclotron. The protons are transported to the N0 experimental hall along the N0 beam line. The polarization of the proton beam is monitored by the beam line polarimeter located upstream from the target chamber in the N0 experimental hall. Details of the N0 experimental hall, NTOF, and NPOL are described in subsection 2.3.5.

The experiment measuring the (p, p') reaction was carried out at the WN beam line using a Large Acceptance Spectrograph (LAS). The beam protons are produced in a similar manner as the (p, n) measurements. Polarized protons were accelerated in the two cyclotrons up to energy of 400 MeV. The polarization of the protons is monitored in a beam line polarimeter at the entrance of the WN experimental hall. The protons are transported to a target chamber and collected by a beam stopper in the target chamber. Scattered protons from the target are momentum-analyzed by the spectrograph LAS and detected by the focal plane counters.

Each of the major instruments of the N0 and WN beam lines will be briefly discussed. More detailed information can be found in references [30, 32, 33].

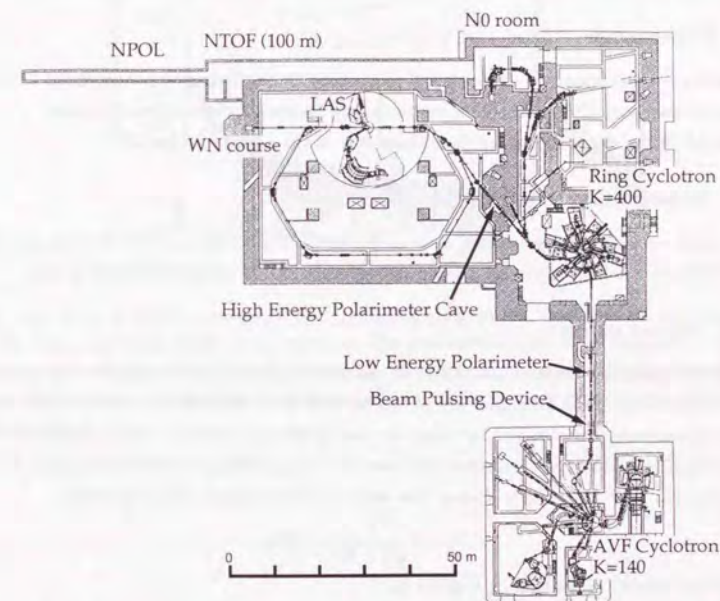


Fig. 2-1: The ring cyclotron facility at RCNP is shown. The (p, n) experiments were performed at the N0 beam line and the (p, p') experiment was performed at the WN beam line.

Table 2-1: Summary of experimental parameters. Beam bunch intervals ΔT are inverted numbers of radio frequencies of the AVF cyclotron.

Dates	Program number	Reaction	Energy [MeV]	Radio frequency [MHz]	ΔT [ns]
1992 5/2 - 5/4	A108	(<i>p</i> , <i>n</i>)	295	15.41677	64.864
1992 12/10 - 12/13	E17	(<i>p</i> , <i>n</i>)	392	16.84535	59.364
1994 2/24 - 2/26	E17	(<i>p</i> , <i>n</i>)	392	16.84535	59.364
1994 6/1 - 6/6	E58	(<i>p</i> , <i>p'</i>)	400	16.98420	58.878

2.2 Experiment

In table 2-1 a summary of experimental parameters for each measurement is listed including the radio frequency (RF) of the AVF cyclotron and intervals between beam bunches.

The RF of the ring cyclotron is three times that of the AVF cyclotron[25].

2.3 Experimental setup for (*p*, *n*) measurement

We have constructed the neutron time-of-flight (NTOF) facility and the neutron polarimeter (NPOL) system[30]. All (*p*, *n*) experiments were performed using the NTOF facility.

2.3.1 Proton energy

Polarized protons were accelerated first by the AVF cyclotron and then by the ring cyclotron. Radio frequencies for acceleration are shown in table 2-1. An accurate beam energy in the (*p*, *n*) experiments was obtained by using the time difference between γ flush originating from π^0 production in the target and neutrons from the ${}^7\text{Li}(p, n){}^7\text{Be}(\text{g.s.}+0.43 \text{ MeV})$ peak. In Fig. 2-2 a typical TOF spectrum is shown. The neutron kinetic energy (T_n) is given by

$$T_n = \left(\frac{1}{\sqrt{1 - \beta_n^2}} - 1 \right) m_n, \quad (2-1)$$

where the velocity of neutron β_n is given by

$$\frac{L_{\text{path}}}{c} \left(\frac{1}{\beta_n} - 1 \right) = \Delta t. \quad (2-2)$$

This calibration was performed with the flight path $L_{\text{path}} = 78.2 \text{ m}$, which gave Δt as 107.92 ns. The neutron energy of the ${}^7\text{Li}(p, n){}^7\text{Be}(\text{g.s.}+0.43 \text{ MeV})$ was derived to be 389.64 MeV. The Q -values of the reactions are -2.07 MeV and -1.65 MeV for the ground and $E_x=0.43 \text{ MeV}$ states, respectively. We estimated the average Q -value to be -1.86 MeV . The average energy loss in the target was calculated to be 0.65 MeV . Consequently, the incident proton energy was found to be 392.2 MeV . The uncertainty of the proton energy was mainly determined by the time resolutions of the γ peak and the neutron peak. The time walk was constant within 50 ps during the (*p*, *n*) measurement. Thus, the beam energy spread was less than 0.9 MeV shown in the table 2-2.

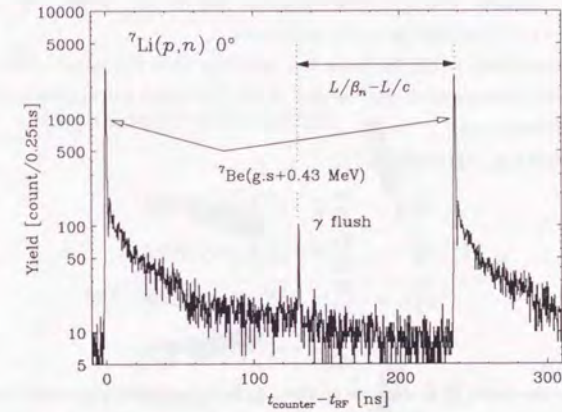


Fig. 2-2: Time of flight spectrum of the ${}^7\text{Li}(p, n)$ reaction at 0° . Two large peaks correspond to the ${}^7\text{Li}(p, n){}^7\text{Be}(\text{g.s.}+0.43 \text{ MeV})$ reaction. The peak around 130 ns corresponds to γ rays. These γ rays originate from the π^0 produced in the target. The time difference between the peak of the γ rays and the neutron peak of the ${}^7\text{Li}(p, n){}^7\text{Be}$ reaction was used to calibrate the neutron energy.

Table 2-2: Beam energy for the (*p*, *n*) experiment derived from the time difference between the γ flush and the ${}^7\text{Li}(p, n){}^7\text{Be}(\text{g.s.}+0.43 \text{ MeV})$ reaction.

	Δt [ns]	E_n [MeV]	$-Q$ [MeV]	Target [MeV]	Beam energy [MeV]
value	107.92	389.64	1.86	0.65	392.15
spread	0.05	0.85	0.22	0.1	0.88

2.3.2 Beam polarization

The polarization of the proton beam was monitored by the beam line polarimeters (BLP)[26]. A polarization axis was parallel to the magnetic field direction of the cyclotrons and of the beam transport dipole magnets. The polarization direction was reversed between up and down with an interval of 2 s or 10 s depending on the experiments.

One BLP was installed at the N0 beam line upstream from the target. Note that another BLP with the same configuration was installed at the WN beam line upstream from the target for the (p, p') measurement.

Beam polarization p_y is given by

$$Y_L^U = \frac{d\sigma}{d\Omega}(1 + p_y^U A_y) N Q^U \Delta\Omega_L, \quad (2-3)$$

$$Y_R^U = \frac{d\sigma}{d\Omega}(1 - p_y^U A_y) N Q^U \Delta\Omega_R, \quad (2-4)$$

$$Y_L^D = \frac{d\sigma}{d\Omega}(1 - p_y^D A_y) N Q^D \Delta\Omega_L, \quad (2-5)$$

$$Y_R^D = \frac{d\sigma}{d\Omega}(1 + p_y^D A_y) N Q^D \Delta\Omega_R, \quad (2-6)$$

where $Y_{L(R)}^\alpha$ are the yields, $\frac{d\sigma}{d\Omega}$ is the cross section, A_y is the analyzing power, Q^α is the integrated charge for polarization direction α , N is the target thickness, and $\Omega_{L(R)}$ are the solid angles of the left (right) counter. When p_y^U equals to p_y^D , p_y is derived by

$$p_y = \frac{1}{A_y} \frac{\sqrt{y} - 1}{\sqrt{y} + 1} \quad \text{when} \quad y = \frac{Y_L^U Y_R^D}{Y_R^U Y_L^D}. \quad (2-7)$$

In order to determine p_y from the measurement, it is necessary to know the A_y value of the reaction beforehand. We employed a $H(\vec{p}, p)$ reaction at 17° for polarimetry. At 400 MeV the analyzing power for the $H(\vec{p}, p)$ scattering is maximum around the laboratory angle of 17° . A forward scattered proton and a backward recoil proton were detected in coincidence by two plastic scintillators. As depicted in Fig. 2-3, two pairs of plastic scintillators were placed at left and right sides of the beam line. In order to determine the reaction angle for the $H(\vec{p}, p)$ reaction, the backward protons were collimated with slits which had a window of $5 \text{ mm} \times 20 \text{ mm}$. The length between the target and the collimator was 250 mm. The opening angle of the backward detector was therefore 1.14° which corresponds to the opening angle of the forward detector of 0.98° . When the forward scattered proton is detected at 17° , the angle of the backward scattered proton is determined by the projectile energy. The angles and the analyzing powers used in the measurements are listed in table 2-3.

We used a polyethylene(CH_2) sheet as the polarimeter target. Therefore the carbon contribution to the analyzing power should be taken into account. The analyzing power of the $\text{CH}_2(p, p')$ reaction was calibrated with the low energy polarimeter. For the low energy polarimeter, the $^{12}\text{C}(\vec{p}, p)^{12}\text{C}(\text{g.s.})$ reaction [27] which had been well calibrated was used.

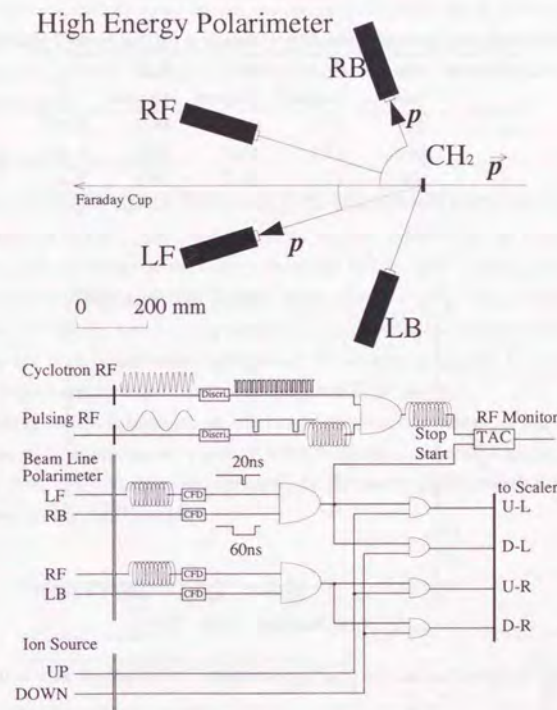


Fig. 2-3: Beam line polarimeter and associated circuits

The calibrated analyzing power was consistent with those for the $H(p, p')$ reaction. The target polyethylene(CH_2) was inserted continuously in the BLP during experiments. The events of the $p + p$ reaction in the polarimeter were counted simultaneously during the (p, n) measurement. For the (p, p') measurement the beam polarization was monitored in the same manner.

The beam polarization was stable within $0.7 \sim 0.8$ for all experiments. The time dependence of the beam polarization during the (p, p') measurement is shown as an example in Fig. 2-4.

Table 2-3: Analyzing powers of the $H(p, p)$ reaction for the beam line polarimeter

Particle	Energy [MeV]	θ_f [degree]	θ_b [degree]	$\theta_{c.m.}$ [degree]	A_y
p	295	17.0	70.5	36.4	0.402
	392	17.0	69.7	37.2	0.461
	400	17.0	69.7	37.2	0.465

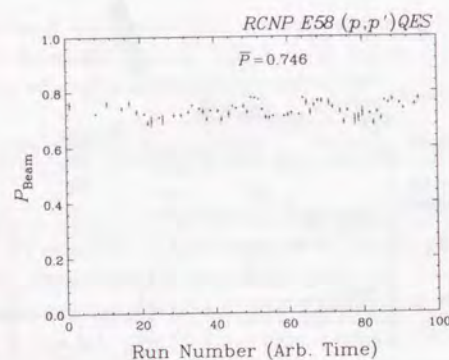


Fig. 2-4: Beam polarization in the (p, p') experiment. A horizontal axis indicates arbitrary time.

2.3.3 Beam current

Protons were transported to a Faraday-Cup after bombarding the target. The total charge of protons was summed up by a current integrator which was connected to the Faraday-Cup. At the same time the beam line polarimeter also counted the number of scattered protons from the $CH_2(p, p')$ reaction at 17° . Using the counts of the beam line polarimeter the total charge

Q is derived by

$$Q_\alpha = Q_{0\alpha} \sqrt{Y_L^\alpha \times Y_R^\alpha}, \quad (2-8)$$

where a suffix α corresponds to the beam spin mode U or D .

Because of multiple scattering of beam protons in the target, especially in the target with large mass number, beam protons partly hit the pole of the swinger magnet or other equipment. As a result, total charge was not always collected by the Faraday-cup at the beam dump. As an alternate way to obtain the total charge, we used the counts by the BLP which was free from such an ambiguity. The ratio $Q_{0\alpha}$ is needed to derive the absolute value of the total charge from the counts of the BLP. We calibrated the ratio before the measurements without targets in the swinger magnet.

2.3.4 Beam timing structure

For the TOF technique, the time structure of the proton beam is of great importance. The accelerators provide beam bunches with a pulse interval determined by the cyclotron radio frequency. In order to detect lower energy neutrons by the TOF method, intervals of beam bunches are required to be longer than those determined by the cyclotron acceleration frequency. In other words, low energy neutrons are required to reach a neutron counter before high energy neutrons from the next bunch reach the counter. Thus, a longer bunch interval enables us to measure the larger energy range of neutrons using the TOF method.

A beam pulsing device is installed at the beam injection line shown in Fig. 2-1 to enlarge the bunch interval by sweeping out a part of beam bunches. A schematic picture of sweeping is shown in Fig. 2-5. Only bunches not deflected by the device pass through a slit downstream and are injected to the ring cyclotron.

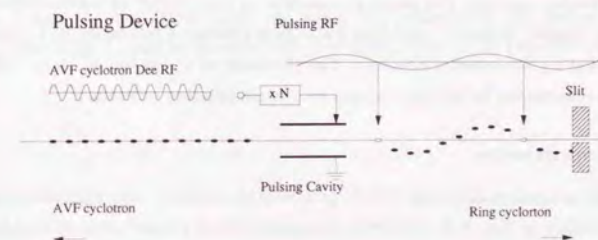


Fig. 2-5: Schematic view of a pulsing device installed at an injection beam line to the ring cyclotron. The situation for a pulsing number N equal to 9 is shown.

The frequency of this device is set to $1/N$ of the acceleration frequency of the AVF cyclotron,

Table 2-4: The large dynamic range for neutron energy was provided by partly sweeping the beam bunches by the pulsing device. Pulsing ratio 4 was used for the (p, n) measurements.

proton energy [MeV]	pulsing [ns]	interval [ns]	flight length [m]	neutron energy lower limit [MeV]
392	4	238.456	78.2	145
295	4	259.456	58.5	63

where N is an integer number. In case of even number N , two bunches on 0 and π of phase out of N bunches are not deflected. In case of odd number N , only one bunch on 0 of phase out of N bunches is not deflected.

Consequently, the bunch interval is enlarged to $N/2$ (N) times of the AVF frequency. For the (p, n) measurement the ratio N was set to 8. The interval of the beam bunches was 4 times longer than the interval determined by the AVF cyclotron and 259.456 ns for 295 MeV and 237.456 ns for 392 MeV, respectively. The experimental conditions specific to the beam bunches are summarized in table 2-4.

In order to keep the interval obtained by the beam pulsing device, a single turn extraction from the ring cyclotron is also required. The single turn extraction was steadily maintained during the experiments.

2.3.5 N0 room

Figure 2-6 shows the beam line in the N0 room. The main feature of this room is a target system (C in Fig. 2-6) in a swinger magnet (B). The swinger magnet consists of two dipole magnets each having a bending angle of 45° . The beam is transported through the swinger magnet to a Faraday-cup (E). The target is controlled to move along the central beam trajectory in the swinger magnet. Scattered neutrons which pass through a collimator in a concrete shield (D) are detected by the neutron detector. The thickness of the shield is 1.5 m. The reaction angle (θ_{lab}) is determined by setting a target at a corresponding position.

2.3.6 Neutron detector

We used the neutron polarimeter NPOL as a neutron counter with high neutron detection efficiency. As shown in Fig. 2-7, the NPOL consisted of four planes¹ of neutron detectors each with a volume of $100 \times 100 \times 10 \text{ cm}^3$.

Two of them are made of liquid scintillators (Bicron BC-519) and the rest of two are made of plastic scintillators (Bicron BC-408). Photo multiplier tubes with a diameter of 12.5 cm

¹The NPOL is now upgraded to six planes of the neutron counters. Extra two planes of liquid scintillators have been added to increase the double scattering efficiency of the neutrons.

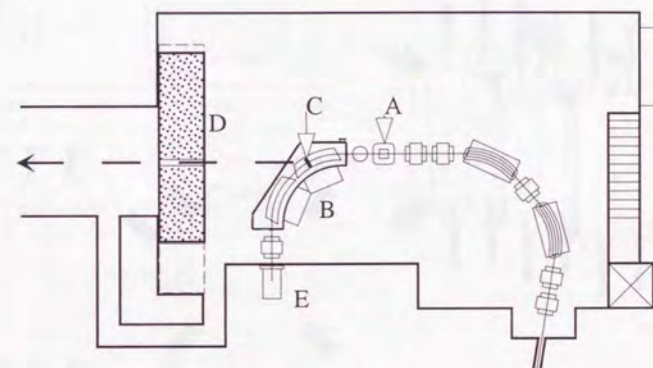


Fig. 2-6: Schematic view of N0 room. A: Beam line polarimeter. B: Swinger magnet. C: Target. D: Shield door made of concrete and neutron collimator. E: Faraday-cup.

are mounted at four corners of each neutron detector. Time signals from the photo multiplier tubes are used to determine the time of arrival as well as the two-dimensional position at which a neutron interacts with scintillator material in the neutron detector. In front of the neutron detector, detectors for particle identification are located. The detector consists of three $35 \times 110 \times 0.5 \text{ cm}^3$ plastic scintillators. The block diagram of the electronics is shown in Fig. 2.3.6.

For the 392 MeV (295 MeV) experiment, the neutron counter was positioned at 78.2 m (58.5 m) from the 0° target position.

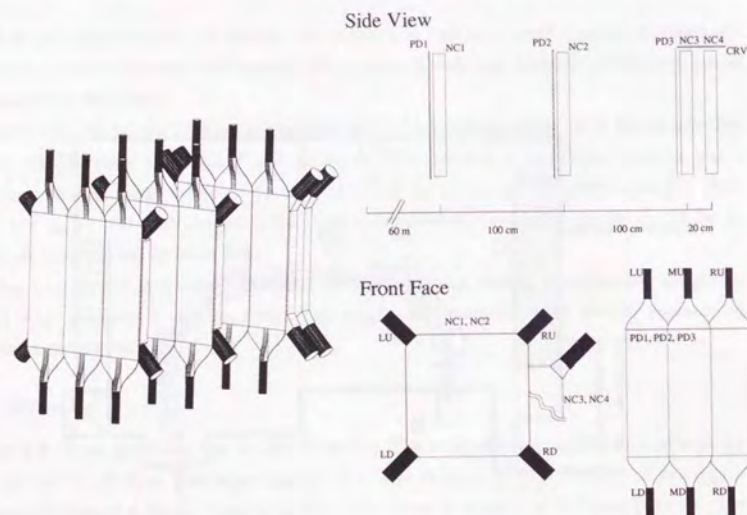


Fig. 2-7: Neutron polarimeter system

2.3.7 Targets

For the (p, n) measurement, we used targets listed in table 2-5 ranging from ^2H to $^{\text{nat}}\text{Pb}$ in order to investigate the mass number A -dependence of the QES response. The thickness was determined from the requirement that the energy loss of the beam proton was about 1 MeV. The total energy resolution was determined mainly by the time resolution of the TOF methods, typically 4 MeV for 400 MeV neutrons.

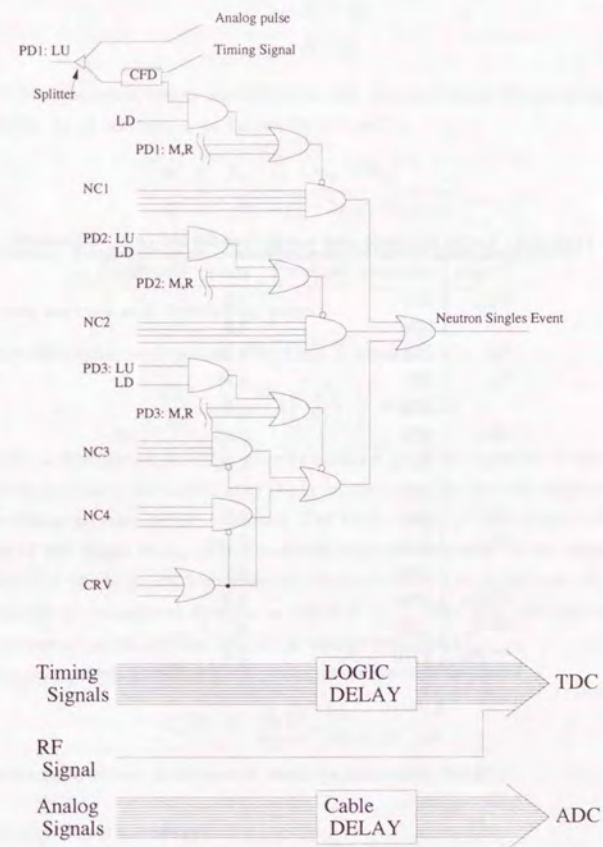


Fig. 2-8: Circuit for neutron singles event

Table 2-5: Target thickness and energy loss for the (p, n) experiment

Target	thickness [mg/cm ²]	energy loss [MeV]
CD ₂	380	1.3
	924	3.0
⁶ Li	123.6	0.30
⁷ Li	379	0.91
	534	1.3
⁹ Be	278	0.67
¹² C	342.5	0.93
	685	1.9
¹³ C	450	1.2
	1108	2.7
^{nat} Ca	396	0.95
	1108	2.7
^{nat} Cu	1787	3.8
¹⁸¹ Ta	1331	2.2
^{nat} Pb	2270	3.4

2.4 Data analysis for (p, n) measurement

2.4.1 Energy transfer and momentum transfer

The energy transfer ω and the momentum transfer q are defined by

$$\omega = E_i - E_f, \quad (2-9)$$

$$\vec{q} = \vec{p}_i - \vec{p}_f, \quad (2-10)$$

where $E_i(E_f)$ is the total energy and $\vec{p}_i(\vec{p}_f)$ is the momentum of the projectile (scattered particle). In the (p, n) reaction, ω and q can be denoted by

$$\omega = T_p - T_n + m_p - m_n, \quad (2-11)$$

$$q = \sqrt{p_p^2 + p_n^2 - 2p_p p_n \cos \theta_{\text{LAB}}}, \quad (2-12)$$

where T is kinetic energy and θ_{LAB} is scattering angle in the laboratory frame.

2.4.2 Cross section and Analyzing power

The double differential cross section $d^2\sigma/d\Omega d\omega$ is given as

$$\frac{dY^\alpha}{d\omega}(\omega) = \epsilon \left(\frac{d^2\sigma}{d\Omega d\omega} \right)^\alpha N Q^\alpha \Delta\Omega. \quad (2-13)$$

Here the suffix α denotes the direction of polarization U or D of the beam. Neutron detection efficiency ϵ was calibrated before and after the (p, n) measurement for each counter by using the reaction for which the cross section is known. The total charge Q^α was monitored by the BLP. The number of the target atoms N was obtained from the thickness of the target. The solid angle covered $\Delta\Omega$ of the neutron counter was determined by the flight path (L_{path}) and the effective area (S) of the neutron detector as $\Delta\Omega = S/L_{\text{path}}^2$. The yield $dY^\alpha/d\omega$ is the number of counts monitored by the neutron counter at energy transfer of ω .

The analyzing power is given by

$$A_y(\omega) = \frac{1}{p_y} \frac{dY^U/d\omega - dY^D/d\omega}{dY^U/d\omega + dY^D/d\omega}, \quad (2-14)$$

where p_y is the polarization of the proton beam monitored by the BLP.

2.4.3 Neutron kinetic energy

Neutron kinetic energy (T_n) is determined by the time of flight (TOF) method shown in Fig. 2-9 as

$$\beta_n = L_{\text{path}}/ct_{\text{TOF}}, \quad (2-15)$$

$$\gamma_n = \frac{1}{\sqrt{1 - \beta_n^2}}, \quad (2-16)$$

$$T_n = E_n - m_n = (\gamma_n - 1)m_n. \quad (2-17)$$

Here t_{TOF} is the flight time from the target to the counter and determined by

$$\begin{aligned} t_{\text{TOF}} &= t_{\text{counter}} - t_{\text{target}}, \\ t_{\text{target}} &= t_{\text{RF}} + t_0, \end{aligned} \quad (2-18)$$

where t_0 is the time for the beam to be transported from the AVF cyclotron to the target position, and t_{counter} is derived from four timing signals ($t_{\text{LU}}, t_{\text{LD}}, t_{\text{RU}}, t_{\text{RD}}$) from the neutron detector[30]. The time $t_0 = t_{\text{target}} - t_{\text{RF}}$ might fluctuate depending on the stability of the cyclotrons and the beam transport. The time intervals $t_{\text{BLP}} - t_{\text{RF}}$ were monitored continuously by the BLP.

The fluctuation of t_0 was therefore monitored by the BLP as shown in Fig. 2-10.

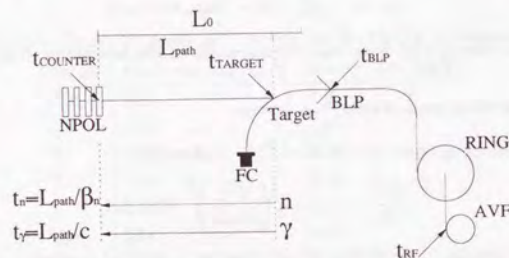


Fig. 2-9: Schematic view of timing relation. Details are described in the text.

The energy resolution is determined from the timing resolution. When the detector thickness ΔL is explicitly given, the energy resolution is

$$\frac{\Delta E_n}{E_n} = \gamma_n(\gamma_n + 1) \sqrt{\left(\frac{\Delta t}{t_{\text{TOF}}}\right)^2 + \left(\frac{\Delta L}{L_{\text{path}}}\right)^2}. \quad (2-19)$$

2.4.4 Neutron detection efficiency calibration

Neutron detection efficiency was calibrated before and after each run of measurements using the ${}^7\text{Li}(p, n){}^7\text{Be}(\text{g.s.} + 0.43 \text{ MeV})$ reaction at 0° . The cross section of this reaction is known to be almost constant at bombarding energy from 80 MeV to 800 MeV[29]. The cross section ($d\sigma/d\omega$) is reported to be $35.3 \pm 2.4 \text{ mb/sr}$ for 300 MeV and $35.8 \pm 2.4 \text{ mb/sr}$ for 400 MeV in the laboratory frame.

The neutron detection efficiency depends on the threshold E_{th} for the light output from the counter as

$$\epsilon(E_{th}) = \frac{Y(E_{th})}{\frac{d\sigma}{d\Omega} N Q \Delta \Omega}, \quad (2-20)$$

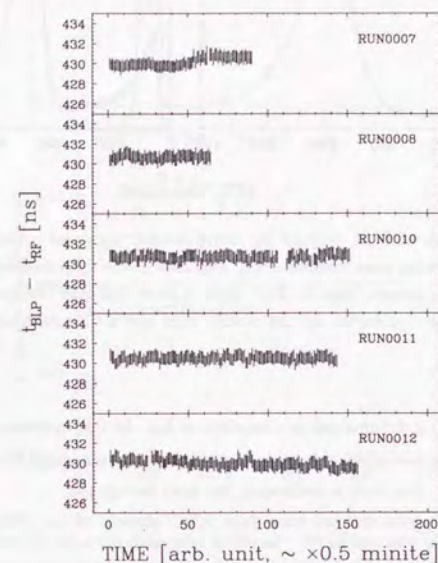


Fig. 2-10: Typical timing monitoring results. The time intervals $t_{\text{BLP}} - t_{\text{RF}}$ were monitored with the BLP counter and were recorded simultaneously. The horizontal axis indicates a block position of the magnetic tape which corresponds to the elapsed times after starting the run. One bin corresponds approximately to 0.5 minutes even though it depends on event rate. For notations, see text.

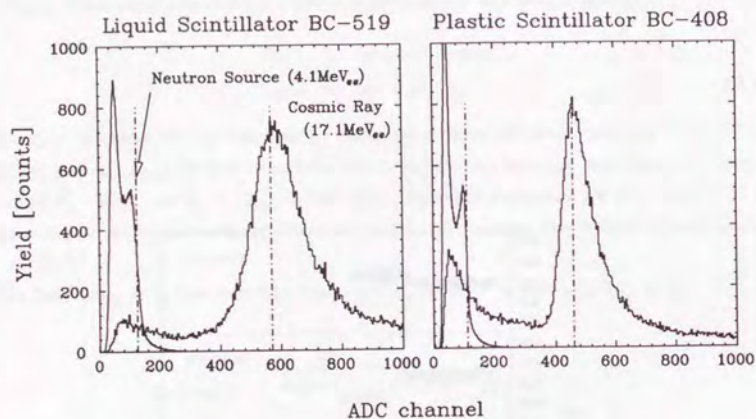


Fig. 2-11: Calibration of light outputs by using cosmic rays and γ rays from a $^{241}\text{Am}-^9\text{Be}$ neutron source. Horizontal axes indicate ADC channels of the light outputs of liquid scintillator (left) and plastic scintillators (right). Dot-dashed lines indicate the referred energies which correspond to minimum ionization by the cosmic rays and a Compton edge by the 4.4 MeV γ rays.

where the yield $Y(E_{th})$ is determined as a function of E_{th} . In this expression, we used the known value for $\frac{d\sigma}{d\Omega}$. The detection efficiency of the neutron counter was about 3% with $E_{th} = 32 \text{ MeV}_{ee}$ as shown in Fig. 2-12. The unit is defined in the next paragraph.

The light output L_{NC} is derived from four ADC signals of the PMT outputs by taking geometrical means as

$$L_{NC} = \sqrt[4]{L_{LU} \cdot L_{LD} \cdot L_{RU} \cdot L_{RD}}. \quad (2-21)$$

The geometrical means are approximately independent of 2-dimensional positions on the neutron counter where incident particles are detected. The L_{NC} is calibrated using cosmic rays and 4.4 MeV γ rays from a $^{241}\text{Am}-^9\text{Be}$ neutron source. The energy deposited by the cosmic rays is expect to be due to minimum ionization in the neutron counter. Therefore the light output by the cosmic rays corresponds to $1.7 [\text{MeV/g/cm}^2] \times 10 [\text{g/cm}^2]$ in the electron light response. This response is generally denoted by unit of MeV_{ee} . We referred to the work by Cecil and his collaborators [31] for converting the response to the proton response. Figure 2-11 shows the results of the light output calibration for the liquid (left) and plastic (right) scintillators. Both the peak of the cosmic rays and the Compton edge by the 4.4 MeV γ rays can be clearly recognized in the spectra.

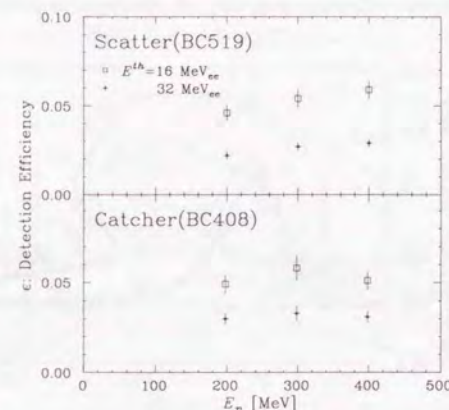


Fig. 2-12: The calibrated neutron detection efficiency of the neutron detectors. Top(bottom) frame indicates the efficiency of the liquid (plastic) scintillator. Open squares (crosses) indicate the efficiency when the threshold is set at 16(32) MeV_{ee} . We performed the calibration with 200, 295, and 392 MeV protons.

2.4.5 $^2\text{H}(p, n)$ spectrum

Cross sections and analyzing powers for the $^2\text{H}(\vec{p}, n)$ reaction were obtained by subtracting the carbon contribution from those for the $\text{CD}_2(\vec{p}, n)$ reaction as

$$\begin{aligned}\sigma_{2\text{H}} &= (\sigma_{\text{CD}_2} - \sigma_{\text{C}})/2, \\ A_y^{2\text{H}} &= (A_y^{\text{CD}_2} - f_{\text{C}} A_y^{\text{C}})/(1 - f_{\text{C}}),\end{aligned}\quad (2-22)$$

where $f_{\text{C}} = \sigma_{\text{C}}/\sigma_{\text{CD}_2}$. A representative set of cross section spectra is shown in Fig. 2-13.

A normalization factor is determined for all angles by adjusting an integrated value of a prominent 4^- state peak in ^{12}N .

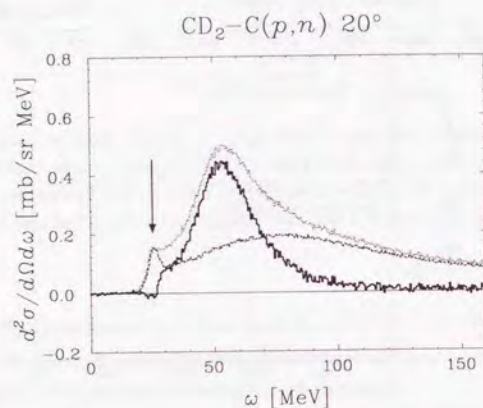


Fig. 2-13: The carbon contribution was subtracted from the $\text{CD}_2(p, n)$ spectrum. The spectra at 392 MeV and 20° are shown. The dotted curve indicates the $\text{CD}_2(p, n)$ spectrum while the dashed curve indicates the $\text{C}(p, n)$ spectrum. The $\text{D}(p, n)$ spectrum indicated by the solid line is obtained from these two spectra. An arrow at $\omega = 25$ MeV indicates a 4^- state peak in ^{12}N from which the normalization factor was determined.

2.5 Experimental setup for the (p, p') measurement

We performed the (p, p') measurement at the WN beam line using the spectrograph LAS.

2.5.1 Spectrograph LAS

The spectrograph LAS consists of a quadrupole magnet (Q) and a dipole magnet (D) as is shown in Fig. 2-14. The spectrograph LAS is designed to analyze particles momentum up to 1 GeV/c, which corresponds to a kinetic energy of a little more than 400 MeV in the case of protons. The typical feature is listed in table 2-6. The most striking property for the QES measurement is a momentum bite of LAS. The property of the large momentum bite $p_{\text{max}}/p_{\text{min}} = 1.3$ enabled us to measure the QES peaks up to 28° with only 3 magnetic rigidity sets.

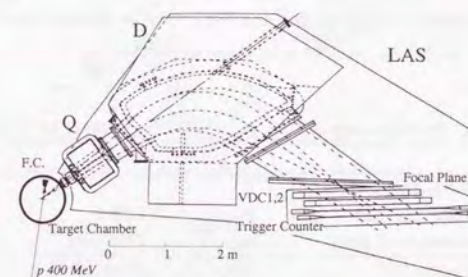


Fig. 2-14: Schematic view of Large Acceptance Spectrograph(LAS). The spectrograph LAS consists of a quadrupole magnet and a dipole magnet. LAS is designed to analyze the momentum of particles up to 1 GeV/c, which corresponds to a kinetic energy of a little more than 400 MeV in case of protons.

2.5.2 Coordinate system

Coordinate frames of the particles at the target and at the detection plane are defined as shown in Fig. 2-15. The zx plane coincides with the symmetry plane of the spectrometer. A central ray is defined as the trajectory of a particle that emerges from the center of the target in the symmetry plane of the spectrometer. Central rays for the different values of p/B reach the focal plane at different positions, where p is the momentum of the particle and B is the magnetic field of the spectrometer. An optical axis is defined as the central ray that passes through the center of the focal plane.

The coordinate frame at the target position is shown in Fig. 2-15B. The z axis is defined along the optical axis. The direction of the particle is described by two angles a_0 and b_0 , where a_0 (b_0) is the angle between the z axis and the projection of the trajectory on the xz (yz) plane. With these definitions, a_0 is the angle deviation from the central scattering angle (θ_{LAS}) and b_0 is the angle deviation of the out-of-reaction-plane angle. All coordinates in the target frame are denoted with the subscript "0". It is convenient to denote the angles as their tangent values, $a_0 = dx_0/dz_0$ and $b_0 = dy_0/dz_0$.

The coordinate frame at the detection plane is shown in Fig. 2-15C. The z axis is defined to the direction normal to the detection plane. The coordinates in this frame are denoted with the subscript "f".

The optical axis satisfies $x_f = 0$, $y_f = 0$, and $b_f = 0$ on the detection plane and $a_0 = 0$, $y_0 = 0$, and $b_0 = 0$ at the target position for the particles with $t_0 = 0$. A momentum ratio t_0 will be defined in subsection 2.5.4. The angle a_f has a nonzero value for the optical axis. The angle a_f for $x_f = 0$ (between the optical axis and the z axis) is denoted by Ψ . This angle for LAS is 54.04° (listed in table 2-6, together with other specifications.)

Table 2-6: Specifications of LAS and the VDC counters for LAS.

LAS			
Dipole magnet			
maximum field	B_{max}	1.68 T	
central orbit radius	r_0	1750 mm	
Solid angle	$\Delta\Omega$	20 msr	
Momentum bite	p_{max}/p_{min}	1.3	
Momentum resolution	$\delta p/p$	1/5000	
Focal plane angle	Ψ	54.04°	
VDC			
Sensitive area	1700 mm (x) × 350 mm (y)		
Anode			
Structure	X-U-V		
sense wire spacing	6 mm (X), 7mm (U,V)		
tilt angle of wires	0° (X), 31° (U), -31° (U)		
number of sense wires	272 (X), 256 (U,V)		
Anode to Cathode distance	10 mm		

2.5.3 Detector system

The detector system [32], located at the focal plane position of LAS, consists of two vertical drift chambers (VDC1, VDC2) and two planes of trigger scintillator. A schematic layout of the

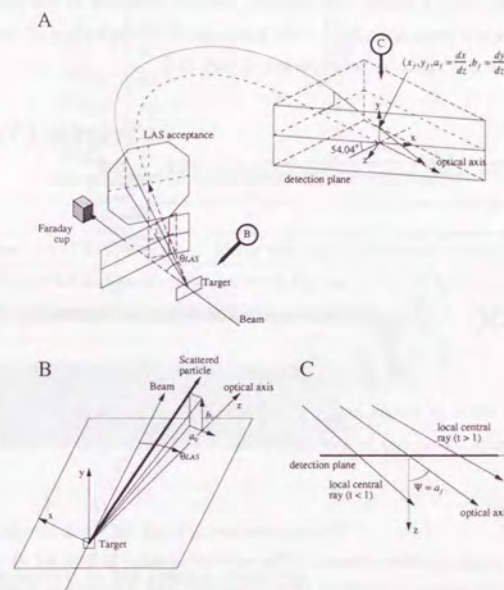


Fig. 2-15: Definition of the coordinate frames of LAS. Overview (A), frames at the target (B) and frames at the focal plane (C).

system is shown in Fig. 2-16.

Each VDC consists of three detection planes denoted by X, U, and V. The distances between the X plane and the U plane and between the U plane and the V plane are 20 mm. Since the wires of the X-planes are parallel to the y -axis, the x_f and a_f coordinates of the particle are determined by the X-channel numbers directly. The wires of the U(V)-planes are inclined at an angle $\gamma = -31^\circ (-\gamma)$ with respect to the y -axis. Therefore the U(V)-channel numbers themselves cannot determine the y_f or b_f coordinates. The y_f and b_f coordinates of the particle are determined from the combination of two of X, U, and V-channel numbers. With the information of more than 4 planes, the position and the direction of the particle (x_f, y_f, a_f, b_f) are obtained at the detection plane. The geometrical configuration of the VDC counter is summarized in table 2-6. Details are reported in Ref. [32].

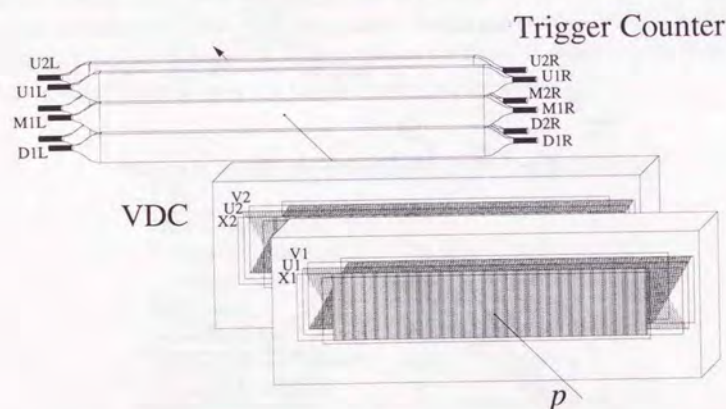


Fig. 2-16: Focal plane counter system. The counter system is located at the focal plane of LAS. It consists of 2 planes of Vertical Drift Chamber and 2 planes of trigger counter. Each VDC consists of three detection planes denoted as X, U, and V. The wires in the X plane are parallel to the y axis while the wires in the U (V) plane are inclined at an angle of 31° (-31°) with respect to the y axis.

2.5.4 Trace back technique

Using a trace back matrix, we obtain information (t_0, a_0, y_0, b_0) of a scattered particle at the target position. A momentum ratio t_0 is defined as $t = p/p_0 - 1$, where p_0 is a corresponding momentum at the central trajectory determined by the LAS dipole magnetic field B_D .

The trace back matrix was determined by Matsuoka and his collaborators [34] beforehand

Table 2-7: Target thickness for the (p, p') reaction measurement and calculated energy loss of the 400 MeV protons in the target.

Target	thickness [mg/cm ²]	energy loss [keV]
CH ₂	51.10	170
CD ₂	75.76	250
⁶ Li	48.1	120
⁷ Li	41.5	100
⁹ Be	99.41	240
¹² C	30.89	85
¹³ C	97.0	260
^{nat} Ca	39.7	95
^{nat} Cu	44.67	94
¹⁸¹ Ta	33.3	53
²⁰⁸ Pb	32.3	48

using protons from the $H(p, p)$ reaction. The scattering angles were selected by the collimator at the entrance of the LAS. Correlations between (t_0, a_0, y_0, b_0) and (x_f, a_f, y_f, b_f) were fitted by up to 4th order polynomials.

2.5.5 Targets

The thicknesses of targets for the (p, p') experiments are shown in table 2-7. The thickness was determined from the requirement that the energy loss of the proton was less than 250 keV.

2.6 Data analysis for the (p, p') measurement

2.6.1 Event selection in the trigger counters

Proton events are selected by using two light outputs from the upstream and downstream trigger scintillators. The total light output in each trigger counter is derived by geometrical means as

$$\begin{aligned} L_F &= \sqrt{L_{1L}L_{1R}}, \\ L_B &= \sqrt{L_{2L}L_{2R}}. \end{aligned} \quad (2-23)$$

Figure 2-17 shows the relation between the two light outputs. We can clearly recognize and select the proton events.

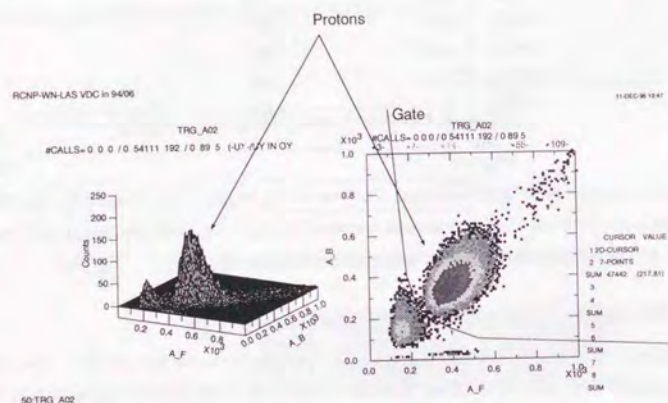


Fig. 2-17: Proton events are selected by light output information from trigger scintillators. The horizontal(vertical) axis in the right frame indicates a product of light outputs from both sides of forward (backward) counter. The solid line indicates the gated area for proton events. In the left frame, an isometric picture for the same histogram is shown.

2.6.2 Event selection in the VDC counters

The particles are expected to pass through the VDC counters with an angle of incidence around the focal plane angle, $\Psi=54.04^\circ$. With the setting listed in table 2-6, an averaged number of wires with signal generated is expected to be 4.6 for the X plane as

$$10[\text{mm}] \times 2 \times \tan(54.04^\circ)/6[\text{mm}] = 4.6. \quad (2-24)$$

Figure 2-18 shows a schematic picture of signals generated and their typical drift times by the protons passing through the VDC plane. Such a signal sequence is called a cluster. More precisely, (1) more than 3 wires have signals and are located sequentially, but (2) one wire in the sequence is allowed not to have signals, and (3) the information has consistent residual information which can be derived by fitting the drift times of more than 3 wires. The consistency in (3) means the time structure from the wires in the sequence satisfies at least the relation

$$\cdots > T_{i-2} > T_{i-1} > T_i < T_{i+1} < T_{i+2} < \cdots, \quad (2-25)$$

where the i th wire is the nearest to the particle trajectory shown in the bottom frame of Fig. 2-18.

The particle path is determined from the event with one or more clusters for each plane. The residuals for position and direction of the X1 plane are given by

$$\begin{aligned} r_p^{X1} &= |x_1 - (x_2 - dx_2/dz \times (z_2 - z_1))|, \\ r_q^{X1} &= |dx_1/dz - dx_2/dz|, \end{aligned} \quad (2-26)$$

where $(x_1, z_1, dx_1/dz)$ is the position and the direction from the cluster in the X1 plane. The left frame of Fig. 2-19 shows results of the residual for position at X2. The event in which one of the residuals r_p has a larger value than r_p^{MAX} is rejected. In this analysis we use 21 mm for r_p^{MAX} which is indicated by arrows in the left frame of Fig. 2-19.

When more than one clusters are detected, we select the cluster which has the minimum r_p value.

2.6.3 Efficiency of the VDC counters

The position dependent detection efficiency of the individual VDC planes is obtained by using the residual information. In general, the detection efficiency of each VDC planes is obtained within the single VDC counter: the detection efficiency of the X plane is determined from information of the U and V plane for the X-U-V configuration.

In the experiment, on the contrary, two pairs (X1,U1 and X2,U2) of planes were used and V1 and V2 plane were not used because of restrictions of circuits for data taking. Therefore we obtain the detection efficiency by the following way instead of the general method.

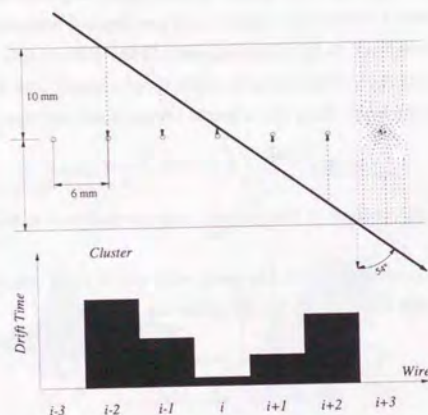


Fig. 2-18: Schematic view of the cluster and typical drift time sequence of the cluster. In the upper frame, the cluster generated by a particle passing through the wire chamber is shown. Expected angles of the particles with respect to the chamber are distributed around 54.04° , the angle between the central trajectory and the focal plane. In the lower frame, drift times of the wires in the cluster shown in the upper frame is schematically described as a function of the wire number. The drift time sequence, which is the relation of the drift time and the wire number in the cluster, is expected to appear in the form of the letter "V" described in Eq. 2-25.

The efficiency is defined by the ratio of number of particles detected over the number of particles passing through. The efficiency of the X2 plane at position x_2 is defined as

$$\epsilon_{X2}(x_2) = \frac{N_{\text{hit}}(x_2)}{N(x_2)}. \quad (2-27)$$

Here N is a number of events in which the particle is detected in the X1 plane and is expected to pass through at position x_2 in the X2 plane. N_{hit} is a number of events in which the particle is detected in the X1 plane and is also detected at position x_2 in the X2 plane. The number N is obtained from information of position and direction at the X1 plane in this case.

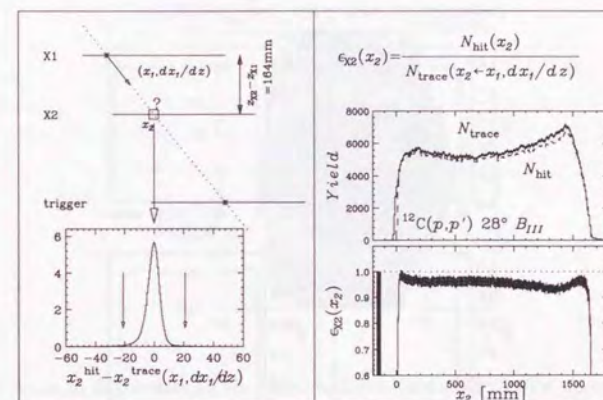


Fig. 2-19: A method to obtain the detection efficiency of the X2 plane from the information in the X1 plane, and an example of the obtained efficiency.

In Fig. 2-20, the efficiency for each plane is obtained using all data. The averaged value of the efficiency was about 95% for each plane. Consequently, the tracking efficiency was about 81%.

2.6.4 Solid angle

In-plane (a) and out-of-plane (b) angles are derived from information on the focal plane by the trace back technique. Figure 2-21 shows a sample of the (a, b) distribution. The distribution seems to reproduce the designed solid angle of LAS which is indicated by regions surrounded by solid lines. The solid angle of the detector has a large ambiguity of about 20% depending on a cut-off value for b .

In order to investigate the solid angle precisely, we measured the $\text{CH}_2(p, p)$ reaction with the same configurations of the LAS angles θ_{LAS} as other targets. We selected the same (a, b)

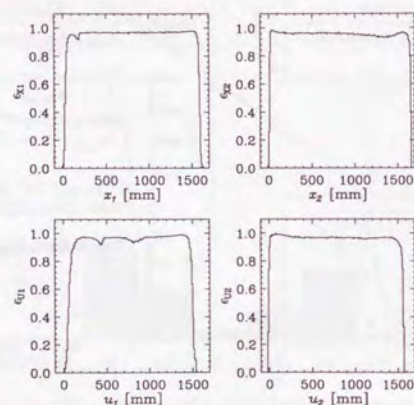


Fig. 2-20: Position dependence of detection efficiency of each plane, X1, U1, X2, and U2. The detection efficiency for each plane is obtained from Eq. 2-27 using all data available. The horizontal axes indicate positions in the planes. The averaged value of the efficiency is about 95% for each plane.

regions surrounded by the dashed line in Fig. 2-21. By comparing the experimental data of the $H(p, p)$ reaction with results of the phase shift analysis, the solid angle of the selected regions is calibrated. In order to confirm the calibration of the solid angles, we compare cross sections of the $^{12}\text{C}(p, p)$ elastic scattering with experimental results obtained at LAMPF[35]. Figure 2-22 shows the comparison. Our data agreed with the previous data within statistical uncertainties.

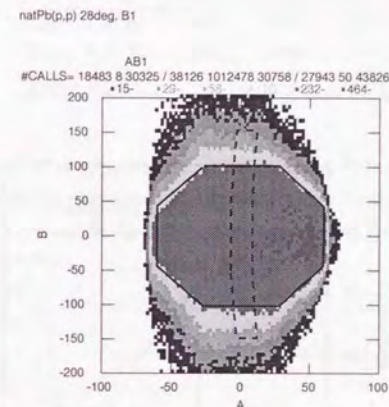


Fig. 2-21: An (a, b) distribution on the target is shown. The angle (a, b) is traced back from a detected position and direction of each particle at the focal plane. The unit for both horizontal and vertical axes is milli-radian. The solid line indicates the designed solid angle. The dashed line indicates the selected solid angle.

2.6.5 Magnetic rigidity

The momentum-analyzed range was covered by a series of sets, up to three sets, of magnetic rigidities. The higher momentum boundary of the range was the elastic scattering region of $\omega \sim 0$ MeV while the lower boundary is the region well above the QES peak which depends on the scattering angle. In the case of measurements of the 28° scattering, the energy region is about $\omega \sim 250$ MeV. The magnetic field sets are shown in table 2-8.

For ^{12}C , $^{\text{nat}}\text{Ca}$, and $^{\text{nat}}\text{Pb}$ targets, we used a B_I set for 12° and 16° measurements, B_I and B_{II} sets for 20° and 24° , and B_I , B_{II} , and B_{III} sets for measurements of 28° scattering. For the CD_2 target, we use the same sets as for the measurement of the ^{12}C target except the B_{III} set for the 28° measurement because the QES peak of the ^2H was well covered by the measurements with the B_I and B_{II} sets. For other targets, we used the B_I set for each angle

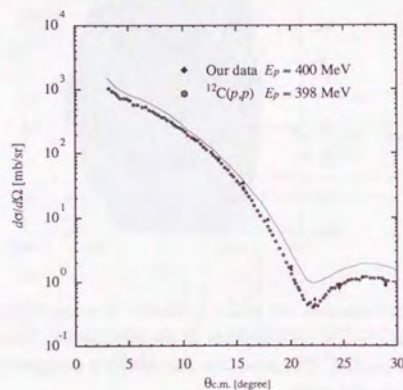


Fig. 2-22: Cross section for $^{12}\text{C}(p,p)$ elastic scattering is compared with data measured at LAMPF[35] for $E_p = 398$ MeV.

because of limitation of the beam time.

Table 2-8: Three magnetic field sets were used. E_{ref} is the proton energy at the reference trajectory. E_{MAX} (E_{MIN}) is the higher (lower) limit of proton energy in the magnetic field set.

set	B_D [T]	E_{ref} [MeV]	E_{MAX} [MeV]	E_{MIN} [MeV]
		$\rho=1.9$ m	2.0 m	1.5 m
B_I	1.6728	400	435	264
B_{II}	1.4178	300	328	196
B_{III}	1.1906	220	240	142

Figure 2-23 shows the $^{\text{nat}}\text{Ca}(p,p')$ spectrum at 28° obtained by the three magnetic field sets. A vertical axis indicates yields normalized by the total charge. The yields are consistent with each other at the region covered by neighboring two magnetic field sets, $[B_I, B_{II}]$ or $[B_{II}, B_{III}]$, within statistical uncertainties.

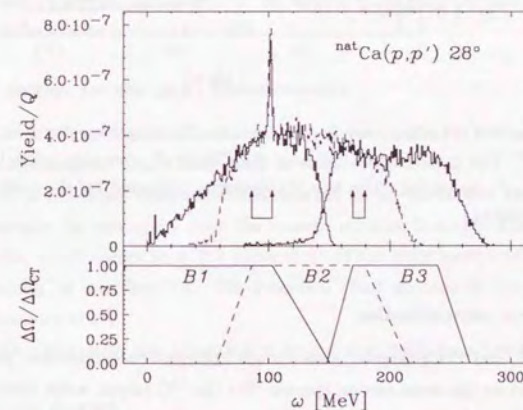


Fig. 2-23: $^{\text{nat}}\text{Ca}(p,p')$ spectrum at proton energy of 400 MeV and 28° . In order to obtain the high energy transfer up to 250 MeV, we used three magnetic field sets. Yields normalized by total charge from different field sets were consistent within the statistical uncertainty. For each magnetic field set, the relative solid angles to that of the central trajectory are schematically shown in the lower frame.

2.6.6 Spectra for ^1H and ^2H

Cross section spectra for the $^1\text{H}(p,p)$ and $^2\text{H}(p,p')$ reactions were obtained by subtracting the ^{12}C contribution from the CH_2 , $\text{CD}_2(p,p')$ spectra. A normalization factor is adjusted for all angles to produce the best subtraction of three prominent peaks in $^{12}\text{C}(\text{g.s.}, 4.44 \text{ MeV}, \text{ and } 9.65 \text{ MeV})$.

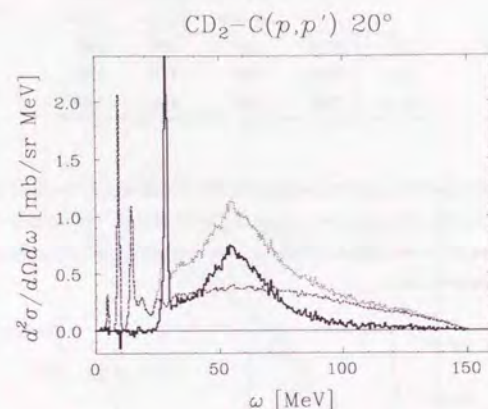


Fig. 2-24: Subtraction of carbon contribution from the $\text{CD}_2(p,p')$ spectrum at proton energy of 400 MeV and 20° . The dotted curve indicates the $\text{CD}_2(p,p')$ spectrum while the dashed curve indicates the $\text{C}(p,p')$ spectrum. The $\text{D}(p,p')$ spectrum indicated by the solid line is obtained from these two spectra.

2.6.7 Hydrogen contamination

For the ^6Li , ^7Li , and ^{nat}Ca targets, some surface hydrogen contamination, probably from hydroxide, is evident on the cross section spectra. For the ^{13}C target, some hydrogen contamination, probably bond for baking the ^{13}C powder, is also evident. Such a hydrogen contamination appears as a narrow peak superimposed on the smoothly varying cross section. The resulting incremental cross section is readily identified and subtracted using the measured $^1\text{H}(p,p)$ spectra.

2.7 Systematic errors

2.7.1 Cross section for the (p,n) measurements

The main sources of systematic uncertainty for the (p,n) cross sections are the target thickness, the total charge, and the neutron detection efficiency of the neutron detector.

The ambiguity of the target thickness is less than 5% for all targets. The normalization factors between the current integrator and the beam line polarimeter agrees within 3%. The uncertainty of the neutron detection efficiency is determined from the uncertainty of the cross section of the $^7\text{Li}(p,n)^7\text{Be}(\text{g.s.} + 0.43 \text{ MeV})$ reaction which is used for the calibration. The uncertainty of the cross section is 6.7%. We measured the cross section of the reaction within a statistical error of 1%. Therefore, combining these three uncertainties, 5% for target thickness, 6.7% for detection efficiency and 3% for the beam charge integration, the overall systematic uncertainty is estimated to be less than 8.9% for all targets except for the ^{13}C measurement.

For the ^{13}C measurement an ambiguity which originates from subtraction methods is taken into account. We subtract the ^{12}C contribution from the ^{13}C spectra with references of the peak for the $^{12}\text{C}(p,p)^{12}\text{C}(\text{g.s.})$ at 12° , 20° and 28° . The ambiguity of the normalization factors obtained using the three angles is 8%. By adding this ambiguity, the overall systematic uncertainty is estimated to be less than 12%.

2.7.2 Cross section for the (p,p') measurements

The main sources of a systematic uncertainty of the cross section for the (p,p') measurements are the target thickness, the total charge, and the solid angle of LAS.

The ambiguity of the target thickness is less than 8% for all the targets. As is the case of the (p,n) measurements, the ambiguity from the current monitor is within 3%. The uncertainty of the solid angle, which comes from the uncertainty of the cross section of the $\text{H}(p,p)$ of the calibration reaction, is less than 1%. We measured cross sections of the reaction within a statistical uncertainty of 1%.

The systematic uncertainty was estimated to be less than 8.8% for all targets.

2.7.3 Analyzing powers

The source of a systematic error for the analyzing powers of the (p,n) and (p,p') reactions is the uncertainty of polarization of the beam. The beam polarization was determined with a statistical error less than 2% for every run. The uncertainty of the analyzing power of the beam line polarimeter is less than 2.5% which originates from the solutions of the phase shift analysis.

The overall systematic uncertainty of the analyzing power is estimated to be less than 3.2%.

3 Experimental results

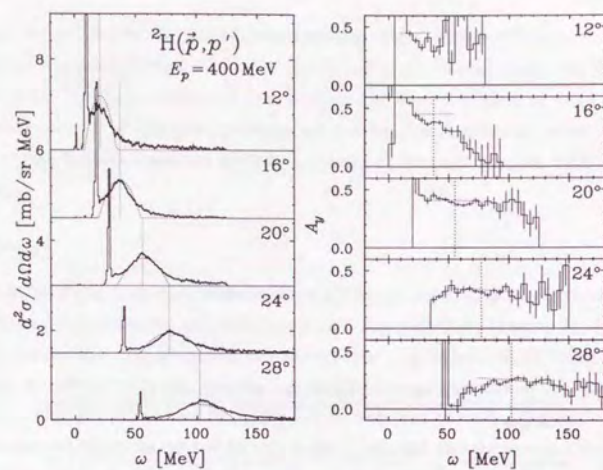
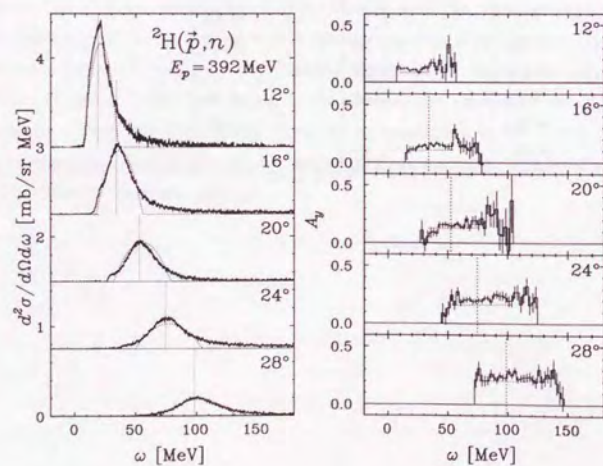
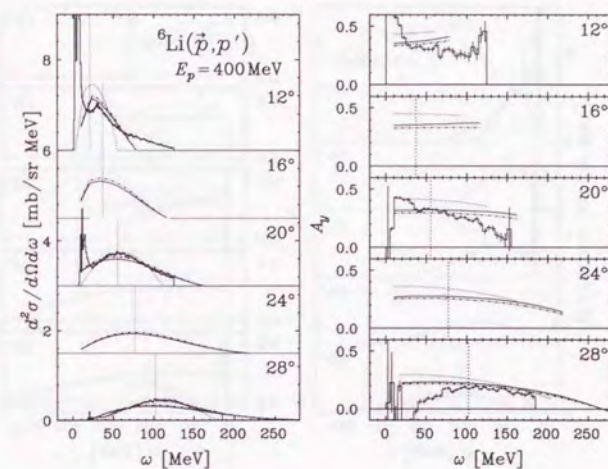
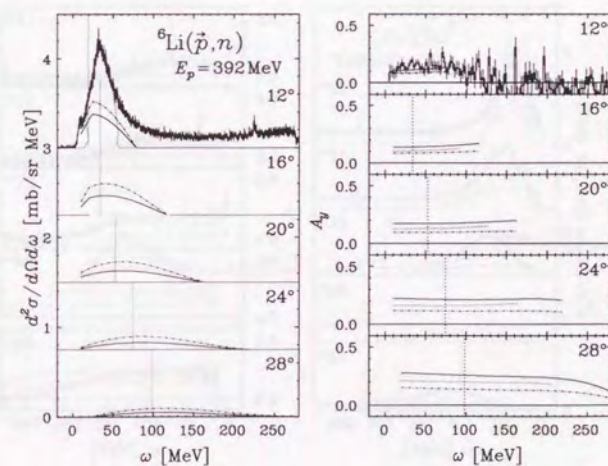
In this section we present the experimental results. First, double differential cross sections $d^2\sigma/d\Omega d\omega$ and analyzing powers A_y for the (p, n) and (p, p') measurements are shown. Then, peak positions for the QES process are derived from the double differential cross section spectra. Analyzing powers at the peak position are derived from analyzing power spectra. We compare the peak positions and the analyzing powers at the peak position with those for free NN scattering.

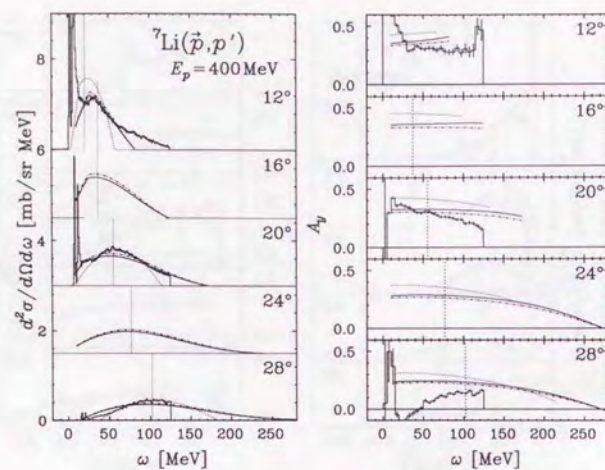
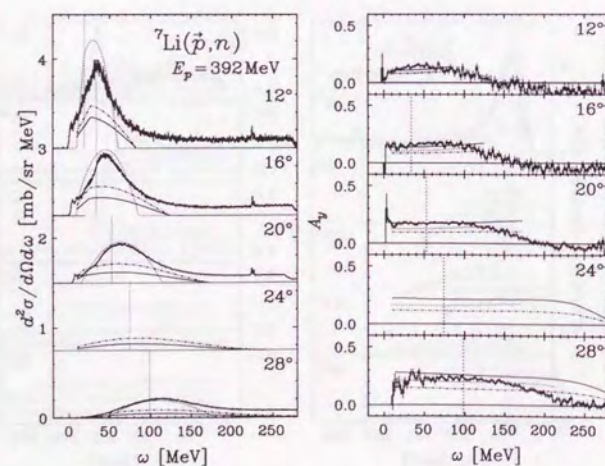
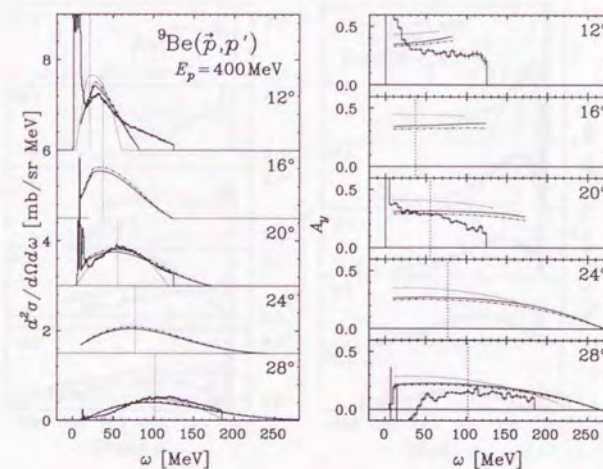
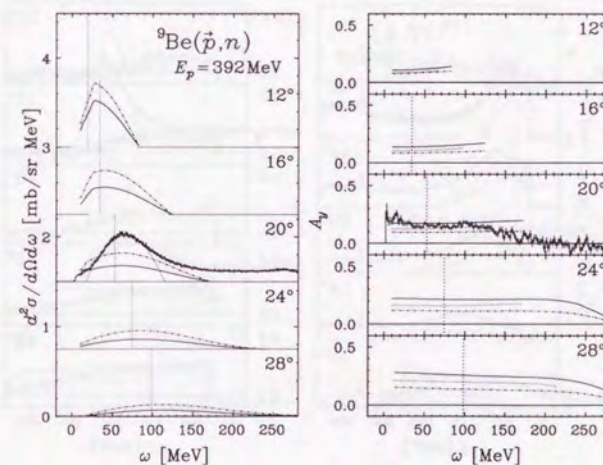
3.1 Spectra

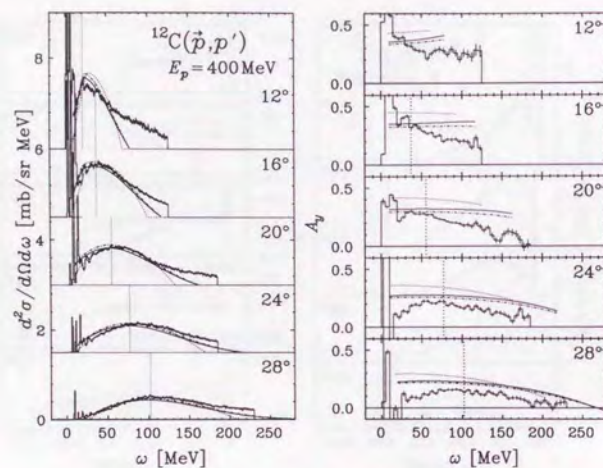
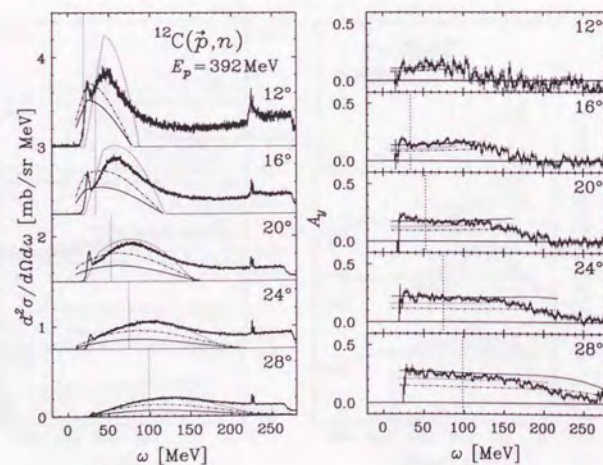
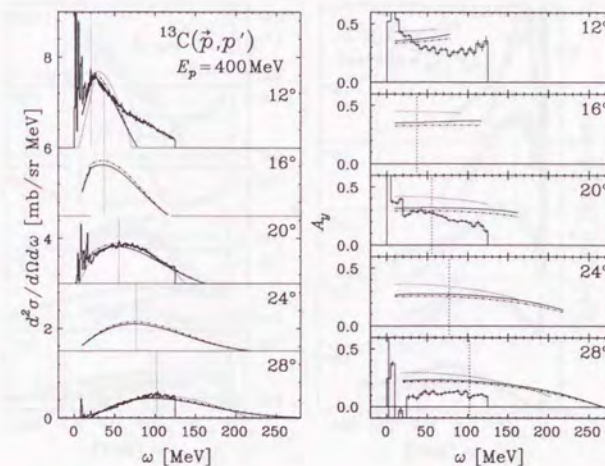
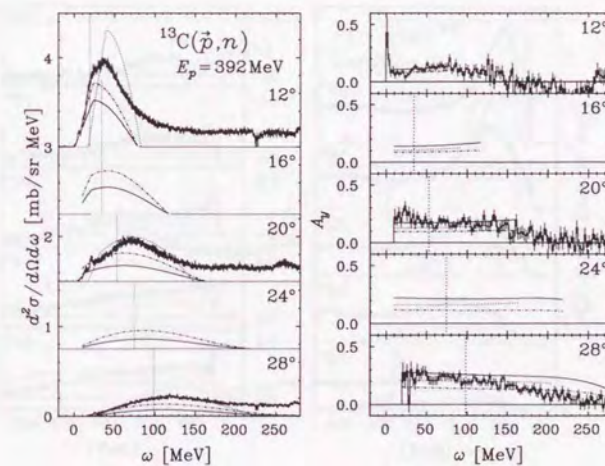
The cross section and analyzing power spectra for the (p, n) and (p, p') reaction are presented. Correspondence between figures and reactions is shown in table 3-1. In every figure, the double differential cross sections (the analyzing powers) are shown in the left (right) frame as a function of the energy transfer ω . For the 400 MeV and 392 MeV measurements, the spectra for 12° , 16° , 20° , 24° , and 28° are shown from the top to the bottom in each frame. For the 295 MeV measurements, the spectra for 15° , 20° , 25° , 30° , and 35° are shown. Vertical dotted lines in both the cross section and analyzing power frames indicate positions predicted by the kinematics of free NN scattering. Dotted lines in the cross section frames indicate the results of Fermi gas model calculations. Dotted lines in the analyzing power frames indicate the result of EFGM calculations described in section 4.3 in which the kinematics between two nucleons are explicitly taken into account. Solid (dot-dashed) lines in both the cross section and analyzing power frames indicate the results of the RPWIA calculations with a pseudovector (pseudoscalar) parameterization of the πN coupling. We describe the details of these calculations in section 4.4. The peaks around $\omega \sim 230$ MeV found in the cross section spectra of the (p, n) reactions correspond to the γ flush which originates from the π_0 production in the target. The number of the peaks is generally equal to the number of the neutron counters. The length of the flight path is slightly different for every counter.

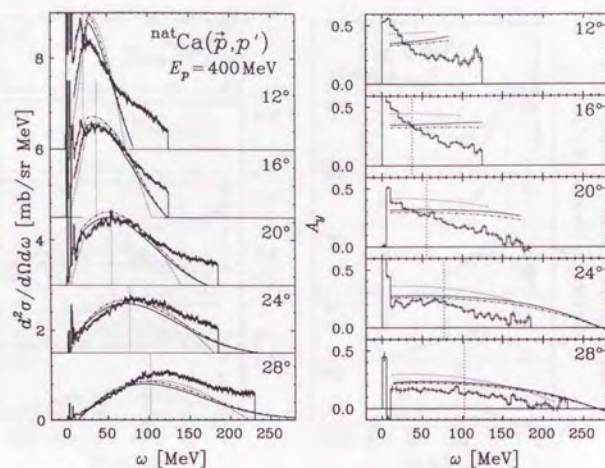
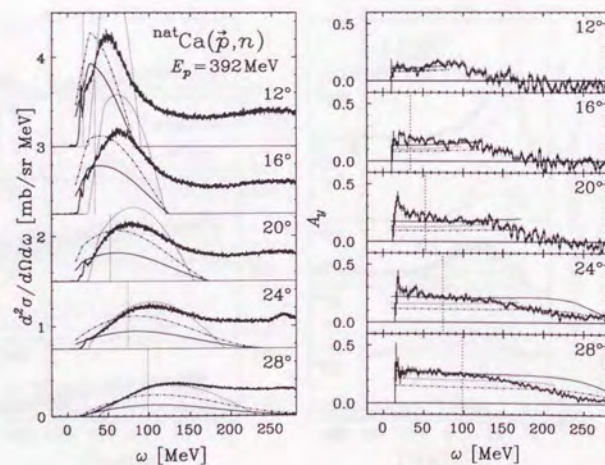
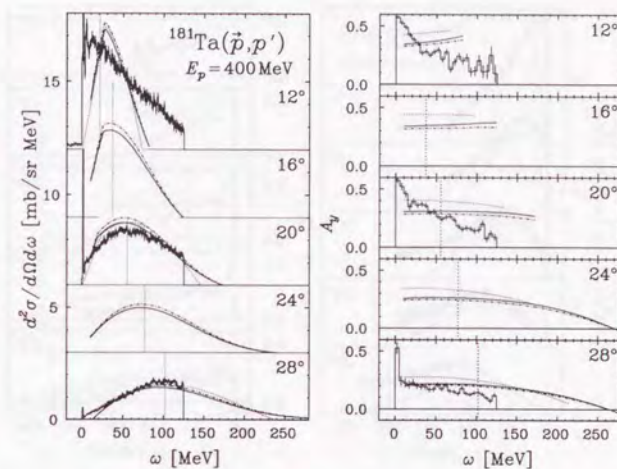
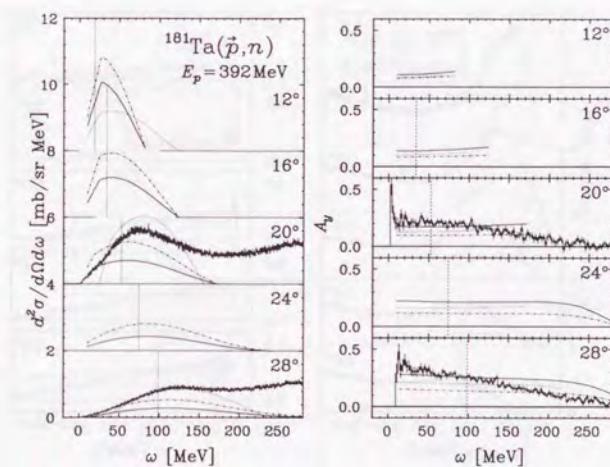
Table 3-1: Figure list for the reaction

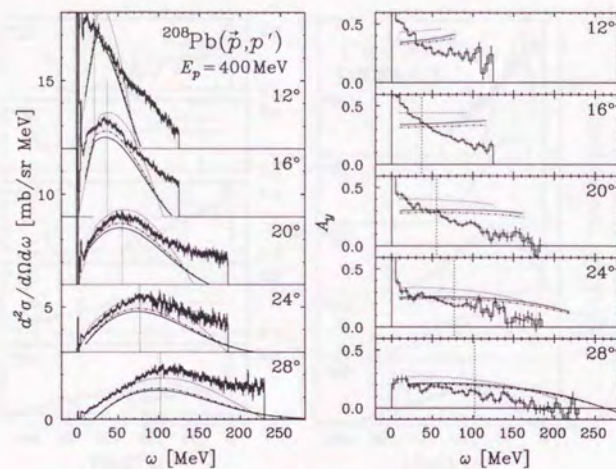
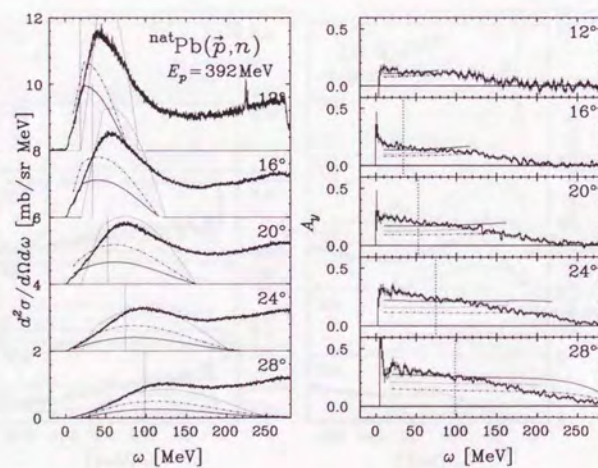
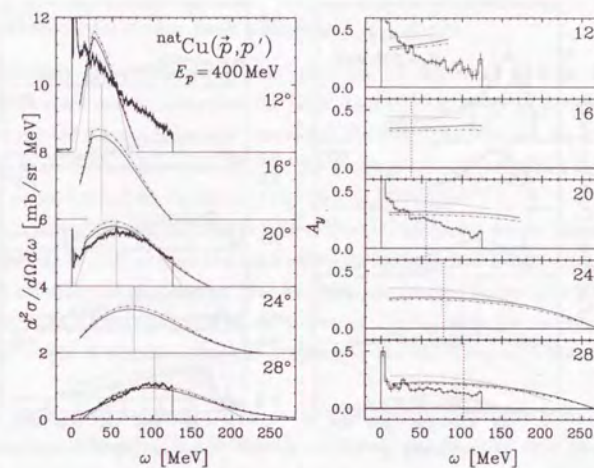
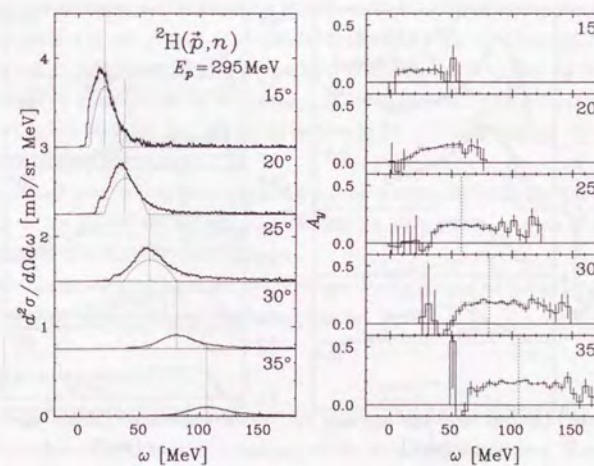
target	reactions		
	(p, p') 400 MeV	(p, n) 392 MeV	(p, n) 295 MeV
^2H	Figure 3-1	Figure 3-2	Figure 3-20
^6Li	3-3	3-4	
^7Li	3-5	3-6	
^9Be	3-7	3-8	
^{12}C	3-9	3-10	3-21
^{13}C	3-11	3-12	
$^{\text{nat}}\text{Ca}$	3-13	3-14	3-22
$^{\text{nat}}\text{Cu}$	3-19		
^{181}Ta	3-15	3-16	
$^{\text{nat}}\text{Pb}$		3-18	
^{208}Pb	3-17		

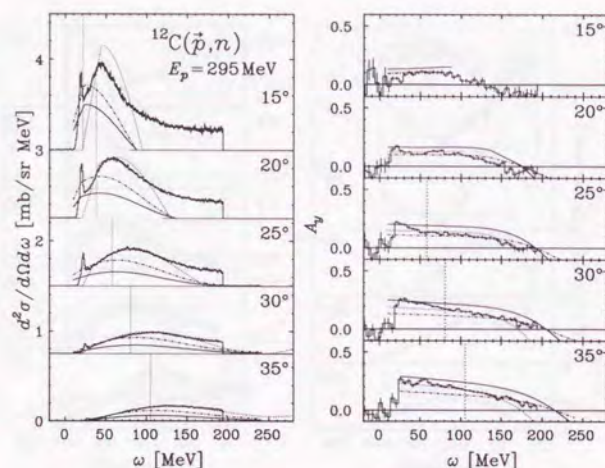
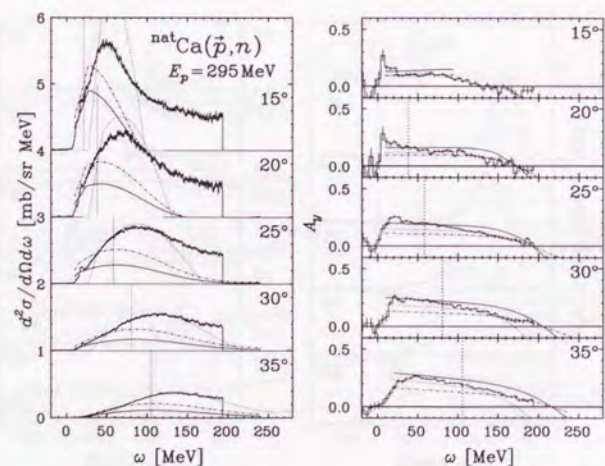
Fig. 3-1: ${}^2\text{H}(p, p')$ at proton energy of 400 MeVFig. 3-2: ${}^2\text{H}(p, n)$ at proton energy of 392 MeVFig. 3-3: ${}^6\text{Li}(p, p')$ at proton energy of 400 MeVFig. 3-4: ${}^6\text{Li}(p, n)$ at proton energy of 392 MeV

Fig. 3-5: ${}^7\text{Li}(p, p')$ at proton energy of 400 MeVFig. 3-6: ${}^7\text{Li}(p, n)$ at proton energy of 392 MeVFig. 3-7: ${}^9\text{Be}(p, p')$ at proton energy of 400 MeVFig. 3-8: ${}^9\text{Be}(p, n)$ at proton energy of 392 MeV

Fig. 3-9: $^{12}\text{C}(p, p')$ at proton energy of 400 MeVFig. 3-10: $^{12}\text{C}(p, n)$ at proton energy of 392 MeVFig. 3-11: $^{13}\text{C}(p, p')$ at proton energy of 400 MeVFig. 3-12: $^{13}\text{C}(p, n)$ at proton energy of 392 MeV

Fig. 3-13: $^{nat}\text{Ca}(p, p')$ at proton energy of 400 MeVFig. 3-14: $^{nat}\text{Ca}(p, n)$ at proton energy of 392 MeVFig. 3-15: $^{181}\text{Ta}(p, p')$ at proton energy of 400 MeVFig. 3-16: $^{181}\text{Ta}(p, n)$ at proton energy of 392 MeV

Fig. 3-17: $^{208}\text{Pb}(p, p')$ at proton energy of 400 MeVFig. 3-18: $^{\text{nat}}\text{Pb}(p, n)$ at proton energy of 392 MeVFig. 3-19: $^{\text{nat}}\text{Cu}(p, p)$ at proton energy of 400 MeVFig. 3-20: $^2\text{H}(p, n)$ at proton energy of 295 MeV

Fig. 3-21: $^{12}\text{C}(p, n)$ at proton energy of 295 MeVFig. 3-22: $^{\text{nat}}\text{Ca}(p, n)$ at proton energy of 295 MeV

3.2 Peak position and analyzing power at the peak position

3.2.1 Method to determine peak positions

From the double differential cross section spectrum, we derive the peak positions. Figures 3-23 and 3-24 show how to determine the peak positions. In order to determine the peak position, we use the Gaussian function, instead of the Fermi gas response function which will be discussed in section 4.2, since the shape of the Fermi gas response function around the peak can be well-approximated by the shape of the Gaussian function.

The peak position is determined in the following way. Firstly, we use the Gaussian function. We select the region to fit around the peak where the cross section is larger than that of 0.75 times of the maximum of cross section. For example, the selected region is $55 \text{ MeV} < \omega < 105 \text{ MeV}$ for the $^{12}\text{C}(p, n)$ reaction at 20° , and $70 \text{ MeV} < \omega < 130 \text{ MeV}$ for the $^{12}\text{C}(p, p')$ reaction at 28° . The width of Gaussian shape is sensitive to the fitted region, while the centroid is insensitive.

Secondly, we estimate the contribution of the cross section from other mechanisms besides QES. The contribution comes mainly from a multi-step process. The cross section from the multi-step process is generally sensitive to the total cross section in medium (see appendix D) and it is difficult to estimate not only the shape but also the amplitude of the response quantitatively. In this work we investigate the sensitivity of the peak position to additional functions which are assumed to represent the multi-step process. We have used a polynomial function and a step function. The region to fit with these two functions was selected as follows. The lower boundary is set at next to the inelastic discrete peak with highest ω . The higher boundary is set at sufficiently high ω region where the slope of the cross section is equal to zero. As a result, the regions are $35 \text{ MeV} < \omega < 185 \text{ MeV}$ for the $^{12}\text{C}(p, n)$ reaction at 20° and $40 \text{ MeV} < \omega < 210 \text{ MeV}$ for the $^{12}\text{C}(p, p')$ reaction at 28° . The results are insensitive to the selection of the higher boundaries.

It is found for all targets that the change of the peak position by using the different functions for fitting is within 2 MeV for the spectra at 20° and 5 MeV for the spectra at 28° . We treat these ambiguities as systematic uncertainties.

After determining the peak position, we derive analyzing powers at the peak positions averaging over 20 MeV around the peak position using Eq. 2-14.

3.2.2 q dependence

In Figs. 3-25 – 3-28, the peak positions (left frame) and the analyzing powers at the peak positions (right frame) are shown as a function of the momentum transfer q . Error bars reflect the statistical uncertainties only.

First of all, it is worth mentioning that the results for the ^2H target in Fig. 3-28 are consistent with the free NN scattering except for the analyzing powers for the (p, n) reaction. The analyzing

powers for the free NN scattering, denoted as A_y^{free} , are obtained by the phase shift analysis[28]. We use the solution of SM89 throughout this thesis. The experimental results of the analyzing powers for the ${}^2\text{H}(p, n)$ reactions are enhanced from A_y^{free} .

Secondly, it is found that the peak positions for the (p, n) reaction of other targets are located at ω_{QE} higher than the position ω_f (dotted lines) predicted by the kinematics of free NN scattering.

The peak shifts from ω_f are almost constant with respect to q and the values are 25 MeV for ${}^{12}\text{C}$, 28 MeV for ${}^{\text{nat}}\text{Ca}$, and 23 MeV for ${}^{\text{nat}}\text{Pb}$.

The peak positions for the ${}^{\text{nat}}\text{Pb}(p, p')$ reactions almost agree with ω_f . The peak positions for ${}^{12}\text{C}$ and ${}^{\text{nat}}\text{Ca}$ are located at slightly higher ω than ω_f . The global A dependence of the peak shifts is also almost constant with respect to q , but for specific case the shifts for ${}^{12}\text{C}$ are 7 MeV and those for ${}^{\text{nat}}\text{Ca}$ are 3 MeV.

It is found that the analyzing powers for the (p, p') reactions are systematically reduced from A_y^{free} . Note that the referred value for the (p, p') scattering is obtained by averaging the $p + p \rightarrow p + p$ and $p + n \rightarrow p + n$ reactions.

On the other hand, the analyzing powers for the (p, n) reactions are slightly enhanced from A_y^{free} , and they are consistent with the analyzing powers for the ${}^2\text{H}(p, n)$ reactions for region of $q < 2.0 \text{ fm}^{-1}$.

3.2.3 A dependence

The mass number (A) dependence of the peak position at 20° is shown in Fig. 3-29.

For the (p, n) reaction the peak shifts from the value of ω_f increase as a function of mass number from 2 to 12. For the region of $A > 12$, the size of the peak shifts is almost constant. For the (p, p') reaction the peak shifts from the value of ω_f increase as a function of mass number from 2 to 12 in a similar manner with the (p, n) results. For the region of $A > 12$, the size of the peak shifts decreases slightly as a function of mass number from 12 to 208.

The mass number dependence of the analyzing powers at 20° and 28° is shown in Fig. 3-30. For the (p, p') reaction, the analyzing powers are reduced from the values of A_y^{free} at regions of $A > 12$. The ratio A_y/A_y^{free} decreases as the mass number increases from 2 to 12 and is almost constant in mass number larger than 12.

For the (p, n) reaction, the analyzing powers are almost constant at both 20° (filled diamonds) and 28° (open squares) as a function of A from 2 to 208. Comparing the results of the phase shift analysis at 20° which are indicated by a dotted line, the experimental results are slightly enhanced over all regions of A from 2 through 208. The experimental results are consistent with the results of the phase shift analysis at 28° which are indicated by a dot-dashed line.

It is found that the peak positions and the analyzing powers of the QES are independent of mass number for $A > 12$, except for the decreasing relation with respect to A for the peak

positions for the (p, p') reactions. In the region of $2 < A < 12$, the peak positions and the analyzing powers change gradually.

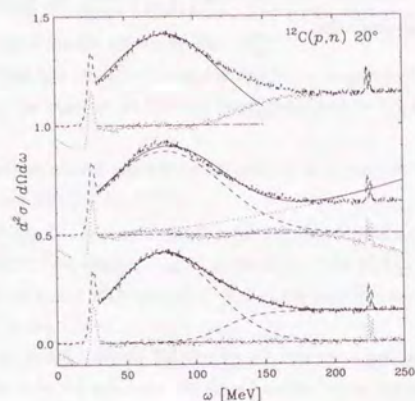


Fig. 3-23: The peak position is investigated using Gaussian (upper frame), Gaussian plus 2nd order polynomial function (middle), and Gaussian plus step function (lower). The dashed histogram is the experimental data and the dotted one is the difference from the fitted function. The fitted function indicated by the solid line is a summation of several functions (dashed or dotted lines). Note that the results using the exponential function are almost identical to those of the polynomial function.

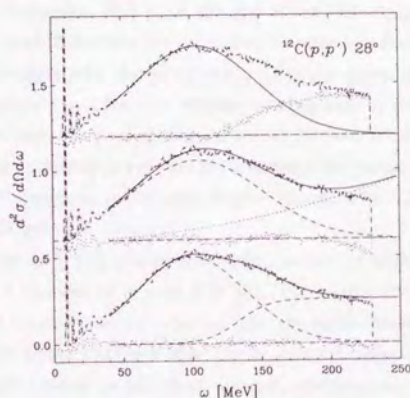


Fig. 3-24: Same figure as 3-23, but for the $^{12}\text{C}(p,p')$ reaction at 400 MeV and 28° .

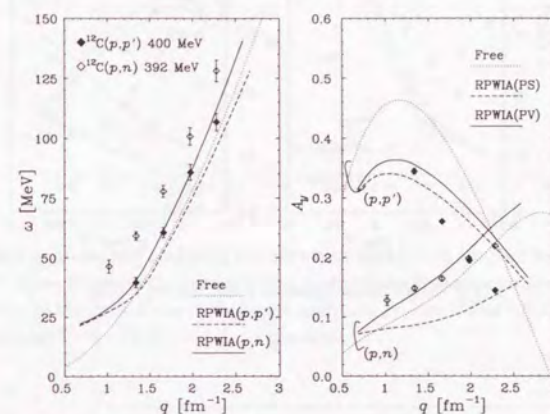


Fig. 3-25: The left frame shows peak positions (ω_{QE}) versus momentum transfer (q) for ^{12}C . The right frame shows momentum transfer dependence for analyzing powers around the peak positions. Filled diamonds indicate the $^{12}\text{C}(p,p')$ reaction at 400 MeV while opened diamonds indicate the $^{12}\text{C}(p,n)$ reaction at 392 MeV. In the left frame, the dotted line indicates the peak position for the Fermi gas model calculations. The solid line indicates the peak position for the (p,n) reaction calculated by the RPWIA. The dashed line indicates the peak position for the (p,p') reaction. The selectivity between a pseudoscalar coupling and a pseudovector coupling for the πN coupling does not influence the peak positions but only the amplitude of the cross section. In the right frame dotted lines indicate FGM results for analyzing powers around peak positions for the (p,n) and (p,p') reactions. Solid (dashed) lines indicate the RPWIA results with the pseudovector (pseudoscalar) coupling.

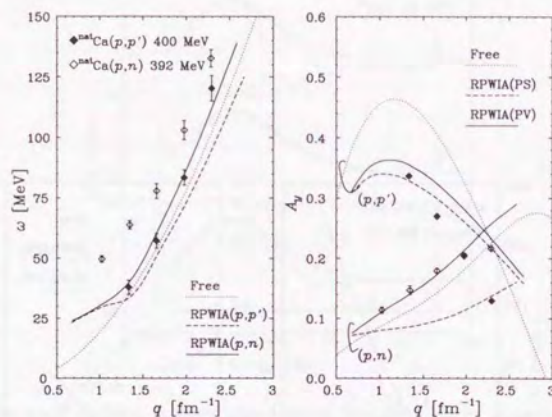
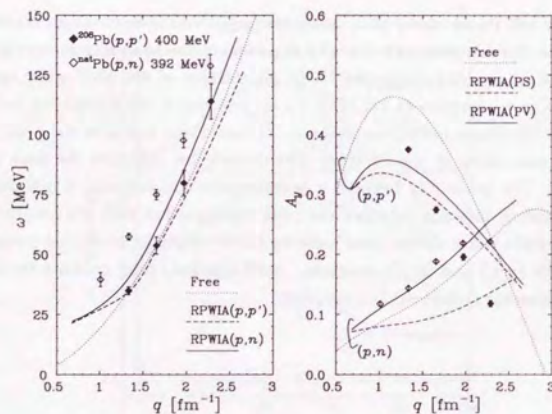
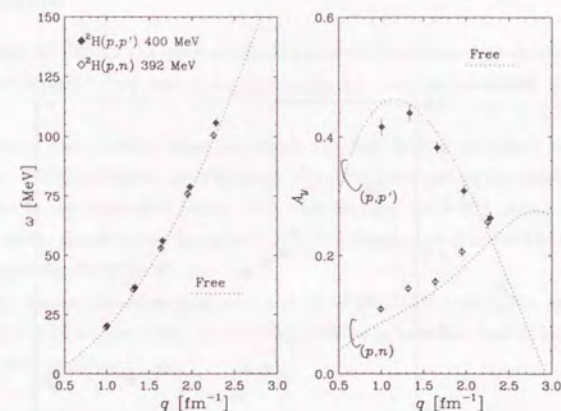
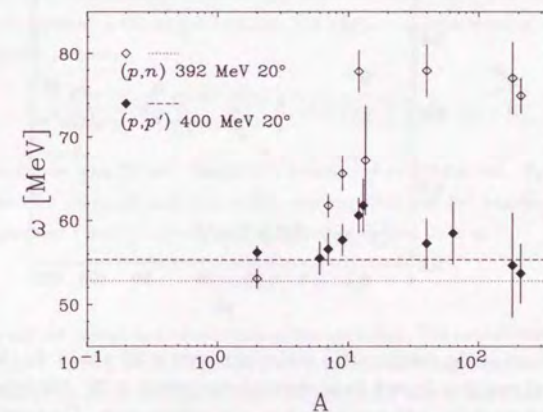
Fig. 3-26: Same figure as 3-25, but for ^{nat}Ca .

Fig. 3-27: Same figure as 3-25, but for Pb.

Fig. 3-28: Peak positions and analyzing powers versus momentum transfer for ^2H . The dotted line in the left frame indicates the peak position predicted by kinematics of free NN scattering. The dotted lines in the right frame indicate the analyzing powers of free NN scattering using a phase shift analysis for the (p,p') and (p,n) reactions.Fig. 3-29: Mass number dependence of the peak position at 20° for the (p,n) and (p,p') reactions. The NN kinematics for the (p,n) reaction at 20° and the (p,p') reaction at 20° yield different positions mainly because the initial proton energies are slightly different, 392 MeV and 400 MeV, from each other.

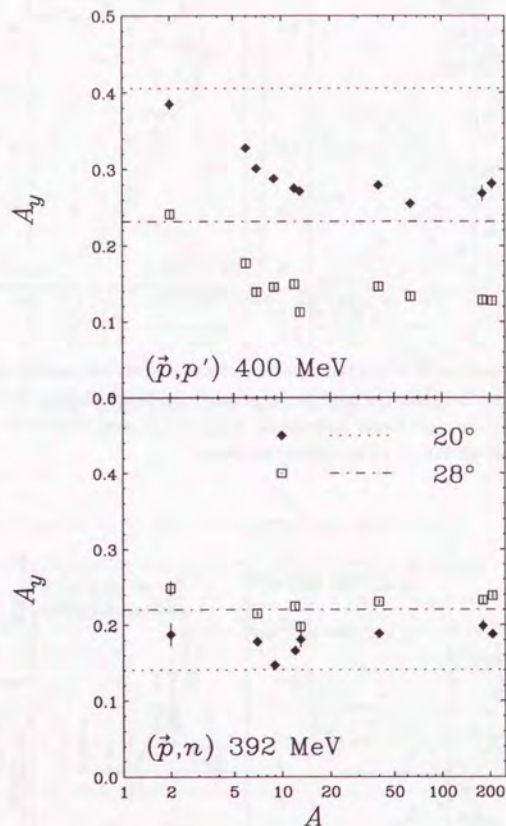


Fig. 3-30: Mass number dependence of the analyzing powers at 20° and 28° for the (p, n) (lower) and (p, p') (upper) reactions. In each frame the analyzing powers at 20° (filled diamonds) and at 28° (open squares) are shown with respect to A on a logarithmic scale. The dotted (dot-dashed) line for each frame indicates the result of a phase shift analysis for each reaction at 20° (28°).

4 Discussion

In this section we discuss the quasi elastic response within a standard reaction model based on the Glauber model, which uses the nuclear response function calculated in the Fermi gas model.

After describing the standard reaction model, we start from a simplified Fermi gas model (SFGM or only FGM) in which the NN amplitudes do not depend on the kinematics but have constant values in the laboratory frame. Next, we describe the PWIA which is equivalent to the extension of the simple Fermi gas model (EFGM). Finally, we describe the PWIA with the relativistic treatment (RPWIA).

We compare the experimental data with results of the FGM calculation and the RPWIA calculation, especially concentrating on the peak position of the cross section and the analyzing power at the peak position.

4.1 Standard reaction model

In electron scattering, the inclusive cross section given by the plane wave impulse approximation (PWIA) is proportional to the two-body (Mott) cross section times the nuclear response function $R(q, \omega)$. This model works very well for describing quasi elastic (e, e') scattering [41]. In the case of a nucleon (or composite particle) scattering, a similar formula is expected to hold for the cross section, modified only by a constant reduction factor to account for the attenuation of the projectile particle in the target nucleus. The nucleon-nucleus cross section then has the simple factorized structure,

$$\frac{d^2\sigma}{d\Omega d\omega} = A_{\text{eff}} \sum_{T,S} \frac{k'_1}{k_1} \text{Tr}\{f_{T,S}^\dagger(\vec{q}, s) f_{T,S}(\vec{q}, s)\} R_{T,S}(q, \omega), \quad (4-1)$$

where the sum is over spin (S) and isospin (T) transferred to the nucleus. $R_{T,S}$ is the response function in the (T, S) channel, and $f_{T,S}$ is the corresponding free NN amplitude. An invariant energy s for particles 1 and 2 is given by the Lorentz invariant form as

$$s = E_1 E_2 - \vec{k}_1 \cdot \vec{k}_2, \quad (4-2)$$

where (E_i, \vec{k}_i) are the energy and momentum of the particle i . The momentum k'_1 is that of the scattered particle 1'. The trace is taken over both projectile and target nucleon spins. A_{eff} is the effective number of nucleons interacting with the projectile, and is calculated by the Glauber model.

Spin observables are given as the ratio between the trace with corresponding spin operators and the trace without spin operators. Based on the assumption A_{eff} is constant among individual spin responses, the spin observables are not different from those of free NN scattering. Thus,

the analyzing power is given by

$$A_y = \frac{\sum_{T,S} \text{Tr}\{f_{T,S}^{\dagger}(\vec{q}) \sigma_y f_{T,S}(\vec{q})\}}{\sum_{T,S} \text{Tr}\{f_{T,S}^{\dagger}(\vec{q}) f_{T,S}(\vec{q})\}}. \quad (4-3)$$

4.1.1 Impulse Approximation for N-Nucleus scattering

The formalism for the Impulse Approximation (IA) is based on Ref. [9]. In this approximation one nucleon in the nucleus which is denoted by "2" is involved in the reaction. Other nucleons, 3 through A+1, act as the spectators.

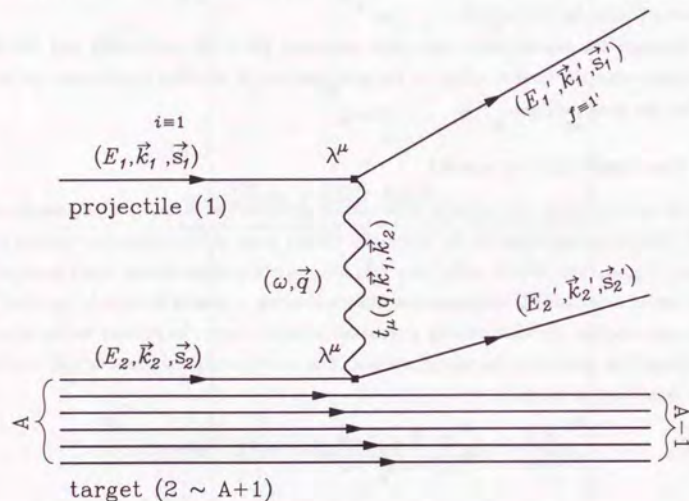


Fig. 4-1: Schematic diagram of the impulse approximation for the quasi elastic scattering.

4.1.2 Formalism for the NN amplitude

We employ the notation of Bystricky, Lehar, and Winternitz [38] for the NN amplitude which is given by

$$\tilde{t} = \frac{1}{2} \left\{ a + b + (a-b)\vec{\sigma}_1 \cdot \hat{n} \vec{\sigma}_2 \cdot \hat{n} + (c+d)\vec{\sigma}_1 \cdot \hat{m} \vec{\sigma}_2 \cdot \hat{m} + (c-d)\vec{\sigma}_1 \cdot \hat{l} \vec{\sigma}_2 \cdot \hat{l} + ie(\vec{\sigma}_1 + \vec{\sigma}_2) \cdot \hat{n} \right\}. \quad (4-4)$$

Here \tilde{t} is the non-relativistic t -matrix and a , b , c , d , and e are the NN amplitudes. The coordinate system $(\hat{l}, \hat{m}, \hat{n})$ is:

$$\hat{l} \equiv (\vec{k} + \vec{k}')/|\vec{k} + \vec{k}'|,$$

$$\hat{m} \equiv (\vec{k} - \vec{k}')/|\vec{k} - \vec{k}'|, \quad (4-5)$$

$$\hat{n} \equiv (\vec{k} \times \vec{k}')/|\vec{k} \times \vec{k}'|,$$

where $\vec{k}(\vec{k}')$ is the incident (final) momentum in the NN c.m. frame.

Using the t -matrix, the cross section and the analyzing power of the free NN scattering are given by

$$\frac{d\sigma}{d\Omega} = \text{Tr}(\tilde{t}^{\dagger} \tilde{t}) = \frac{1}{2} (|a|^2 + |b|^2 + |c|^2 + |d|^2 + |e|^2), \quad (4-6)$$

$$A_y = \frac{\text{Tr}(\tilde{t}^{\dagger} \sigma_y \tilde{t})}{\text{Tr}(\tilde{t}^{\dagger} \tilde{t})} = \frac{\text{Re}(a^* e)}{\frac{1}{2} (|a|^2 + |b|^2 + |c|^2 + |d|^2 + |e|^2)}, \quad (4-7)$$

where the vector \hat{n} coincides with the unit vector perpendicular to the scattering plane.

4.1.3 Effective nucleon number

The effective nucleon number is determined from calculations based on the Glauber model from the total NN cross section σ as

$$A_{\text{eff}} = \frac{1}{\sigma} \int_0^{\infty} d^2b \chi(b) e^{-\chi(b)},$$

$$\chi(b) = \int_{-\infty}^{\infty} dz \sigma \rho(r), \quad \vec{r} = (\vec{b}, z). \quad (4-8)$$

Here $\chi(b)$ is the total absorption along the projectile's path at impact parameter b , which is schematically shown in Fig. 4-2. $\rho(r)$ is the density distribution of nuclear matter given by Eq. 4-9. Thus A_{eff} is the probability, averaged over impact parameters, that the projectile finds a nucleon in the target to interact with and is free from absorption by the other nucleons. The expansion for Eq. 4-8 to 2nd order components is described in Appendix D.

When the experimental results are compared with the effective nucleon numbers, it is convenient to treat the effective proton number and the effective neutron number separately. In this subsection, we describe total cross sections σ_{pp} and σ_{np} for the $p+p$ and $n+p$ reactions, respectively. Correspondingly the one-nucleon densities $\tilde{\rho}_p$ and $\tilde{\rho}_n$ are defined by

$$1 \equiv \int d^3r \tilde{\rho}_{p(n)}(r),$$

$$\rho(r) = Z \tilde{\rho}_p(r) + N \tilde{\rho}_n(r). \quad (4-9)$$

Using these densities, the total absorption $\chi(b)$ in Eq. 4-8 is evaluated as

$$\chi_{pp}(b) = Z \int_{-\infty}^{\infty} dz \sigma_{pp} \tilde{\rho}_p(b),$$

$$\chi_{pn}(b) = N \int_{-\infty}^{\infty} dz \sigma_{np} \tilde{\rho}_n(b),$$

$$\chi(b) = \chi_{pp}(b) + \chi_{pn}(b). \quad (4-10)$$

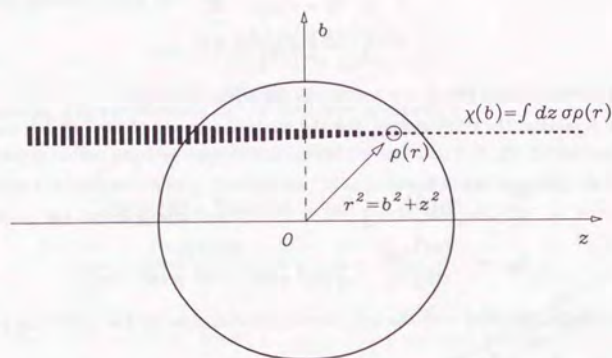


Fig. 4-2: Schematic picture for describing the Glauber theory. The total absorption $\chi(b)$ is derived by integrating the probability of a collision along the projectile's path at impact parameter b . σ is a total cross section of the projectile interacting with a nucleon in the target. $\rho(r)$ is the density of nuclear matter.

Consequently, the effective nucleon numbers are given separately as

$$\begin{aligned} N_{\text{eff}} &= \frac{1}{\sigma_{np}} \int d^2b \chi_{pn} e^{-(\chi_{pp} + \chi_{pn})}, \\ Z_{\text{eff}} &= \frac{1}{\sigma_{pp}} \int d^2b \chi_{pp} e^{-(\chi_{pp} + \chi_{pn})}, \end{aligned} \quad (4-11)$$

because protons are absorbed via common factor $e^{-(\chi_{pp} + \chi_{pn})}$ for both $p+p$ and $p+n$ reactions. The effective nucleon number A_{eff} extracted from the (p, p') reaction is a summation of above two numbers as

$$\begin{aligned} \sigma_{pN} A_{\text{eff}} &= \sigma_{pn} N_{\text{eff}} + \sigma_{pp} Z_{\text{eff}}, \\ \sigma_{pN} &= (N \sigma_{np} + Z \sigma_{pp}) / A. \end{aligned} \quad (4-12)$$

4.2 Fermi gas model

4.2.1 Formalism

Assuming that the NN amplitude in Eq. 4-1 does not depend on the invariant energy s but only depends on the momentum transfer q , we can calculate the differential cross section as

$$\frac{d^2\sigma}{d\Omega d\omega}(q, \omega) = A_{\text{eff}} \left. \frac{d\sigma}{d\Omega} \right|_{NN} R(q, \omega). \quad (4-13)$$

In this formula, the NN cross section $\left. \frac{d\sigma}{d\Omega} \right|_{NN}$ is a differential cross section of the corresponding free NN scattering process at the same reaction angle with the same bombarding energy. The response function is defined by

$$R(q, \omega) = \frac{1}{A} \sum_{i,f} \langle \phi_i | \mathcal{O}_q | \phi_f \rangle^2 \delta(E_i - E_f - \omega), \quad (4-14)$$

where A is the target nucleon number, $\phi_{i(f)}$ is the wave function in the initial(final) state of the target nucleus and \mathcal{O}_q is an operator for a transition from i to f with the momentum transfer q . In the non-interacting Fermi gas model, \mathcal{O}_q and $\phi_{i(f)}$ are equal to $e^{i\vec{q}\cdot\vec{r}}$, and $e^{i\vec{k}'\cdot\vec{r}}$, respectively. When using non-relativistic kinematics, the response function is obtained by

$$\begin{aligned} R(q, \omega) &= \frac{1}{A} \sum_{k < k_F, k_F < k'} \langle k | e^{i\vec{q}\cdot\vec{r}} | k' \rangle^2 \delta\left(\frac{k^2}{2m} - \frac{k'^2}{2m} - \omega\right) \\ &= \frac{3m}{4qk_F^3} \int_{k < k_F, k_F < k'} d^2k_{\perp}, \end{aligned} \quad (4-15)$$

where k_F is the Fermi momentum and k_{\perp} (k_z) is a perpendicular (parallel) component of the initial momentum with respect to \vec{q} . Integrating with the condition of $k_z^2 + k_{\perp}^2 < k_F^2$ and $k_F < (k_z + q)^2 + k_{\perp}^2$, the response function is evaluated as

$$R(q, \omega) = \begin{cases} \frac{3\omega_f}{\omega_W^3} \omega, & (|\omega - \omega_f| < \omega_W, |\omega + \omega_f| < \omega_W : \text{I}) \\ \frac{3}{4\omega_W} \left\{ 1 - \left(\frac{\omega - \omega_f}{\omega_W} \right)^2 \right\}, & (|\omega - \omega_f| < \omega_W, |\omega + \omega_f| > \omega_W : \text{II}) \\ 0, & (|\omega - \omega_f| > \omega_W : \text{III}) \end{cases} \quad (4-16)$$

where the energy transfer of the free NN scattering ω_f and the energy width ω_W are defined by

$$\omega_f \equiv \frac{q^2}{2m}, \quad (4-17)$$

$$\omega_W \equiv \frac{qk_F}{m}. \quad (4-18)$$

The response function is normalized by

$$\int R(q, \omega) d\omega = 1, \quad (q > 2k_F). \quad (4-19)$$

Three regions in Eq. 4-16 are illustrated by the dashed lines in every frame in Fig. 4-3 with the results of the FGM calculations using the relativistic kinematics (solid lines). The top frame shows the response for the condition of $q < k_F$, $q=1.0 \text{ fm}^{-1}$ for the nucleus with $k_F = 1.2 \text{ fm}^{-1}$. The middle (bottom) frame shows the response for the condition of $k_F < q < 2k_F$ ($2k_F < q$). The peak positions of the response function coincide exactly with the positions predicted by non-relativistic kinematics for free NN scattering at the region where q is greater than k_F . Expression I in Eq. 4-16 describes the Pauli blocking effect which changes the shape of the response function at the region where q is less than $2k_F$. The response function at the low energy side is reduced at region of $\omega < \omega_W - \omega_f = \frac{q}{2m}(2k_F - q)$. Note that the QES response is free from the Pauli blocking effect at the region where q is greater than $2k_F$ because the value of $\frac{q}{2m}(2k_F - q)$ is always negative and thus reduction does not occur at region of $\omega > 0$.

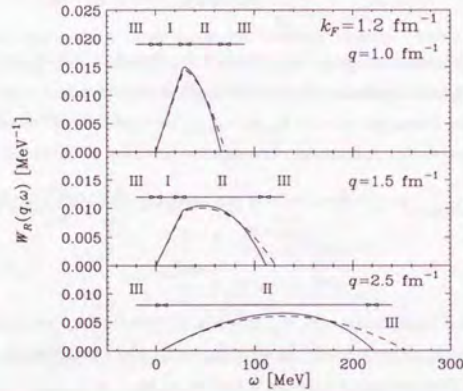


Fig. 4-3: The response functions with relativistic kinematics (solid lines) are compared to those for non-relativistic kinematics (dashed lines). The horizontal axis represents the energy transfer. The top frame shows the response for the condition of $q < k_F$, $q=1.0 \text{ fm}^{-1}$ for the nucleus with $k_F = 1.2 \text{ fm}^{-1}$. The middle (bottom) frame shows the response for the condition of $k_F < q < 2k_F$ ($2k_F < q$). In the case of $2k_F < q$, the response is free from the Pauli blocking effect. One can see the large deviation at larger ω region, which indicates the effect of relativistic kinematics. In the low q spectra the Pauli blocking effects are shown at low ω side of the peak.

Using relativistic kinematics, the expressions for the response function are not so simple as those for non-relativistic kinematics. The response function with relativistic kinematics is

expressed by

$$R(q, \omega) = \begin{cases} \frac{3\omega_f}{\omega_W^3} \omega \left(1 + \frac{12k_F^2 + \omega^2 - 3q^2}{12m^2} \right), & (E_F - \omega > E_m) & \text{I} \\ \frac{1}{2k_F^3 q} \left\{ (E_F + \frac{1}{2}\omega)(E_F + \frac{1}{2}\omega + \frac{\sqrt{3}}{2}q)(E_F + \frac{1}{2}\omega - \frac{\sqrt{3}}{2}q) \right. \\ \quad \left. - q^3 \left(\frac{m^2}{Q^2} - \frac{1}{2} \right) \sqrt{\frac{m^2}{Q^2} + \frac{1}{4}} \right\} \\ \quad \times \left\{ 1 - \frac{m^2}{k_F^2 \{ \omega \sqrt{4m^2 + Q^2} + qQ \}^2} \left(\omega - \frac{Q^2}{2m} \right)^2 \left(\omega + \frac{Q^2}{2m} \right)^2 \right\} & (E_F > E_m > E_F - \omega) & \text{II} \\ 0, & (E_m > E_F) & \text{III} \end{cases} \quad (4-20)$$

where the energy E_F and E_m are defined by

$$\begin{aligned} E_F &= \sqrt{m^2 + k_F^2}, \\ E_m &= \sqrt{m^2 + k_m^2}. \end{aligned} \quad (4-21)$$

The momentum k_m is the minimum momentum depending on (q, ω) and is given by

$$\vec{k}_m = -\vec{q} \left(1 - \frac{\omega}{q} \sqrt{1 + \frac{4m^2}{Q^2}} \right). \quad (4-22)$$

The Lorentz invariant momentum transfer Q^2 is given by

$$Q^2 = q^2 - \omega^2. \quad (4-23)$$

In the limit of

$$\begin{aligned} \omega \sqrt{1 + \frac{4m^2}{Q^2}} &\rightarrow \frac{2m\omega}{q}, \\ E_m &\rightarrow m + \frac{m}{2q}(\omega - \omega_f)^2, \end{aligned} \quad (4-24)$$

Eqs. 4-20 become equivalent to the non-relativistic formulae of Eqs. 4-16. These equations are derived in appendix A.

Due to the Fermi momentum, the peak positions of the FGM calculation with relativistic kinematics do not coincide with the positions ω_f predicted by relativistic kinematics of free NN scattering. The positions are located at higher ω than ω_f , which are shown in Fig. 4-4. The shifts of the peak positions from ω_f depend on q . The value of the shifts increases from 2 MeV to 8 MeV as q increases from 1.2 fm^{-1} to 3.0 fm^{-1} .

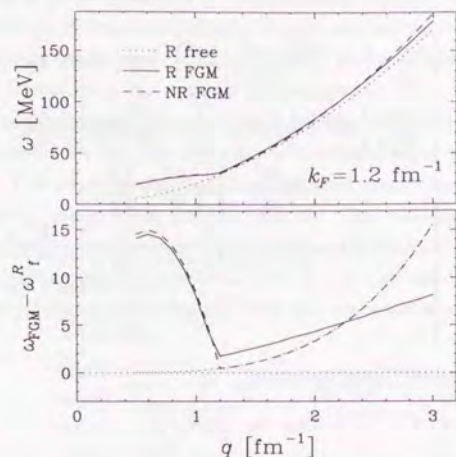


Fig. 4-4: The peak positions of the response for a Fermi gas nucleus with $k_F = 1.2 \text{ fm}^{-1}$ are shown in the top frame. The solid (dashed) line indicates the FGM response with relativistic (non-relativistic) kinematics. The dotted line indicates the position predicted by relativistic kinematics for free NN scattering. In order to emphasize the deviation from the position ω_f^R predicted by relativistic kinematics for free NN scattering, the peak shifts from ω_f^R are shown in the bottom frame. The peak positions of the FGM response with relativistic kinematics are located at 2–8 MeV higher than those for free NN scattering. The dotted line in the bottom frame indicates the position predicted by non-relativistic kinematics.

4.2.2 Comparison of the experimental data to the result of the FGM calculation

When comparing the experimental data with results of the FGM calculations using relativistic kinematics, we use the response functions which are shifted along energy transfer as

$$R(q, \omega) \rightarrow R(q, \omega - \Delta\omega),$$

in order to reproduce the peak positions.

We search for three parameters, A_{eff} , k_F , and $\Delta\omega$ by minimizing

$$F = \sum \left\{ \frac{d^2\sigma}{d\Omega d\omega}(q, \omega) - A_{\text{eff}} \frac{d\sigma}{d\Omega}(q) \right\}_{NN}^2 R(q, \omega - \Delta\omega; k_F) \Big/ \left\{ \Delta \left(\frac{d^2\sigma}{d\Omega d\omega} \right) \right\}^2. \quad (4-25)$$

Here the statistical uncertainties $\Delta(d^2\sigma/d\Omega d\omega)$ are taken into account. The summation is done over the regions around the peaks of the cross sections for all q simultaneously. For each q spectrum we select the fitting region where the cross section is larger than 0.75 times of the maximum of cross section, in a manner similar to procedure described in section 3.2.1.

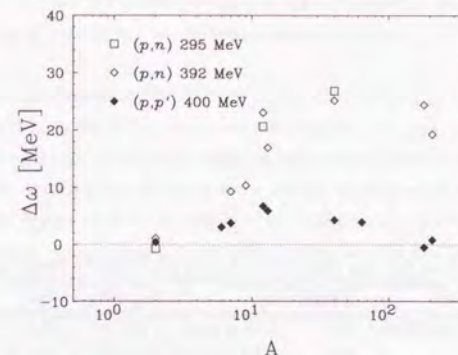


Fig. 4-5: Result of $\Delta\omega$ for the FGM calculation. Although $\Delta\omega$ is derived using all q spectra, the results are almost equivalent to the results for the peak positions at 20° shown in Fig. 3-29.

The best-fit parameters are listed in table 4-1. For all targets the results are shown in Figs. 3-1 through 3-22, respectively. Figure 4-5 shows the results of the parameter $\Delta\omega$ with respect to A . Although $\Delta\omega$ is derived using all q spectra, the results are almost equivalent to the results for the peak positions at 20° shown in Fig. 3-29.

4.2.3 Comparison of N_{eff} and A_{eff} with the Glauber model

The effective nucleon numbers evaluated from the FGM calculation can be compared with the calculations based on the Glauber model [43]. The proton distribution is derived from the charge distribution of nuclei [44, 45] by deconvoluting the charge distribution of the nucleon itself. We assume that the charge distribution of the nucleon itself is same with the matter distribution of the nucleon. In this calculation we assume that the shape of the neutron density distribution is equal to that of the proton density distribution for all nuclei as

$$\rho_n(r) = \frac{N}{Z} \rho_p(r), \quad (4-26)$$

or

$$\bar{\rho}_n(r) = \bar{\rho}_p(r). \quad (4-27)$$

We use two candidates for the total NN cross section. One is the cross section for free NN scattering, $\sigma_{np}=32.5 \text{ mb}$ and $\sigma_{pp}=26.5 \text{ mb}$ at 400 MeV. The other is the cross section in the nuclear medium, $\bar{\sigma}_{NN} \simeq 21 \text{ mb}$ at 400 MeV which is derived from the imaginary part of the optical potential [46].

Table 4-1: The k_F , A_{eff} (N_{eff}), and $\Delta\omega$ results from the Fermi gas model.

Reaction	Target	k_F	A_{eff} (N_{eff})	$\Delta\omega$
(p, p') 400 MeV	^2H	0.32 ± 0.05	1.0 ± 0.1	0.4 ± 1.1
	^6Li	0.74 ± 0.15	3.0 ± 0.3	3.0 ± 0.5
	^7Li	0.78 ± 0.13	3.4 ± 0.3	3.8 ± 1.0
	^9Be	0.83 ± 0.14	3.8 ± 0.5	3.3 ± 1.1
	^{12}C	0.97 ± 0.12	4.4 ± 0.4	6.7 ± 0.8
	^{13}C	1.03 ± 0.20	4.8 ± 0.6	5.9 ± 1.2
	$^{\text{nat}}\text{Ca}$	1.08 ± 0.10	8.8 ± 0.9	4.3 ± 1.0
	$^{\text{nat}}\text{Cu}$	1.04 ± 0.15	9.8 ± 1.4	3.9 ± 1.2
	^{181}Ta	1.19 ± 0.15	17.9 ± 2.4	-0.5 ± 1.4
	^{208}Pb	1.15 ± 0.12	20.6 ± 2.1	0.8 ± 1.2
(p, n) 392 MeV	^2H	0.35 ± 0.05	1.0 ± 0.1	1.1 ± 1.1
	^7Li	0.73 ± 0.15	2.1 ± 0.2	9.3 ± 2.0
	^9Be	0.72 ± 0.13	2.4 ± 0.2	10.3 ± 2.0
	^{12}C	1.09 ± 0.12	2.5 ± 0.3	21.0 ± 1.8
	^{13}C	1.05 ± 0.25	2.5 ± 0.8	16.9 ± 4.2
	$^{\text{nat}}\text{Ca}$	1.03 ± 0.10	4.2 ± 0.5	25.2 ± 1.8
	^{181}Ta	1.05 ± 0.15	10.6 ± 1.5	24.4 ± 2.3
	^{208}Pb	1.17 ± 0.15	11.2 ± 1.4	19.3 ± 1.7
(p, n) 295 MeV	^2H	0.31 ± 0.06	0.57 ± 0.2	-0.7 ± 1.1
	^{12}C	1.07 ± 0.16	3.3 ± 0.5	20.6 ± 1.6
	$^{\text{nat}}\text{Ca}$	1.01 ± 0.14	7.0 ± 0.9	26.8 ± 1.3

Figures 4-6 and 4-7 show the results of N_{eff} and A_{eff} , respectively. The experimental results for the (p, n) and (p, p') reactions can be approximated by $N_{\text{eff}} = N^{0.5}$ and $A_{\text{eff}} = 1.3A^{0.5}$, respectively.

The results of the calculations by the Glauber model are indicated by the regions surrounded by dotted (dashed) lines for the total cross sections of $\sigma_{np}=32.5$ mb and $\sigma_{pp}=26.5$ mb ($\sigma_{NN} = 21$ mb). The uncertainties of the calculations originate from uncertainties in the charge distribution of the nucleus. The results using the total cross section of $\bar{\sigma}_{NN} = 21$ mb overestimate both N_{eff} and A_{eff} at the region of $N < 20$ and $A < 64$, respectively. In such regions the results using the total cross sections for free NN scattering reproduce the experimental results of N_{eff} and A_{eff} . In other regions, the results by using the total cross sections for free NN scattering underestimate the effective nucleon numbers while the results using the total cross sections of $\bar{\sigma}_{NN} = 21$ mb reproduce the experimental results.

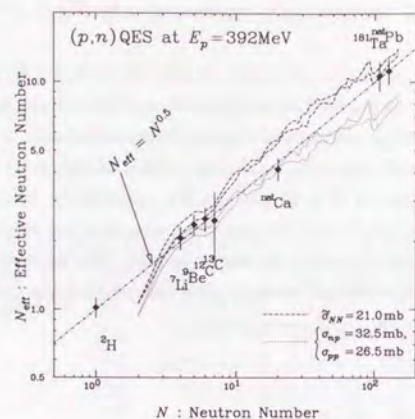


Fig. 4-6: Filled diamonds indicate the results of the QES process for the (p, n) reaction. It is consistent with the line for $N_{\text{eff}} = N^{0.5}$ which is indicated by a dot-dashed line. Dotted lines (dashed lines) indicate the results of calculations based on the Glauber model in which the total cross section is adopted as the value in the free space (modified value in the nuclear medium). The width comes from the difference of shape of the nucleus used in the calculation.

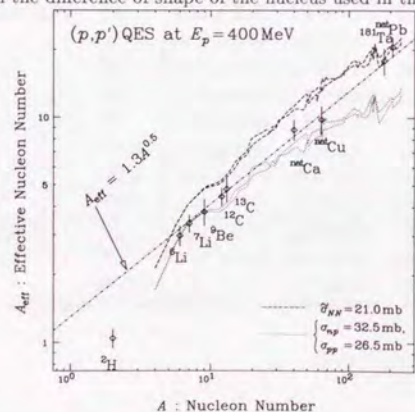


Fig. 4-7: Opened diamonds indicate the results of the QES process for the (p, p') reaction. It is consistent with the line for $A_{\text{eff}} = 1.34 A^{0.5}$ which is indicated by a dot-dashed line except for ^2H .

4.3 Kinematic effect of the Fermi motion

In this section, we discuss a kinematic effect caused by the Fermi motion in the target nucleus. Within the framework of the Fermi gas model described in the previous section, we use the NN cross sections as a constant value which is determined by the projectile energy and the scattering angle. Nucleons in the target nucleus, however, have momenta within the Fermi momentum. Therefore the bombarding energy and the reaction angle between the two nucleons should be modified according to the momentum of the nucleon in the target nucleus. When the NN cross sections is independent of ω , the QES peak shape is not modified from the FGM response. On the contrary, when the NN cross sections depend on ω through the bombarding energy and the reaction angle, the kinematic effect may modify the peak shape.

The kinematic effect should have already been taken into account in ordinary Plane Wave Impulse Approximation (PWIA). In order to emphasize the effect in this thesis, we call the model including the kinematic effect as an Extended Fermi Gas Model (EFGM).

4.3.1 Kinematics

As shown in the top frame of Fig. 4-8, we assume that the scattering occurs between the nucleons 1 and 2, where "1" is a projectile nucleon and "2" is a nucleon in the target nucleus. In the final state, the nucleons are denoted as 1' and 2', respectively. The momenta \vec{k}_1 and \vec{k}_2 are those of the projectile and target nucleon, respectively. The energy and momentum conservations are given by

$$\begin{aligned} E_1 + E_2 &= E_{1'} + E_{2'}, \\ \vec{k}_1 + \vec{k}_2 &= \vec{k}_{1'} + \vec{k}_{2'}, \end{aligned} \quad (4-28)$$

where the momentum of the nucleon 2 is distributed with $|\vec{k}_2| < k_F$ in the Fermi gas model. The notation was given in the previous subsection and was shown in Fig. 4-1. The energy transfer and the momentum transfer are given by

$$\omega = E_1 - E_{1'}, \quad (4-29)$$

$$\vec{q} = \vec{k}_1 - \vec{k}_{1'}. \quad (4-30)$$

The scattered nucleon 1' is observed at θ_{lab} , which is given by

$$\frac{\vec{k}_{1'} \cdot \vec{k}_1}{|\vec{k}_{1'}||\vec{k}_1|} = \cos \theta_{\text{lab}}. \quad (4-31)$$

From Eqs. 4-28 and 4-31, the energy and momentum of the scattered nucleons 1' and 2' ($E_{1'}, \vec{k}_{1'}, E_{2'}, \vec{k}_{2'}$) are determined.

The NN amplitude depends on an effective laboratory kinetic energy T_{eff} as well as a scattering angle θ_{cm} . T_{eff} is defined as the bombarding energy in the two-body laboratory frame (in the

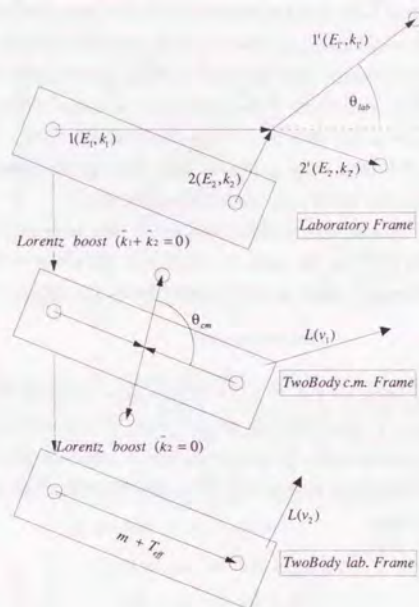


Fig. 4-8: Definitions of the frames used. For QES kinematics, not only a projectile nucleon but also a target nucleon have the kinetic energy in the initial state. Within the frame of the Fermi gas model, the QES kinematics are equivalent to those of the two nucleon scattering. From top to bottom, a laboratory frame, a two-body center of mass frame, and a two-body laboratory frame are shown. In the top frame, nucleon 1 is a projectile and nucleon 2 is a target nucleon which has a momentum $k_2 < k_F$ in the nucleus. Scattered nucleons are denoted as 1' and 2'. The nucleon 1' is detected at the laboratory angle θ_{lab} . The two-body center of mass frame is defined by a Lorentz boost $L(v_1)$ which transforms $k_1 + k_2$ to 0. The reaction angle θ_{cm} is shown. The two-body laboratory frame is defined by a Lorentz boost $L(v_2)$ which transforms k_2 to 0. An effective laboratory kinetic energy T_{eff} is defined as the bombarding energy in this frame.

bottom of the Fig. 4-8) in which the nucleon 2 has the momentum $\vec{0}$ by a Lorentz boost $L(v_2)$. The angle θ_{cm} is defined as the scattering angle in the two-body center of mass frame (in the middle of the Fig. 4-8) in which the sum $\vec{k}_1 + \vec{k}_2$ is transformed to zero by $L(v_1)$.

Figure 4-9 shows the relation between T_{eff} and θ_{cm} for the QES process in which the projectile nucleon energy is 400 MeV and the scattering angle is 20° in the laboratory frame. The most important aspect of the scattering is that the invariant energy s varies with respect to ω through its dependence on \vec{k}_2 , and it can be modified from the energy in the two-body laboratory frame. T_{eff} is given by

$$T_{eff} = \frac{s}{m} - m = \frac{E_1 E_2 - \vec{k}_1 \cdot \vec{k}_2 - m^2}{m}. \quad (4-32)$$

This relation is plotted in the right top frame of Fig. 4-9 as a function of ω . T_{eff} agrees with the true kinetic energy (shown by the vertical dotted line at 400 MeV) at the quasi elastic point $\omega = \sqrt{q^2 + m^2} - m$, which corresponds to $\vec{k}_2 = 0$ in the two-body laboratory frame. However, away from this point, it varies as much as ± 200 MeV. Such a variation will clearly have a large effect on the NN cross section.

The reaction angle θ_{cm} is given by

$$\theta_{cm} = 2 \sin^{-1} \sqrt{\frac{q^2 - \omega^2}{2mT_{eff}}}. \quad (4-33)$$

Using Eqs. 4-32 and 4-33, the relation between T_{eff} and θ_{cm} is obtained and shown in the right bottom frame of Fig. 4-9. At the quasi elastic point indicated by the cross point of the dotted lines, T_{eff} and θ_{cm} are equal to the kinetic energy and the reaction angle of the free NN scattering, respectively.

The right-bottom frame in Fig. 4-9 shows the relation between T_{eff} and θ_{cm} . In the region of higher (lower) T_{eff} than that of the quasi elastic point, the angle θ_{cm} is smaller (larger) than that of the quasi elastic point.

4.3.2 (T_{eff}, θ_{cm}) dependence of NN cross section

In this subsection, the (T_{eff}, θ_{cm}) dependence of the NN cross sections is discussed.

Figure 4-10 shows the cross sections of the NN scattering at $T_{eff} = 400$ MeV.

Top two frames show the cross sections in the center-of-mass (c. m.) frame. One is the $p + p$ scattering (left) and the other is the $n + p$ scattering (right). The cross section of the $p + p$ scattering is symmetric with respect to $\theta_{cm} = 90^\circ$ because of the identical particle scattering. On the other hand, the cross section of the $n + p$ scattering deviates from the symmetric shape as the bombarding energy becomes higher than 300 MeV shown in Fig. B-1.

For the proton induced reaction, there are the three types of the reactions in the laboratory frame, $p(p, p)p$, $n(p, p)n$, and $n(p, n)p$. Bottom three frames in Fig. 4-10 show the cross sections in the laboratory frame as a function of the laboratory scattering angle θ_{lab} . For example of the

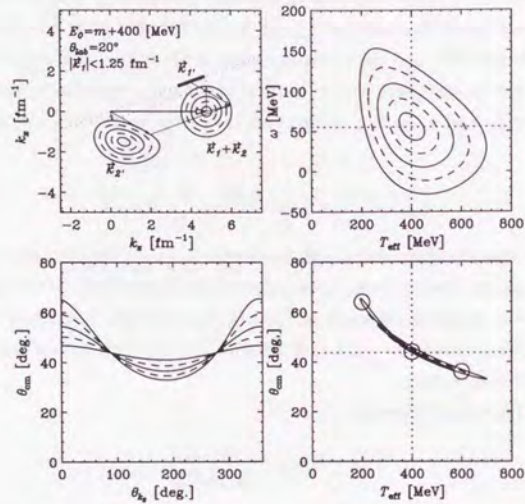


Fig. 4-9: Relation between effective bombarding energy T_{eff} and scattering angle θ_{cm} for QES at 400 MeV and 20° in the FGM calculation. k_1 is the momentum of the projectile and k_2 is the momentum of the nucleon in the target nucleus with the Fermi momentum $k_2 < k_F$. Solid and dashed lines indicate the conditions that $|k_2|$ equal to 0.25(solid), 0.5(dashed), 0.75(solid), 1.0(dashed), 1.25(solid) fm $^{-1}$.

(left top) Momentum conservation $k_1 + k_2 = k_1' + k_2'$ within the constraint that the opening angle between k_1 and k_1' is 20° .

The horizontal axis indicates a momentum component parallel to the projectile momentum k_1 while the vertical axis indicates a momentum component perpendicular to k_1 in the reaction plane. (left bottom) The reaction angle θ_{cm} depends on the Fermi motion k_2 .

(right top) T_{eff} dependence of ω . T_{eff} is determined from k_1 and k_2 while ω is determined from $|k_1|$ and $|k_1'|$.

(right bottom) The relation between T_{eff} and θ_{cm} is derived by combining the left bottom frame and the right top frame. The typical tendency of the distribution is that, relative to the $k_2 = 0$ point, the higher T_{eff} corresponds to the smaller θ_{cm} while the lower T_{eff} to the larger θ_{cm} . Open circles are exemplified to explain θ_{lab} dependence shown in Fig. 4-11. They correspond to filled circles in Fig. 4-11.

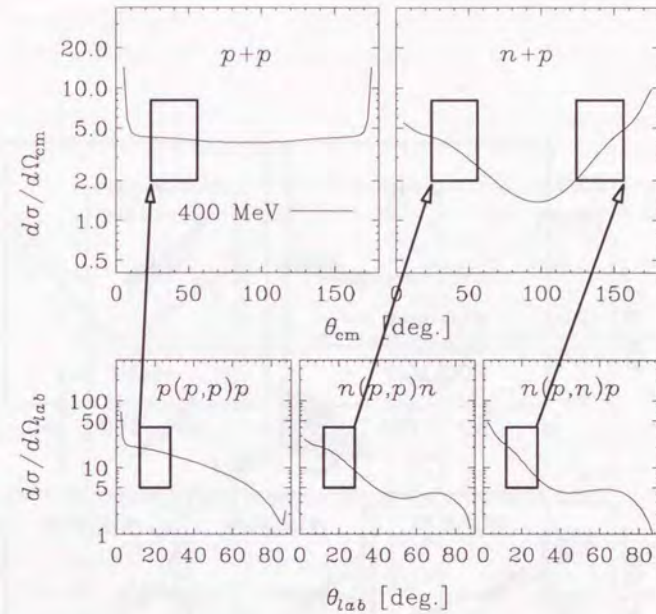


Fig. 4-10: The $p+p$ and $n+p$ cross sections in the c. m. frame at 400 MeV are shown in top two frames. From left to right in the bottom frames, the $p(p,p)p$, $n(p,p)n$, and $n(p,n)p$ reactions in the laboratory frame are shown. Correspondence between the reactions in the laboratory frame and those in the c. m. frame is indicated by arrows for the example of $\theta_{lab} \sim 20^\circ$. The $p(p,p)p$ and $n(p,p)n$ reactions at these angles correspond to the $p+p$ and $n+p$ reactions at $\theta_{cm} \sim 40^\circ$, respectively. On the other hand, the $n(p,n)p$ reaction at those angles corresponds to the $n+p$ reactions at $\theta_{cm} \sim 180^\circ - 40^\circ$.

laboratory angles around 20° shown in Fig. 4-10 by arrows, the laboratory angles of the $p(p,p)p$ and $n(p,p)n$ reactions, correspond to $\theta_{cm} \simeq 40^\circ$ of the $p+p$ and $n+p$ reactions, respectively. In the $n(p,n)p$ reaction, on the other hand, these angles correspond to $\theta_{cm} \simeq 180^\circ - 40^\circ = 140^\circ$ in the $n+p$ reaction.

Note that the QES process for the (p,p') reaction is formed by the summation of the $p(p,p)p$ and $n(p,p)n$ reactions while the QES process for the (p,n) reaction is formed by the $n(p,n)p$ reaction.

The NN cross sections for projectile energies of 200, 400, and 600 MeV are shown in Fig. 4-11. Three filled circles in each frame for the laboratory cross sections represent the QES

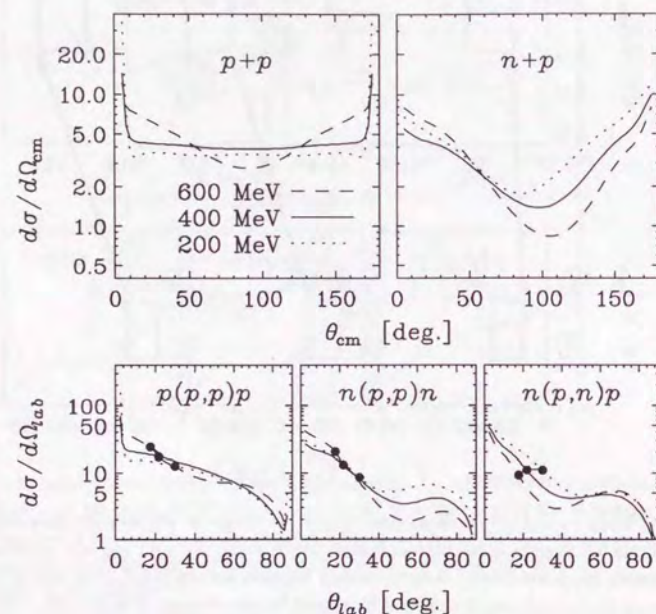


Fig. 4-11: Same figure as Fig. 4-10 but with bombarding energies of 200, 400, and 600 MeV. Above 300 MeV, the cross section of $n + p$ scattering deviates from the symmetric shape with respect to the $\theta_{cm} = 90^\circ$. These deviations make the tendencies different between the (p, p) reactions (left and middle frames in the bottom) and the (p, n) reaction (right frame in the bottom) around the QES kinematics. Three dots in each frame of laboratory cross sections represent the QES kinematics at $\theta_{lab} = 20^\circ$ which is also shown in the bottom right frame of Fig. 4-9. Relative to the $p(p, p)p$ or $n(p, p)n$ reactions, the slope of these three dots is small for the $n(p, n)p$ reaction.

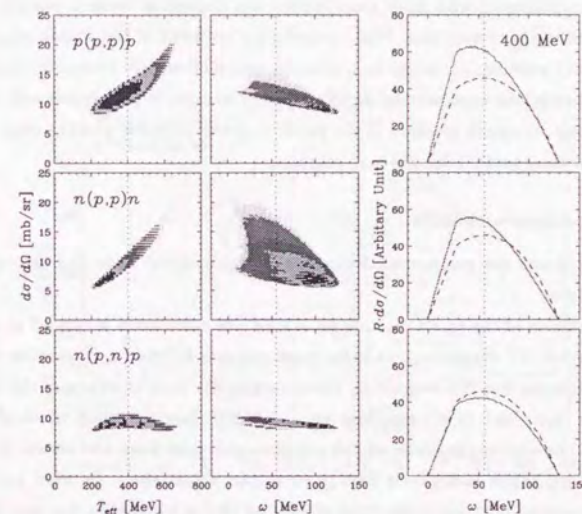


Fig. 4-12: T_{eff} and ω dependence of the NN cross sections at 400 MeV and $q = 1.65 \text{ fm}^{-1}$. The left three frames indicate the T_{eff} dependence of the cross sections. The middle three frames show the ω dependence of the cross sections. For the $p(p, p)p$ (top) and $n(p, p)n$ (middle) reactions, components with large cross sections are located at lower ω regions than ω_f . Considering products of the response and the cross section, consequently, the peak positions of the products are shifted downward of ω for these reactions shown in right-top and right-middle frames. On the other hands, the cross section for the $n(p, n)p$ reaction is almost constant (middle-bottom). As a result, the peak position of the product of the response and the cross section is nearly the same as that of the pure response (right-bottom).

kinematics at $\theta_{lab} = 20^\circ$ which are marked by the open circles in the bottom right frame of Fig. 4-9. The tendency of the three points indicates that the cross sections for larger projectile energy become larger for the $p(p,p)p$ and $n(p,p)n$ reactions while the cross section is almost constant with respect to the projectile energy for the $n(p,n)p$ reaction.

In the same manner, the T_{eff} and ω dependences of the NN cross sections can be derived, which is shown in Fig. 4-12. Focusing on the ω dependences which are shown in the middle three frames, components with large cross section are located at lower ω regions than ω_f for the $p(p,p)p$ and $n(p,p)n$ reactions. When considering products of the responses and the cross sections, the peak positions of the product, consequently, shift toward lower ω for these reactions. On the other hands, the cross section for the $n(p,n)p$ reaction is almost constant with respect to ω . As a result, the peak position of the product of the response and the cross section still remains almost same as that for the pure response.

4.3.3 Comparison with data

Figure 4-13 shows the comparison between the experimental data and the results of the EFGM calculation.

The peak position of the (p,n) reaction for the EFGM calculation is located at almost same position as for free NN scattering, while the peak position for the (p,p') reaction is located at lower ω than that for free NN scattering. Consequently the peak positions of the experimental data for both (p,n) and (p,p') reactions are located at larger ω than those of the EFGM calculations. The size of the shifts of the experimental data from the results of the EFGM calculation is larger than 15 MeV for both (p,n) and (p,p') reactions. In other words, the large peak shift is observed not only in the QES process for the (p,n) reaction but also for the (p,p') reaction.

The results of the EFGM calculation do not reproduce the peak positions both for the (p,n) and (p,p') reactions. In this model, the discrepancies of the peak position appear for both reactions. Thus, some extra mechanisms are needed which modify the peak positions to larger ω for both the (p,n) and (p,p') reactions simultaneously.

Note that the discrepancy of the peak position appears for only the (p,n) reactions in the simplified FGM calculation. It is difficult to find some extra mechanisms in which the peak positions of the (p,n) reaction are shifted upward in ω while those of the (p,p') reaction are not influenced.

In the next section, we discuss a relativistic model as one of the possible solutions.

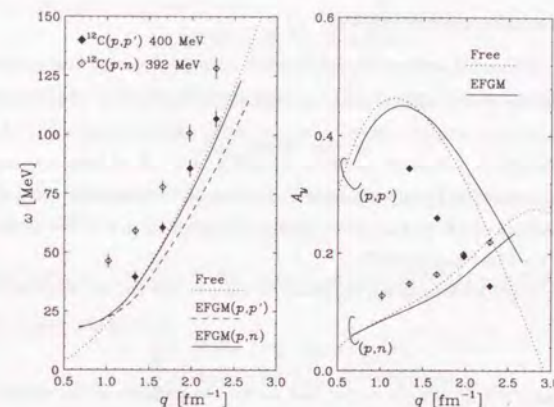


Fig. 4-13: Comparison between experimental data and the results of the EFGM calculation. As results of the EFGM calculation, the peak positions for the QES process for the (p,p') reaction shift toward lower ω from those for free NN scattering. The peak positions for the QES process for the (p,n) reaction is not so influenced by the kinematic effect. Consequently the peak positions of the experimental data for both (p,n) and (p,p') reactions are located more than 15 MeV higher than those of the EFGM calculations. Note that the analyzing powers at the peak positions are not largely influenced by the kinematic effect.

4.4 Relativistic PWIA

In this subsection we calculate the cross section and the analyzing power in a relativistic plane-wave impulse approximation (RPWIA) assuming a Fermi gas model for the target. We discuss projectile and target wave functions at an appropriate average density. Firstly, the square of the scattering matrix element is written with spin projection operators. Secondly, we take traces of the square of the matrix element to calculate the cross section and the analyzing power. Finally, a numerical integration over the Fermi-motion of the target nucleons is performed. This integration involves the experimental NN amplitudes over a range of effective kinetic energies.

4.4.1 Dirac impulse approximation

We begin by considering uniform nuclear matter with appropriate four-component spinors for the projectile and target nucleons. The spinors are solutions to a Dirac equation,

$$[\not{p} - m - U] \psi_{\vec{k},s} = 0, \quad (4-34)$$

in an optical potential $U(r, E)$ which generally depends on both position and energy. The four momentum p consists of (E, \vec{p}) and consequently \not{p} is given by $\not{p} = \gamma^0 E - \vec{\gamma} \cdot \vec{p}$. Here γ^0 and $\vec{\gamma} = (\gamma^1, \gamma^2, \gamma^3)$ are Dirac matrices[47].

Assuming the target nucleus as a spin saturated nucleus, the optical potential $U(r, E)$ can be described as[37]

$$U(r, E) = S(r, E) + \gamma^0 V(r, E), \quad (4-35)$$

where $S(r, E)$ and $V(r, E)$ are the scalar and vector components of the optical potential, respectively. The solution of Eq. 4-34 is written as an integral equation and an asymptotic limit of this wave function is given by

$$\begin{aligned} \psi_{\vec{k},s}(\vec{r}) &= e^{i\vec{k}\cdot\vec{r}} u_s(\vec{k}) + \int d^3r' \langle \vec{r} | \frac{\not{p} + m}{p^2 - m^2 + i\eta} | \vec{r}' \rangle \langle \vec{r}' | U(r, E) | \psi_{\vec{k},s} \rangle \\ &\xrightarrow{r \rightarrow \infty} e^{i\vec{k}\cdot\vec{r}} u_s(\vec{k}) + \frac{e^{ikr}}{4\pi r} \left\{ -(E\gamma^0 - k\hat{r} \cdot \vec{\gamma} + m) \int d^3r' e^{-i\vec{k}' \cdot \vec{r}'} \langle \vec{r}' | U(r, E) | \psi_{\vec{k},s} \rangle \right\}, \end{aligned} \quad (4-36)$$

where the term in curly brackets defines the scattering amplitude $F_{s's}(\vec{k}', \vec{k}; E)$ and $\vec{k}' \equiv k\hat{r}$ is the outgoing wave momentum. Employing the identity[47]

$$E\gamma^0 - \vec{k}' \cdot \vec{\gamma} + m = 2m \sum_{s'} u_{s'}(\vec{k}') \bar{u}_{s'}(\vec{k}'), \quad (4-37)$$

we can extract the scattering amplitude from Eq. 4-37 in the form:

$$F_{s's}(\vec{k}', \vec{k}; E) = -\frac{m}{2\pi} \bar{u}_{s'}(\vec{k}') \int d^3r' e^{-i\vec{k}' \cdot \vec{r}'} \langle \vec{r}' | U(r, E) | \psi_{\vec{k},s} \rangle. \quad (4-38)$$

A Dirac T matrix appropriate to elastic p -nucleus scattering is introduced by the definition:

$$U | \psi_{\vec{k},s} \rangle = T | \vec{k} \rangle u_s(\vec{k}), \quad (4-39)$$

where $|\vec{k}\rangle u_s(\vec{k})$ is the incoming plane-wave state. From Eqs. 4-39 and 4-40, the Dirac scattering amplitude is given by

$$F_{s's}(\vec{k}', \vec{k}; E) = -\frac{m}{2\pi} \bar{u}_{s'}(\vec{k}') \langle \vec{k}' | T | \vec{k} \rangle u_s(\vec{k}). \quad (4-40)$$

The central point in a single scattering approximation is that the T matrix is the expectation value of a sum of two-body NN t matrices in the nuclear ground state $|0\rangle$ as

$$\langle \vec{k}' | T | \vec{k} \rangle = \langle 0 | \sum_{i=2}^{A+1} \langle \vec{k}' | \hat{t}_i | \vec{k} \rangle | 0 \rangle. \quad (4-41)$$

Here \hat{t}_i is the t matrix for the incident proton to scatter from an i th nucleon of the target nucleus and A is the mass number of the nucleus. In the impulse approximation, the NN t -matrix elements needed in Eq. 4-42 are equal to the on-shell NN amplitude for momentum transfer $\vec{q} = \vec{k} - \vec{k}'$. The Lorentz-invariant NN amplitude between two scattering particles 1 and 2 is described as

$$\hat{t} = t_S + \gamma_\mu(1)\gamma^\mu(2)t_V + \sigma_{\mu\nu}(1)\sigma^{\mu\nu}(2)t_T + \gamma_5(1)\gamma_5(2)\gamma_\mu(1)\gamma^\mu(2)t_A + \gamma_5(1)\gamma_5(2)t_P. \quad (4-42)$$

Then the NN t matrix is given by

$$-\frac{m}{2\pi} \langle \vec{k}' | \hat{t}_i | \vec{k} \rangle = 2ik\hat{\mathcal{F}}(q^2, s) \exp(i\vec{q} \cdot \vec{r}_i), \quad (4-43)$$

where the $\hat{\mathcal{F}}$ and the components F_i are simply related respectively to \hat{t} and t_i by kinematic factors as

$$\begin{aligned} \hat{t}(q, s) &= \frac{4\pi k}{m} \hat{\mathcal{F}}(q, s), \\ t_i(q, s) &= \frac{4\pi k}{m} F_i(q, s). \end{aligned} \quad (4-44)$$

Combining Eqs. 4-41, 4-42, and 4-44, the following relation for the single-scattering amplitude for the proton-nucleus scattering is deduced:

$$F_{s's}(\vec{k}', \vec{k}; E) = 2ik\bar{u}_{s'}(\vec{k}') \sum_{i=2}^{A+1} \langle 0 | \mathcal{F}(q) \exp(i\vec{q} \cdot \vec{r}_i) | 0 \rangle u_s(\vec{k}). \quad (4-45)$$

Notice that for a spin-saturated nucleus, this matrix element involves a trace over struck-nucleon spins which eliminates all but the scalar (F_S) and time component of vector ($\gamma^0(1)F_V$) terms from the Dirac scattering amplitude of Eq. 4-43. Thus, Eq. 4-46 is simplified to

$$F_{s's}(\vec{k}', \vec{k}; E) = 2ik\bar{u}_{s'}(\vec{k}') \left[F_S(q) \rho_S(q) + \gamma^0(1)F_V(q) \rho_V(q) \right] u_s(\vec{k}), \quad (4-46)$$

where the scalar and vector form factors of the nucleus are defined by

$$\rho_S(q) = \langle 0 | \sum_{i=2}^{A+1} \exp(i\vec{q} \cdot \vec{r}_i) | 0 \rangle, \quad (4-48)$$

$$\rho_V(q) = \langle 0 | \sum_{i=2}^{A+1} \gamma^0(i) \exp(i\vec{q} \cdot \vec{r}_i) | 0 \rangle. \quad (4-49)$$

Equation 4-47 defines the Dirac impulse approximation. It consists of a scalar and a vector term which are fully determined by the NN amplitudes and the nuclear density. This procedure neglects nuclear-medium modification of the NN interaction, off-shell effects and intrinsic corrections of order A^{-1} to the optical potential. Implicitly we assume the operator form of the NN amplitudes in Dirac representation to obtain

$$\langle \vec{k}' | U | \vec{k} \rangle \simeq \langle \vec{k}' | T | \vec{k} \rangle = -\frac{4i\pi k}{m} [F_S(q)\rho_S(q) + \gamma^0(1)F_V(q)\rho_V(q)]. \quad (4-50)$$

The coordinate-space optical potential is found by the Fourier transformation as

$$\begin{aligned} U(r, E) &= S(r, E) + \gamma^0(1)V(r, E) \\ &= -\frac{4i\pi k}{m} [F_S\rho_S(r) + \gamma^0(1)F_V\rho_V(r)], \end{aligned} \quad (4-51)$$

We assume the components S and V are approximately proportional to the baryon density:

$$S(r, E) \simeq S_0(E) \frac{\rho(r)}{\rho_0}, \quad V(r, E) \simeq V_0(E) \frac{\rho(r)}{\rho_0}. \quad (4-52)$$

Here $S_0(E)$ and $V_0(E)$ are the depth of the potential at the origin where the density is ρ_0 .

4.4.2 Effective mass

In the work of Ref. [9] relativistic effects were examined using the projectile effective mass m_1^* and the effective mass m_2^* for the nucleon in the nucleus, separately. m_1^* is slightly larger than m_2^* due to a small energy dependence of $S(r, E)$. In this work, however, we ignore the difference for simplicity.

We simply evaluate Eq. 4-52 at an average density $\bar{\rho}$ which is calculated by the Glauber approximation:

$$\begin{aligned} \bar{\rho} &= \frac{\int d^2b \chi(b) \int dz \rho(r)^2}{\int d^2b \chi(b) \int dz \rho(r)}, \\ \bar{k}_F &= \left(\frac{3}{2} \pi^2 \bar{\rho} \right)^{\frac{1}{3}}, \end{aligned} \quad (4-53)$$

where the absorption $\chi(b)$ is given by Eq. 4-8. Using Eq. 4-52 we define an average scalar field $\bar{S}(E)$ as

$$\bar{S}(E) = S_0(E) \frac{\bar{\rho}}{\rho_0}. \quad (4-54)$$

Table 4-2: Average masses and Fermi momenta

Target	T_{lab} [MeV]	m^*/m	k_F fm ⁻¹
¹² C	400	0.85	0.98
⁴⁰ Ca	400	0.82	1.05
²⁰⁸ Pb	400	0.84	0.98

The four-component spinor for the nucleon of momentum \vec{k} in these potentials is

$$u(k, s) = \left(\frac{E^* + m^*}{2m^*} \right)^{\frac{1}{2}} \begin{bmatrix} \vec{1} \\ \frac{\vec{\sigma} \cdot \vec{k}}{E^* + m^*} \end{bmatrix} \chi_s. \quad (4-55)$$

Here χ is a Pauli spinor. The effective mass m^* is given by

$$m^* = m + \bar{S}(E). \quad (4-56)$$

As a result, $E^* = \sqrt{k^2 + m^{*2}}$ is given. The ratio of lower components to upper ones for given \vec{k} is determined by m^* . As m^* decreases, the lower components are enhanced. Typical values of m^* are 0.82 – 0.85 m , which are listed in table 4-2. Note that the vector component vanishes when a trace is taken over the spinor.

Between the two representations of the NN amplitude, the non-relativistic one of Eq. 4-4 and the relativistic one 4-43, the relation

$$\langle u'_1 u'_2 | \vec{l} | u_1 u_2 \rangle = \langle \chi'_1 \chi'_2 | \vec{l} | \chi_1 \chi_2 \rangle. \quad (4-57)$$

is required in the free space where m^* equals to m . The matrix which transforms between different representations is shown in detail in appendix C. In the relativistic model the parameters of t_S , t_V , t_T , t_A and t_P are not modified. Instead, the NN amplitude is modified through the modification of spinors which depend on the effective mass m^* .

4.4.3 Pseudovector model

Considering the degrees of freedom of the NN amplitude, five parameters are required in the free space. In the nuclear medium, another parameter depending on $(1 - \frac{m^*}{m})$ might be added to the five parameters of the NN amplitude in the free space. Therefore we emphasize that the representation in Eq. 4-43 is not unique in the nuclear medium where m^* is not always equal to m . In this thesis, the model using the pseudovector parameterization for the πN coupling is considered as another representation for Eq. 4-43. In the pseudovector model, the pseudoscalar coupling γ_5 is replaced with

$$\lambda_{pv} = \frac{\not{\epsilon} \gamma_5}{2m}, \quad (4-58)$$

where q is the four momentum transfer (ω, \vec{q}). According to the effective mass, Eq. 4-58 gives the modification by $\frac{m^*}{m}$ for the πN coupling in the nuclear medium as

$$\bar{u}(k'_1) \frac{\not{q} \gamma_5}{2m} u(k_1) = \frac{m^*}{m} \bar{u}(k'_1) \gamma_5 u(k_1). \quad (4-59)$$

In the free spinors of mass m , the πN coupling is confirmed to be equal with each other.

For the pseudovector model we simply multiply t_P by

$$t_{PV} = \left(\frac{m^*}{m} \right)^2 t_P, \quad (4-60)$$

to get the pseudovector amplitude.

4.4.4 Cross section and analyzing power

By summing over the unobserved spin of the target nucleon with appropriate kinematic factors, the cross section with one nucleon in the nucleus is calculated from Eq. 4-42. The cross section is averaged over a Fermi gas momentum distribution for k_2 up to k_F and given by

$$\begin{aligned} \frac{d^2\sigma}{d\Omega dE_1} &= \int_{k_2 < k_F} d^3k_2 \theta \sum_{s'_2, s'_1, s_2, s_1} |\langle u'_1(k'_1, s'_1) u'_2(k'_2, s'_2) | \hat{t} | u_1(k_1, s_1) u_2(k_2, s_2) \rangle|^2, \\ \theta &= \frac{3}{4\pi k_F^3} \frac{k'_1 E'_1}{k_1 E_1} m^{*2} \frac{\delta(E_1 + E_2 - E'_1 - E'_2)}{E_2 E_2} \frac{1}{(2\pi)^2}. \end{aligned} \quad (4-61)$$

The analyzing power is given by

$$A_y = \frac{\int d^3k_2 \theta \sum_{s'_2, s_2, s_1} (|\langle u'_1(k'_1, s'_1 = \hat{n}) u'_2(k'_2) | \hat{t} | u_1 u_2 \rangle|^2 - |\langle u'_1(k'_1, s'_1 = -\hat{n}) u'_2(k'_2) | \hat{t} | u_1 u_2 \rangle|^2)}{d^2\sigma/d\Omega dE_1}. \quad (4-62)$$

The results of the cross sections and the analyzing powers calculated with the model are shown in Figs. 3-3 through 3-22 by the dot-dashed lines. The peak positions are derived from the results of the cross section. In left frames of Figs. 3-25 through 3-27, the peak positions for the (p, n) ((p, p')) reaction are shown by the solid (dashed) lines. In the right frames of these figures the analyzing powers at the peak positions are shown by the dashed lines for both (p, n) and (p, p') reactions. The amplitudes of the cross sections are scaled by appropriate A_{eff} and N_{eff} for the (p, p') and (p, n) reactions, respectively.

4.4.5 Modification by the effective mass and the pseudovector model

peak position

Peak positions of the cross sections are modified depending approximately on $\left(\frac{m^*}{m}\right)^{-1}$ irrespective of the (p, n) or (p, p') reaction. Consequently, the effective mass shifts the peak positions towards higher ω . On the other hand, the kinematic correction of the NN amplitude shifts the peak positions towards lower ω . We take these two effects into account for the RPWIA calculation simultaneously. The relative position between the (p, n) reaction and the (p, p') reaction

is reproduced by the combination of the two effects. The peak positions themselves, however, are not sufficiently reproduced. When we employ $m^* = 0.7m$ instead of $0.85m$, it is found that the peak positions are well reproduced at $q > 1.5 \text{ fm}^{-1}$, which is shown in Fig. 4-14. We need more complicated models which are not discussed in this thesis for explaining the region $q < 1.5 \text{ fm}^{-1}$.

analyzing power

Analyzing powers depend on the effective mass as

$$A_y = \frac{2 \sin \theta \left(\frac{k}{m^*}\right)^2 \text{Im}(t_S^* t_V)}{\cos^2 \theta \left(\frac{k}{m^*}\right)^4 |t_S - 3t_V|^2} \approx \frac{\sin \theta}{\cos^2 \theta} \left(\frac{m^*}{k}\right)^2, \quad (4-63)$$

where only the scalar and vector terms are taken into account[48]. We can ignore the pseudoscalar t_P term because the a and e terms which appear in the numerator of Eq. 4-6 do not depend on t_P . Note that only c and d terms depend on the t_P term, as shown in Eq. C-4. Thus, the analyzing powers are reduced by $\left(\frac{m^*}{m}\right)^2$ for both the (p, p') and (p, n) reactions.

Next, the dependence of the πN coupling is considered. The effect of the pseudovector coupling (PV) instead of the pseudoscalar coupling (PS) appears on only c and d terms by

$$\left(\frac{c}{d}\right)_{\text{PV}} = \left(\frac{m^*}{m}\right)^2 \left(\frac{c}{d}\right)_{\text{PS}}. \quad (4-64)$$

Other terms, a , b and e are not influenced by the selection of the πN coupling. As a result, only the denominator which represents the cross section in Eq. 4-6 is influenced. Therefore, the analyzing powers are modified through the modification of the cross sections. For the (p, p') reactions the analyzing powers are not strongly modified by the replacement to the PV coupling. It is because c and d are not the dominant terms in the region of interest about the reaction angles, which is shown in Fig. 4-15. For the (p, n) reaction, on the contrary, the cross sections are dominated by the squares of the amplitudes, $|c|^2$ and $|d|^2$, and therefore reduced by $\left(\frac{m^*}{m}\right)^4$ when only these two terms are only taken into account. Even considering together with the modification by the m^* effect of $\left(\frac{m^*}{m}\right)^2$, the analyzing powers are enhanced as a total.

Thus, the experimental results of the analyzing powers, the reduction for the (p, p') reactions and the enhancement for the (p, n) reactions, are reproduced simultaneously by using the pseudovector representation within the RPWIA model.

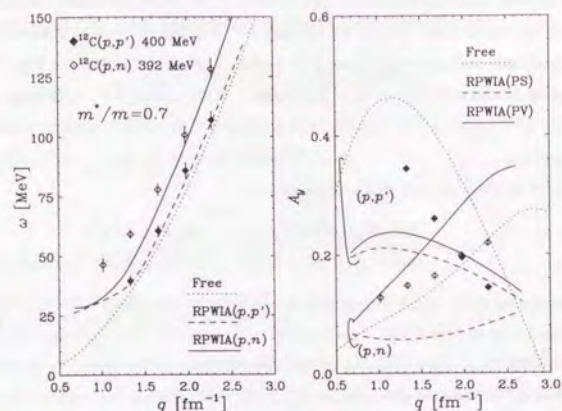


Fig. 4-14: The results of the RPWIA calculation using the effective mass $m^*/m=0.7$. In the region of $q > 1.5 \text{ fm}^{-1}$, the peak positions are well reproduced for the (p,n) and (p,p') reaction simultaneously. For the analyzing powers, modifications by the effective mass are too large to explain the experimental data.

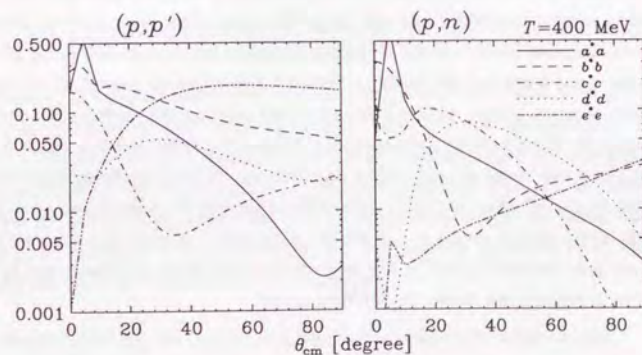


Fig. 4-15: The NN amplitudes corresponding to the (p,n) and (p,p') reactions. In the left and right frames, the squares of the individual NN amplitudes for the (p,p') and (p,n) reactions are shown, respectively. In the regions of $\theta_{cm} \simeq 40^\circ$, which corresponds to the regions of $\theta_{lab} \simeq 20^\circ$, the dominant terms for the (p,p') reaction are a , b , and e terms while those for the (p,n) reaction are c and d terms.

5 Summary

In this work we have aimed at revealing the systematic features, q dependence and A dependence, of the proton induced quasi elastic scattering by measuring the cross sections and the analyzing powers.

We measured the cross section and the analyzing power of the QES for the (p,n) reaction at 392(295) MeV and for the (p,p') reaction at 400 MeV. The spectra were obtained for the several targets from ^2H through ^{nat}Pb at laboratory angles 12° to 28° (15° to 35° at 295 MeV) which correspond to the momentum transfer q from 1.0 fm^{-1} through 2.4 fm^{-1} .

The results can be summarized as:

- i) We have compared the peak positions of the QES process with the positions $\omega_f(q)$ predicted by kinematics of free NN scattering. The positions of the QES peaks for the (p,n) reactions for targets heavier than ^{12}C are located at ω about 25 MeV larger than ω_f . The size of the peak shifts from ω_f is almost irrespective of momentum transfer ($q = 1.0 - 2.4 \text{ fm}^{-1}$) and bombarding energies (295 MeV and 392 MeV).
- ii) The QES peaks for the (p,p') reactions for ^{12}C and ^{nat}Ca targets are also located at ω about 5 MeV larger than ω_f . The size of the peak shifts from ω_f slightly decreases according to the increase of mass number A .
- iii) The analyzing powers at the QES peak for the (p,p') reactions with targets beyond $A=12$ are reduced to 60 % from those for free NN scattering.
- iv) The analyzing powers at the QES peak for the (p,n) reactions are slightly larger than those of free NN scattering for all targets studied.

Using the FGM, EFGM and RPWIA in which the target nucleus is regarded as the Fermi gas, we show how the peak positions and the analyzing powers are modified.

Some of the important results as for the peak positions are:

- v) With the non-relativistic kinematics, the peak position from the simplified model (denoted as FGM) exactly equals to the position predicted by the non-relativistic kinematics of free NN scattering. When we apply the relativistic kinematics for the FGM, the peak position is shifted to higher ω by the effect of the Fermi momentum. For the target with Fermi momentum $k_F=1.2 \text{ fm}^{-1}$, the size of the shift increases gradually from 2 MeV for $q=1.2 \text{ fm}^{-1}$ to 8 MeV for $q=3.0 \text{ fm}^{-1}$. The size is not sufficiently large to explain the peak positions for the (p,n) reactions. Thus, the FGM calculation is unable to reproduce the peak positions for the (p,n) and (p,p') reactions simultaneously. Furthermore, this model implies no mechanisms which make difference of the peak positions between the (p,n) reaction and the (p,p') reaction. Thus, the model cannot reproduce (1) the experimental

results of the QES peak positions both for the (p, n) and (p, p') reactions and (2) relative positions between the QES peaks for the (p, n) reactions and those for the (p, p') reactions.

- vi) The momentum of nucleons in the nucleus, Fermi motion, is taken into account for the NN amplitude. We have denoted this model as EFGM. The peak positions calculated by this model are shifted to lower ω because the NN amplitudes at the lower ω regions have relatively larger values than those at high ω regions. The size of the peak shifts is different between the (p, n) reaction and the (p, p') reaction. The difference originates from the asymmetrical shape of differential cross sections for the $n + p$ reactions. Note that the asymmetrical shape becomes obvious when the projectile proton energy is larger than 300 MeV. Thus, although the experimental results of the peak positions cannot be reproduced, the difference between the peak positions for the (p, n) reactions and for the (p, p') reactions can be reproduced. It is also mentioned that the peak shifts towards the higher ω may be able to be explained within some concurrent ways for both the (p, n) and (p, p') reactions.

- vii) As one of the solutions to explain the peak shifts simultaneously, we have employed the relativistic model in the PWIA calculation. In this model the mass of nucleon in the nucleus is modified to the effective mass m^* which depends on the nuclear density. The peak position is shifted to larger ω as the effective mass becomes smaller. Taking the effective mass of $0.7m$, the peak position can be reproduced at $q > 1.5 \text{ fm}^{-1}$.

Considering the experimental results of the peak positions from this point of view, the positions are governed by both the m^* effect and the kinematic effect. For the (p, p') reactions the two effects compensate each other, while, for the (p, n) reactions, the kinematic effect makes smaller shifts than those for the (p, p') reactions. As results, the peak shifts for the (p, n) reactions from ω_f are larger than those for the (p, p') reactions.

The results for the analyzing powers are:

- viii) Because the analyzing powers for FGM and EFGM do not deviate noticeably from those of free NN scattering, we focus only on the results of the RPWIA calculation.

The analyzing powers for the (p, p') and (p, n) reactions around the QES peaks are reduced in the same manner by the effective mass effect. The analyzing powers for the (p, n) reactions are also sensitive to the parameterization of the πN coupling, while those for the (p, p') reactions are insensitive. Using the pseudovector coupling instead of the pseudoscalar coupling, the analyzing powers for the (p, n) reactions are enhanced. The enhancement by the pseudovector coupling model compensates the reduction by the effective mass. Thus, the reduction in the (p, p') QES and the slight enhancement in the (p, n) QES are reproduced simultaneously by incorporating the pseudovector parameterization into the RPWIA model.

We have shown one more feature for the QES process about the effective nucleon numbers, N_{eff} and A_{eff} as:

- ix) From the (p, n) reactions at 392 MeV, N_{eff} can be represented by $N_{\text{eff}} = N^{0.5}$ for a wide mass range from ^2H to ^{208}Pb . From the (p, p') reactions at 400 MeV, A_{eff} can be represented by $A_{\text{eff}} = 1.3 \times A^{0.5}$ for from ^6Li to ^{208}Pb . These relations are well reproduced by calculations based on Glauber theory.

6 Conclusion

In this thesis experimental investigations on quasi elastic scattering have been reported by measuring the cross sections and the analyzing powers for the (p, n) and (p, p') reactions. We have focused on the two observables, the position of the QES peak and the analyzing power around the peak position.

We have derived the systematic deviations of the observables from those for free NN scattering, the shifts of the peak positions for both the (p, n) and (p, p') reactions and reduction and enhancement of the analyzing powers for the (p, p') and (p, n) reaction, respectively.

We have discussed how simple models are able to give satisfactory explanations about these deviations simultaneously. We have compared the peak positions of the experimental results with the results by the calculations of the Fermi gas model. As a result of the comparison, we have emphasized the necessities of both the kinematic correction of the NN amplitude and the mechanism which shifts the peak positions towards higher ω , such as the effect by the effective mass, within the framework of the Fermi gas model. In the RPWIA model the mass of the nucleon in the nuclear medium is taken into account as the effective mass. Therefore, the feature of the peak shift is qualitatively explained within the model. From the comparison of analyzing powers between the experimental results and the results of the calculation of the RPWIA model, we have concluded that the pseudovector representation should be incorporated with the effective mass. As a result, it is found that the peak positions and the analyzing powers for both the (p, n) and (p, p') reactions are well reproduced simultaneously at regions of $q > 1.5 \text{ fm}^{-1}$ by the RPWIA model.

References

- [1] W. N. Alberico, M. Ericson and A. Molinari, Nucl. Phys. **A379**, 429 (1982).
- [2] M. Ichimura, K. Kawahigashi, T. S. Jorgensen, and C. Gaarde, Phys. Rev. **C39**, 1446 (1989).
- [3] R. E. Chrien, T. J. Krieger, R. J. Sutter, M. May, H. Palevsky, R. L. Stearns, T. Kozlowski, and T. Bauer, Phys. Rev. **C21**, 1014 (1980). R. D. Smith, "Spin Observables of Nuclear Probes", edited by C. J. Horowitz, C. D. Goodman, and G. E. Walker, Plenum, New York, 1988, p.15.
- [4] T. A. Carey, K. W. Jones, J. B. McClelland, J. M. Moss, L. B. Rees, N. Tanaka, and A. D. Bacher, Phys. Rev. Lett. **53**, 144 (1984).
- [5] L. B. Rees, J. M. Moss, T. A. Carey, K. W. Jones, J. B. McClelland, N. Tanaka, A. D. Bacher, and H. Esbensen Phys. Rev. **C34**, 627 (1986).
- [6] O. Häusser, R. Abegg, R. G. Jeppesen, R. Sawafu, A. Celler, A. Green, R. L. Helmer, R. Henderson, K. Hicks, K. P. Jackson, J. Mildenerger, C. A. Miller, M. C. Vetterli, S. Yen, M. J. Iqbal, and R. D. Smith, Phys. Rev. Lett. **61**, 822 (1988).
- [7] C. Chan, T. E. Drake, R. Abegg, D. Frekers, O. Häusser, K. Hicks, D. A. Hutcheon, L. Lee, C. A. Miller, R. Schubank, and S. Yen, Nucl. Phys. **A510**, 713 (1990).
- [8] R. D. Smith and S. J. Wallace, Phys. Rev. **C32**, 1654 (1985).
- [9] C. J. Horowitz and D. P. Murdock, Phys. Rev. **C 37**, 2032 (1988).
- [10] C. J. Horowitz and M. J. Iqbal, Phys. Rev. **C 33**, 2059 (1986).
- [11] D. L. Prout, C. Zafiratos, T. N. Taddeucci, J. Ullmann, R. C. Byrd, T. A. Carey, P. Lisowski, J. B. McClelland, L. J. Rybarczyk, W. Sailor, W. Amian, M. Braunstein, D. Lind, D. J. Mercer, D. Cooper, S. DeLucia, B. Luther, D. G. Marchlenski, E. Sugarbaker, J. Rapaport, B. K. Park, E. Gulmez, C. A. Whitten, Jr., C. D. Goodman, W. Huang, D. Ciskowski, and W. P. Alford, Phys. Rev. **C52**, 228 (1995).
- [12] T. N. Taddeucci, R. C. Byrd, T. A. Carey, D. E. Ciskowski, C. D. Goodman, E. Gulmez, W. Huang, D. Marchlenski, J. B. McClelland, D. Prout, J. Rapaport, L. J. Rybarczyk, W. C. Sailor, and E. Sugarbaker, Nucl. Phys. **A527**, 393c (1991).
- [13] X. Y. Chen, T. N. Taddeucci, J. B. McClelland, T. A. Carey, R. C. Byrd, L. J. Rybarczyk, W. C. Sailor, D. J. Mercer, D. L. Prout, S. DeLucia, B. Luther, D. G. Marchlenski, E. Sugarbaker, J. Rapaport, E. Gulmez, C. A. Whitten, Jr., C. D. Goodman, W. Huang, Y. Wang, and W. P. Alford, Phys. Rev. **C47**, 2159 (1993).

- [14] T. N. Taddeucci, in *Polarization Phenomena in Nuclear Physics*, edited by E. J. Stephenson, and S. E. Vigdor (AIP Conference Proceedings 339, New York, 1995) p. 371.
- [15] L. Wang, X. Yang, J. Rapaport, C. D. Goodman, C. C. Foster, Y. Wang, J. Piekarewicz, E. Sugarbaker, D. Marchlenski, S. de Lucia, B. Luther, L. Rybarczyk, T. N. Taddeucci, and B. K. Park, Phys. Rev. **C50**, 2438 (1994).
- [16] K. H. Hicks, W. P. Alford, A. Celler, R. S. Henderson, K. P. Jackson, C. A. Miller, M. C. Vetterli, S. Yen, F. Brieva, C. J. Horowitz, and J. Piekarewicz, Phys. Rev. **C47**, 260 (1993).
- [17] T. Wakasa, Ph.D Thesis, University of Tokyo, 1997.
- [18] P. Barreau, M. Bernheim, J. Duclos, J. M. Finn, Z. Meziani, J. Morgenstern, J. Mougey, D. Royer, B. Saghai, D. Tarnowski, S. Turck-Chieze, M. Brussel, G. P. Capitani, E. De Sanctis, S. Frullani, F. Garibaldi, D. B. Isabelle, E. Jans, I. Sick, and P. D. Zimmerman, Nucl. Phys. **A402**, 515 (1983).
- [19] I. Bergqvist, A. Brockstedt, L. Carlen, L. P. Ekstrom, B. Jakobsson, C. Ellegaard, C. Gaarde, J. S. Larsen, C. D. Goodman, M. Bedjidian, D. Contardo, J. Y. Grossiord, A. Guichard, R. Haroutunian, J. R. Pizzi, D. Bachelier, J. L. Boyard, T. Hennino, J. C. Jourdain, M. Roy-Stephan, M. Boivin, and P. Radvanyi, Nucl. Phys. **A469**, 648 (1987).
- [20] D. V. Bugg and C. Wilkin, Nucl. Phys. **A467**, 565 (1987).
- [21] C. Ellegaard, C. Gaarde, T. S. Jorgensen, J. S. Larsen, C. D. Goodman, I. Bergqvist, A. Brockstedt, P. Ekstrom, M. Bedjidian, D. Contardo, J. Y. Grossiord, A. Guichard, D. Bachelier, J. L. Boyard, T. Hennino, J. C. Jourdain, M. Roy-Stephan, P. Radvanyi, and J. Tinsley, Phys. Rev. Lett. **59**, 974 (1987).
- [22] R. J. Peterson, S. Hoibraten, J. Ouyang, M. R. Braunstein, X. Y. Chen, M. D. Kohler, B. J. Kriss, D. J. Mercer, D. S. Oakley, D. L. Prout, and W. Fong, Phys. Lett. **B 297**, 238 (1992).
- [23] T. Sams, in *Spin and Isospin in Nuclear Interactions*, edited by S. W. Wissink, C. D. Goodman, and G. E. Walker (Plenum, New York, 1991) p. 497.
- [24] T. Rapaport, in *Spin and Isospin in Nuclear Interactions*, edited by S. W. Wissink, C. D. Goodman, and G. E. Walker (Plenum, New York, 1991) p. 433.
- [25] I. Miura, T. Yamazaki, A. Shimizu, K. Hosono, T. Itahashi, T. Saito, A. Ando, H. Ogata, I. Katayama, M. Tosaki, M. Kondo, and H. Ikegami, RCNP Annual Report (1987) p.125

- [26] M. W. McNaughton and E. P. Chamberlin, *Phys. Rev.* **C24**, 1778 (1981).
- [27] M. Ieiri, H. Sakaguchi, M. Nakamura, H. Sakamoto, H. Ogawa, M. Yosoi, T. Ichihara, N. Isshiki, Y. Takeuchi, H. Togawa, T. Tsutsumi, S. Hirata, T. Nakano, S. Kobayashi, T. Noro, and H. Ikegami, *Nucl. Instrum. Methods Phys. Res.* **A257**, 253 (1987).
- [28] R. A. Arndt and L. D. Roper, Scattering Analyses Interactive Dial-in(SAID) program, Virginia Polytechnic Institute and State University (unpublished).
- [29] T. N. Taddeucci, W. P. Alford, M. Barlett, R. C. Byrd, T. A. Carey, D. E. Ciskowski, C. C. Foster, C. Gaarde, C. D. Goodman, C. A. Goulding, E. Gulmez, W. Huang, D. J. Horen, J. Larsen, D. Marchlinski, J. B. McClelland, D. Prout, J. Rapaport, L. J. Rybarczyk, W. C. Sailor, E. Sugarbaker, C. A. Whitten Jr, *Phys. Rev* **C41**, 2548 (1990).
- [30] H. Sakai, H. Okamura, H. Otsu, T. Wakasa, S. Ishida, N. Sakamoto, T. Uesaka, Y. Satou, S. Fujita, K. Hatanaka, *Nucl. Instrum. Methods*, **A369**, 120 (1996).
- [31] K. A. Cecil, B. D. Anderson, and R. Madey, *Nucl. Instrum. Methods*, **161**, 439 (1979).
- [32] N. Matsuoka, T. Noro, K. Sagara, S. Morinobu, A. Okihana, and K. Hatanaka, RCNP Annual Report, p186, (1991)
- [33] A. Okihana, N. Matsuoka, T. Noro, and M. Yoshimura, RCNP Annual Report, p150, (1994)
- [34] A. Okihana, N. Matsuoka, T. Noro, K. Sagara, H. Akiyoshi, H. Utsunomiya, and M. Yoshimura, RCNP Annual Report, p178, (1992), A. Okihana, T. Noro, private communication.
- [35] L. Rikus, K. Nakano and H. V. Von Geramb, *Nucl. Phys.* **A414**, 413 (1984).
- [36] T. Uchida, N. Ohtsuka, Y. Nara and A. Ohnishi, in preparation
- [37] J. A. McNeil, L. Ray, and S. J. Wallace, *Phys Rev. C* **27**, 2123 (1983).
- [38] J. Bystricky, F. Lehar, and P. Winternitz, *J. Phys. (Paris)* **39**, 1 (1978)/.
- [39] A. N. James, W. J. McDonald, J. M. Cameron, C. A. Miller, D. A. Hutcheon, P. Kitching, G. C. Neilson, G. M. Stinson, and E. D. Earle, *Nucl. Phys.* **A324**, 253 (1979).
- [40] J. D. Walecka, *Ann. Phys. (N. Y.)* **83**, 491 (1974).
- [41] E. J. Moniz, I. Sick, R. R. Whitney, J. R. Ficenec, R. D. Kephart, and W. P. Trower, *Phys. Rev. Lett.* **26**, 445 (1971).
- [42] T. Suzuki, private communication.

- [43] G. F. Bertsch and O. Scholten, *Phys. Rev.* **C25**, 804 (1982).
- [44] H. De Vries, C. W. De Jager, and C. De Vries, *Atom. Nucl. Data. Tabl.* **36**, 495 (1987).
- [45] C. W. De Jager, H. De Vries, and C. De Vries, *Atom. Nucl. Data. Tabl.* **14**, 479 (1974).
- [46] R. D. Smith and J. Wambach, *Phys. Rev.* **C36**, 2704.
- [47] J. D. Bjorken and S. D. Drell, "Relativistic Quantum Mechanics," McGraw-hill, New York, 1964.
- [48] Y. Miyama and T. Suzuki, RCNP (Osaka), Ann.Rept., 1991, p.115 (1992).

Appendix

A Response function by the Fermi gas model

In a non-interacting Fermi gas model, the wave function is given by

$$|F\rangle \equiv \prod_{p < k_F, s} b_{ps}^\dagger |\text{vacuum}\rangle, \quad (\text{A-1})$$

where b_{ps}^\dagger is the creation operator of the nucleon with momentum p and spin s . The response function W with respect to energy and momentum transfer $q \equiv (q, \omega)$ is defined as:

$$W(q) \equiv \mathcal{N} \int d^4x e^{iqx} \langle F | \hat{\rho}(x) \hat{\rho}(0) | F \rangle, \quad (\text{A-2})$$

where \mathcal{N} is a normalization constant, x is equivalent to (t, \vec{x}) , and $\hat{\rho}$ is a density operator. The density operator with respect to x is defined as

$$\hat{\rho}(x) \equiv \hat{\rho}(x) - \rho_0, \quad (\text{A-3})$$

where

$$\begin{aligned} \hat{\rho}(x) &= : \psi^\dagger(x) \psi(x) :, \\ \rho_0 &= \langle F | \hat{\rho}(x) | F \rangle. \end{aligned} \quad (\text{A-4})$$

$\psi(x)$ is a nucleon field operator.

A.1 Non-relativistic kinematics

In a non-relativistic formulation, a free nucleon field operator is expanded with respect to the creation operator as,

$$\begin{aligned} \psi(x) &= \sum_s \int d^3\vec{p} \varphi_{ps}(x) b_{ps}, \\ \varphi_{ps}(x) &= (2\pi)^{-3/2} \exp(-ipx) \chi_s, \end{aligned} \quad (\text{A-5})$$

where p is equivalent to (E_p, \vec{p}) and χ_s is a Pauli spinor. The density operators $\hat{\rho}$ and ρ_0 are therefore calculated as

$$\begin{aligned} \hat{\rho} &= \sum_{s, s'} \int d^3\vec{p} d^3\vec{p}' \varphi_{ps'}^*(x) \varphi_{ps}(x) b_{ps}^\dagger b_{p's'}, \\ \rho_0 &= \langle F | \hat{\rho}(x) | F \rangle \\ &= \sum_s \int d^3\vec{p} \Theta(k_F - p) \\ &= \frac{k_F^3}{3\pi^2}, \end{aligned} \quad (\text{A-6}) \quad (\text{A-7})$$

with the help of,

$$\langle F | b_{p's'}^\dagger b_{ps} | F \rangle = \delta(\vec{p} - \vec{p}') \delta_{s, s'} \Theta(k_F - p). \quad (\text{A-8})$$

$\Theta(x)$ is the theta function and defined as

$$\Theta(x) = \begin{cases} 1, & (x \geq 0) \\ 0, & (x < 0) \end{cases} \quad (\text{A-9})$$

Consequently, the non-relativistic response function W_{NR} is calculated as,

$$\begin{aligned} W_{NR}(q) &= \mathcal{N} \int d^4x e^{iqx} \sum_{s_1, s'_1, s_2, s'_2} \int \frac{d\vec{p}_1 d\vec{p}'_1 d\vec{p}_2 d\vec{p}'_2}{(2\pi)^6} e^{-i(p'_2 - p_2)x} \delta_{s_1, s'_1} \delta_{s_2, s'_2} \\ &\quad \times \langle F | b_{p_2 s_2}^\dagger b_{p'_2 s'_2}^\dagger b_{p'_1 s'_1}^\dagger b_{p_1 s_1} | F \rangle_{p_1 \neq p'_1, p_2 \neq p'_2}. \end{aligned} \quad (\text{A-10})$$

The condition $p_1 \neq p'_1, p_2 \neq p'_2$ originates from the subtraction of ρ_0 in the density operator which is given by Eq. A-7. Analogous to Eq. A-8, the density operator is substituted to one δ function and two Θ functions as

$$\begin{aligned} W_{NR}(q) &= \mathcal{N} \int d^4x \sum_s \int \frac{d\vec{p} d\vec{p}'}{(2\pi)^6} e^{-i(q+p-p')x} \Theta(k_F - p) \Theta(p' - k_F) \\ &= \frac{2\mathcal{N}}{4\pi^2} \int d\vec{p} d\vec{p}' \delta^4(q + p - p') \Theta(k_F - p) \Theta(p' - k_F) \\ &= \frac{\mathcal{N}}{2\pi^2} \int d\vec{p} \delta(\omega + E_p - E_{p+q}) \Theta(k_F - |\vec{p}|) \Theta(|\vec{p} + \vec{q}| - k_F), \end{aligned} \quad (\text{A-11})$$

where E_p is defined by $\frac{\vec{p}^2}{2m}$. The Pauli blocking effect is provided by the two Θ functions. The former Θ function in Eq. A-11 indicates the initial state in which the nucleon in the nucleus has momentum \vec{p} less than the Fermi momentum k_F of the nucleus. In the final state, the scattered nucleon needs to have the momentum larger than the Fermi momentum, which is described in the latter Θ function.

The integration can be done analytically. Then, the response function is evaluated as

$$W_{NR}(q) = \begin{cases} \frac{3\omega_f}{\omega_W^3} \omega, & (|\omega - \omega_f| < \omega_W, |\omega + \omega_f| < \omega_W : \text{I}) \\ \frac{3}{4\omega_W} \left\{ 1 - \left(\frac{\omega - \omega_f}{\omega_W} \right)^2 \right\}, & (|\omega - \omega_f| < \omega_W, |\omega + \omega_f| > \omega_W : \text{II}) \\ 0, & (|\omega - \omega_f| > \omega_W : \text{III}) \end{cases} \quad (\text{A-12})$$

where the energy transfer and the energy width are defined as

$$\omega_f \equiv \frac{q^2}{2m}, \quad (\text{A-13})$$

$$\omega_W \equiv \frac{q k_F}{m}. \quad (\text{A-14})$$

The normalization factor \mathcal{N} is determined by

$$\int d\omega W_{NR} \rightarrow 1 \quad \text{when} \quad q \rightarrow \infty. \quad (\text{A-15})$$

The top expression (I) corresponds to the region with the Pauli blocking effect while the middle expression (II) corresponds to the region without the Pauli blocking effect. Exemplified spectra of the response function are shown in Fig. A-1.

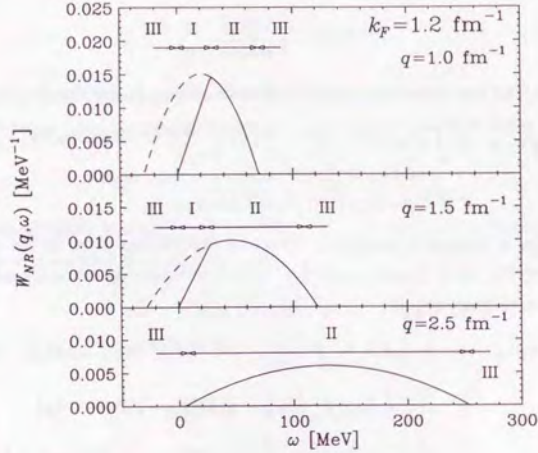


Fig. A-1: The responses calculated with the non-relativistic kinematics are shown for several q conditions of $q < k_F$ (top), $k_F < q < 2k_F$ (middle), and $2k_F < q$ (bottom). Regions of "I", "II", and "III" correspond to each expression in Eq. A-12. Dashed lines indicate responses when Pauli blocking effect is not considered.

A.2 Relativistic kinematics

In a relativistic formulation, the equation A-5 which describes the free nucleon field operator is modified as

$$\psi(\mathbf{x}) = \sum_s \int d\vec{p} \sqrt{\frac{m}{E_p}} [u(p, s) \varphi_{ps}(\mathbf{x}) b_{ps} + v(p, s) \varphi_{ps}^*(\mathbf{x}) d_{ps}^\dagger], \quad (\text{A-16})$$

where d^\dagger is the creation operator of anti-nucleon and u, v are Dirac spinors. The spinors u, v satisfy the following equations:

$$(\not{p} - m)u(p, s) = 0, \quad (\text{A-17})$$

$$(\not{p} + m)v(p, s) = 0, \quad (\text{A-18})$$

$$\bar{u}(p, s)u(p, s) = 1 = -\bar{v}(p, s)v(p, s), \quad (\text{A-19})$$

where

$$u(p, s) = \sqrt{\frac{E_p + m}{2m}} \begin{pmatrix} 1 & \chi_s \\ \vec{\sigma} \cdot \vec{p} & E_p + m \end{pmatrix} \chi_s, \quad (\text{A-20})$$

and $\vec{\sigma}$ is the Pauli spin matrix and χ_s is the Pauli spinor. The density operator becomes

$$\hat{\rho}(\mathbf{x}) = \psi^\dagger(\mathbf{x})\psi(\mathbf{x}) \quad (\text{A-21})$$

$$\begin{aligned} &= \sum_{s, s'} \int d\vec{p} d\vec{p}' \sqrt{\frac{m^2}{E_p E_{p'}}} [\varphi_{p's'}^*(\mathbf{x}) \varphi_{ps}(\mathbf{x}) u^\dagger(p', s') u(p, s) b_{p's'}^\dagger b_{ps} \\ &\quad + \varphi_{p's'}(\mathbf{x}) \varphi_{ps}^*(\mathbf{x}) v^\dagger(p', s') v(p, s) d_{p's'} d_{ps}^\dagger \\ &\quad + \varphi_{p's'}^*(\mathbf{x}) \varphi_{ps}^*(\mathbf{x}) u^\dagger(p', s') v(p, s) b_{p's'}^\dagger d_{ps}^\dagger \\ &\quad + \varphi_{p's'}(\mathbf{x}) \varphi_{ps}(\mathbf{x}) v^\dagger(p', s') u(p, s) d_{p's'} d_{ps}]. \end{aligned} \quad (\text{A-22})$$

$b^\dagger d^\dagger$ and db terms are vanished in subtracting vacuum components, which is shown as

$$\begin{aligned} \langle F | \hat{\rho}(\mathbf{x}) \hat{\rho}(0) | F \rangle &= \langle F | (\hat{\rho}(\mathbf{x}) - \rho_0(\mathbf{x})) (\hat{\rho}(0) - \rho_0(0)) | F \rangle \\ &= \langle F | \hat{\rho}(\mathbf{x}) \hat{\rho}(0) | F \rangle - \langle F | \hat{\rho}(\mathbf{x}) | F \rangle \langle F | \hat{\rho}(0) | F \rangle \\ &\quad - \langle F | \hat{\rho}(0) | F \rangle \langle F | \hat{\rho}(\mathbf{x}) | F \rangle + \langle F | \hat{\rho}(\mathbf{x}) | F \rangle \langle F | \hat{\rho}(0) | F \rangle \\ &= \langle F | \hat{\rho}(\mathbf{x}) \hat{\rho}(0) | F \rangle - \langle F | \hat{\rho}(\mathbf{x}) | F \rangle \langle F | \hat{\rho}(0) | F \rangle. \end{aligned} \quad (\text{A-23})$$

Consequently, the response function is given by

$$\begin{aligned} W(q) &= \mathcal{N} \int d^4x \sum_{s, s'} \int \frac{d\vec{p}_1 d\vec{p}_1' d\vec{p}_2 d\vec{p}_2'}{(2\pi)^6} \sqrt{\frac{m^4}{E_{p_1} E_{p_1'} E_{p_2} E_{p_2'}}} e^{-i(\mathbf{p}_1' - \mathbf{p}_1) \cdot \mathbf{x}} \\ &\quad \times u^\dagger(p_1', s_1') u(p_1, s_1) u^\dagger(p_2, s_2) u(p_2', s_2') \langle F | b_{p_2 s_2}^\dagger b_{p_2' s_2'}^\dagger b_{p_1 s_1}^\dagger b_{p_1' s_1'} | F \rangle. \end{aligned} \quad (\text{A-24})$$

The Pauli Blocking effects are represented in the last bra-ket:

$$\langle F | b_{p_2 s_2}^\dagger b_{p_2' s_2'}^\dagger b_{p_1 s_1}^\dagger b_{p_1' s_1'} | F \rangle = \delta(p_2 - p_1') \delta(p_2' - p_1) \Theta(k_F - p) \Theta(p' - k_F). \quad (\text{A-25})$$

Thus,

$$W(q) = \mathcal{N} \int d^4x \int \frac{d\vec{p} d\vec{p}'}{(2\pi)^6} \frac{m^2}{E_p E_{p'}} e^{i(\mathbf{q} + \mathbf{p} - \mathbf{p}') \cdot \mathbf{x}} \Theta(k_F - p) \Theta(p' - k_F) \times \mathcal{M}, \quad (\text{A-26})$$

where

$$\begin{aligned} \mathcal{M} &= \sum_{s, s'} u^\dagger(p', s') u(p, s) u^\dagger(p, s) u(p', s') \\ &= \sum_{s, s'} \bar{u}' \gamma_0 u \bar{u} \gamma_0 u' \\ &= \text{Tr} \left(\frac{\not{p}' + m}{2m} \gamma_0 \frac{\not{p} + m}{2m} \gamma_0 \right) \\ &= \frac{1}{m^2} \{ 2E_{p'} E_p - \mathbf{p}' \cdot \mathbf{p} + m^2 \} \\ &= \frac{1}{m^2} (E_{p'} E_p + \vec{p}' \cdot \vec{p} + m^2) \\ &= \frac{1}{2m^2} \{ (2E_p + \omega)^2 - \vec{q}^2 \}. \end{aligned} \quad (\text{A-27})$$

The response function becomes:

$$W(q) = \frac{N}{4\pi^2} \int d\vec{p} \frac{(2E_p + \omega)^2 - \vec{q}^2}{E_p} \Theta(E_F - E_p) \Theta(E_p + \omega - E_F) \times \delta(2E_p\omega - 2\vec{p} \cdot \vec{q} - Q^2) \quad (\text{A-28})$$

$$= \frac{N}{4\pi^2} \int_0^\infty p dp \frac{(2E_p + \omega)^2 - \vec{q}^2}{E_p} \Theta(E_F - E_p) \Theta(E_p + \omega - E_F) \times \int_{-1}^1 dx \delta(x - \frac{2E_p\omega - Q^2}{2pq}), \quad (\text{A-29})$$

where Q^2 is defined as $Q^2 \equiv q^2 - \omega^2$. In order to satisfy the equation $\int \delta dx = 1$, the following conditions are required.

$$\begin{aligned} -1 &< \frac{2E_p\omega - Q^2}{2pq} < 1, \\ \rightarrow Q^2 - 2pq &< 2E_p\omega < Q^2 + 2pq. \end{aligned} \quad (\text{A-30})$$

i) In the case of $Q^2 > 2pq$, this expression is equivalent to:

$$\begin{aligned} Q^2 &> 2pq, \\ \rightarrow q(q - 2p) &> \omega^2. \end{aligned} \quad (\text{A-31})$$

Therefore the condition $q > 2p$ is required. The formula A-30 becomes:

$$\begin{aligned} (Q^2 - 2pq)^2 &< 4E_p^2\omega^2 < (Q^2 + 2pq)^2 \\ \rightarrow (2p - q)^2 &< \Delta^2 < (2p + q)^2, \end{aligned} \quad (\text{A-32})$$

where Δ is defined by

$$\Delta = \omega \sqrt{1 + 4m^2/Q^2}. \quad (\text{A-33})$$

Combined with Eq. A-31, the condition is denoted by

$$\frac{\omega^2}{q} < q - 2p < \Delta < q + 2p \quad (\text{A-34})$$

$$\frac{|\Delta - q|}{2} < p < \frac{Q^2}{2q}. \quad (\text{A-35})$$

ii) In the case of $2pq > Q^2 > 0$, the formula A-30 becomes:

$$\begin{aligned} 0 &< 4E_p^2\omega^2 < (Q^2 + 2pq)^2, \\ \rightarrow \Delta &< q + 2p. \end{aligned} \quad (\text{A-36})$$

The condition is therefore given by

$$\begin{aligned} p &> \frac{\Delta - q}{2}, \\ p &> \frac{Q^2}{2q}. \end{aligned} \quad (\text{A-37})$$

From i) and ii) considerations, the response function is given by

$$W(q) = \frac{N}{4\pi^2} \int_0^\infty dE \{ (2E + \omega)^2 - \vec{q}^2 \} \Theta(E_F - E) \Theta(E + \omega - E_F) \Theta(E - E_m), \quad (\text{A-38})$$

where E_m is defined by

$$E_m = \sqrt{m^2 + k_m^2}. \quad (\text{A-39})$$

$$k_m = \frac{|\Delta - q|}{2}. \quad (\text{A-40})$$

From the equation A-38, the response function for relativistic Fermi gas is expressed by

$$W(q) = \begin{cases} \frac{3}{4k_F^3} \frac{1}{2q} \left[\frac{4}{3} E^3 + 2\omega E^2 - Q^2 E \right]_{\min(E_F - \omega, E_m)}^{E_F}, & (E_m < E_F) \\ 0, & (E_m > E_F) \end{cases} \quad (\text{A-41})$$

$$= \begin{cases} \frac{3\omega_f}{\omega_W^3} \omega \left(1 + \frac{12k_F^2 + \omega^2 - 3q^2}{12m^2} \right), & (E_F - \omega > E_m) : \text{I} \\ \frac{1}{2k_F^3 q} \left\{ (E_F + \frac{1}{2}\omega)(E_F + \frac{1}{2}\omega + \frac{\sqrt{3}}{2}q)(E_F + \frac{1}{2}\omega - \frac{\sqrt{3}}{2}q) \right. \\ \quad \left. - q^3 \left(\frac{m^2}{Q^2} - \frac{1}{2} \right) \sqrt{\frac{m^2}{Q^2} + \frac{1}{4}} \right\} \\ \quad \times \left\{ 1 - \frac{m^2}{k_F^2 \{ \omega \sqrt{4m^2 + Q^2} + qQ \}^2} \left(\omega - \frac{Q^2}{2m} \right)^2 \left(\omega + \frac{Q^2}{2m} \right)^2 \right\} \\ \quad (E_F > E_m > E_F - \omega) : \text{II} \\ 0, & (E_m > E_F) : \text{III} \end{cases} \quad (\text{A-42})$$

This equation becomes equivalent to the non-relativistic formula A-10 in the limit of

$$\Delta = \omega \sqrt{1 + \frac{4m^2}{Q^2}} \rightarrow \frac{2m\omega}{q}. \quad (\text{A-43})$$

The result of the FGM calculation with the relativistic kinematics are shown in Fig. 4-3. The positions are located at higher ω than ω_f , which is shown in Fig. 4-4.

B Projectile energy dependence of peak shifts by the PWIA calculation

In this appendix we describe the energy dependence of the peak positions of the calculation described in section 4.3. Fig. B-1, 4-11, and B-3 show the differential cross sections for the $p + p$ and $n + p$ reactions in the center of mass frame with respect to the scattering angle (upper frame) around laboratory energies of 200, 400, and 800 MeV, respectively. In addition, the differential cross sections for the $p(p,p)p$, $n(p,p)n$, and $n(p,n)p$ reactions in the laboratory frame are shown.

The differential cross section for the $p + p$ reaction is symmetric with respect to $\theta_{cm} = 90^\circ$ at all energies because of scattering between identical particles. For the $n + p$ reaction, on the contrary, the shape of the differential cross section deviates from the symmetrical shape above 300 MeV.

The laboratory angle from 0° to 90° corresponds to the center of mass angle from 0° to 180° for both the $p(p,p)p$ and $n(p,p)n$ reactions. For the $n(p,n)p$ reaction, the laboratory angle from 0° to 90° corresponds to the center of mass angle from 180° to 0° because direction of the Lorentz boost is opposite to that for the $n(p,p)n$ reaction.

Thus the non-symmetric shape for the $n + p$ results in the difference of peak position of the quasi elastic scattering between the (p,n) and (p,p') reactions.

At 400 and 800 MeV, large differences of the peak positions between the (p,n) and (p,p') reaction are indicated.

For example at $\theta_{lab} = 20^\circ$, the difference is more than 10 MeV. It is noticeable that the difference does not cause the shift upward for the (p,n) reaction but the shift downward for the (p,p') reaction. At 200 MeV, on the contrary, small differences occur.

These features will be confirmed by the comparison of the peak position using the (p,p') and (p,n) quasi elastic scattering spectra at 200 MeV or lower.

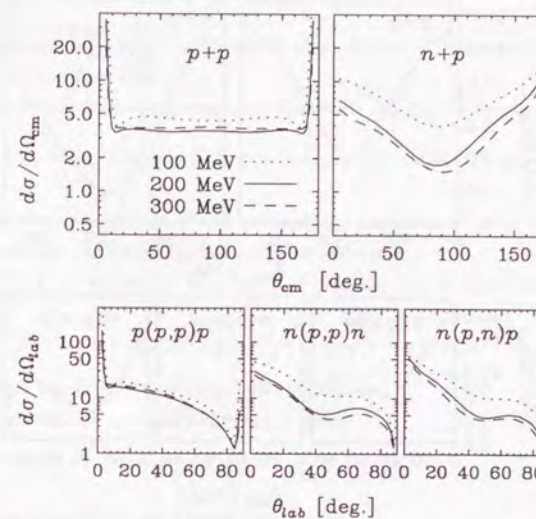


Fig. B-1: Angular distribution of the NN cross section at 100, 200, and 300 MeV.

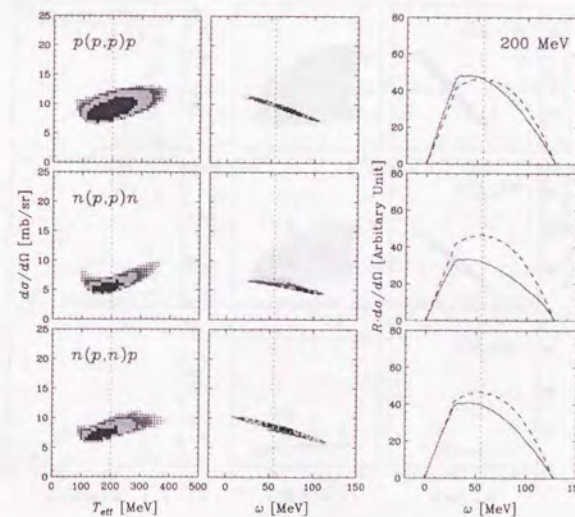


Fig. B-2: T_{eff} and ω dependence of the NN cross sections at 200 MeV and $q = 1.65 \text{ fm}^{-1}$.

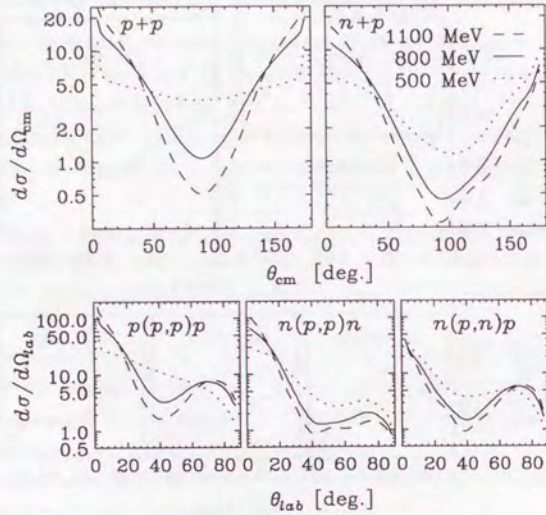


Fig. B-3: Angular distribution of the NN cross section at 500, 800, and 1100 MeV.

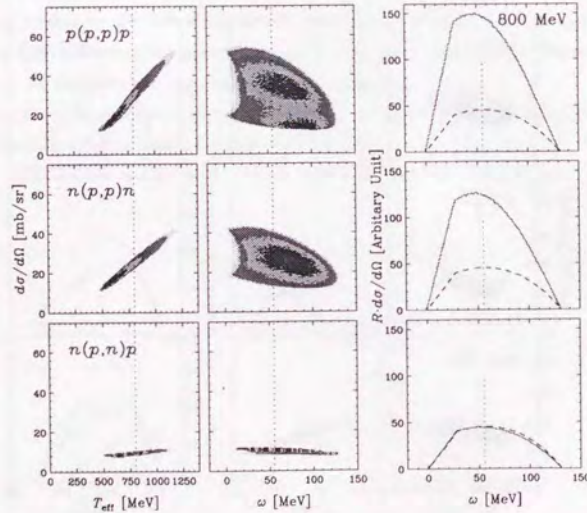


Fig. B-4: Same figure with B-2, but bombarding energy is 800 MeV.

C Parameterization of NN amplitude

We use two representations for the NN amplitude in section 4. In this appendix we show the relation between them.

With the notation of Bystricky, Lehar, and Winternitz [38] the NN amplitude is given by

$$\tilde{t} = \frac{1}{2} \left\{ a + b + (a-b)\vec{\sigma}_1 \cdot \hat{n}\vec{\sigma}_2 \cdot \hat{n} + (c+d)\vec{\sigma}_1 \cdot \hat{m}\vec{\sigma}_2 \cdot \hat{m} + (c-d)\vec{\sigma}_1 \cdot \hat{l}\vec{\sigma}_2 \cdot \hat{l} + ie(\vec{\sigma}_1 + \vec{\sigma}_2) \cdot \hat{n} \right\} \quad (C-1)$$

The parameters depend on isospin T and are explicitly denoted as a^T, b^T, c^T, d^T and e^T . Thus the free NN scattering can be parameterized by 10 parameters.

In the work by J. A. McNeil, L. Ray, and S. J. Wallace, on the other hand, They use the notation of

$$\tilde{t} = t_S + t_V \gamma_\mu \gamma^\mu + t_P \gamma_5 \gamma^5 + t_A \gamma_\mu \gamma_5 \gamma^\mu \gamma^5 + t_T \sigma_{\mu\nu} \sigma^{\mu\nu}. \quad (C-2)$$

These parameters also depend on isospin T in this notation.

The two representations are related by the equation:

$$\langle u'_1 u'_2 | \tilde{t} | u_1 u_2 \rangle = \langle \chi'_1 \chi'_2 | \tilde{t} | \chi_1 \chi_2 \rangle. \quad (C-3)$$

This can be written explicitly using matrix notation as

$$\begin{bmatrix} a \\ b \\ c \\ d \\ e \end{bmatrix} = \frac{im^2}{8\pi E_c} \begin{bmatrix} \cos \theta & \cos \theta & \cos \theta & -\cos \theta & -4 \sin \theta \\ 1 & -1 & 1 & 1 & 0 \\ -1 & 1 & 1 & 1 & 0 \\ 1 & 1 & -1 & 1 & 0 \\ -i \sin \theta & -i \sin \theta & -i \sin \theta & i \sin \theta & -4i \cos \theta \end{bmatrix} \times \begin{bmatrix} \alpha & e\alpha + p\beta & 0 & p\alpha + e\beta & -2\beta \\ -e\gamma & -\gamma & -p\gamma & -\delta & 2(p+e)\delta \\ \alpha & (p+e)\alpha & 0 & -(p+e)\alpha & 2\alpha \\ e\gamma & \gamma & -p\gamma & -\gamma & 2\gamma \\ -\epsilon & -\epsilon & 0 & \epsilon & -2\epsilon \end{bmatrix} \begin{bmatrix} t_S \\ t_V \\ t_P \\ t_A \\ t_T \end{bmatrix}. \quad (C-4)$$

Table C-1: Parameters in matrix elements of Eq. C-4.

e	$= E_c^2 / m^*$
p	$= k_c^2 / m^* = e - 1$
α	$= \cos^2 \frac{\theta}{2}$
β	$= 1 + \sin^2 \frac{\theta}{2}$
γ	$= \sin^2 \frac{\theta}{2}$
δ	$= 1 + \cos^2 \frac{\theta}{2}$
ϵ	$= \frac{E_c}{m^*} \sin \frac{\theta}{2} \cos \frac{\theta}{2}$

The energy $E_c = \sqrt{m^2 + k_c^2}$ and scattering angle θ are represented in the center of mass frame of the two nucleon system. The first matrix gives the transformation from the helicity representation to the Bystricky representation. In the second matrix, the parameters e and p depend on the energy and momentum while the parameters $\alpha, \beta, \gamma, \delta$, and ϵ depend on the scattering angles listed in Table C-1.

D Expansion of the Glauber theory

The total cross section σ is expanded as the summation of n -step cross section as

$$\sigma = \sigma^{(1)} + \sigma^{(2)} + \dots + \sigma^{(A)}. \quad (D-1)$$

Each component is approximately denoted by

$$\begin{aligned} \sigma^{(n)} &= A C_n \int d^2 b (\chi_{pp} + \chi_{pn})^n \{1 - (\chi_{pp} + \chi_{pn})\}^{(A-n)} \\ &\simeq \int d^2 b \frac{(\chi_{pp} + \chi_{pn})^n}{n!} e^{-(\chi_{pp} + \chi_{pn})}. \end{aligned} \quad (D-2)$$

The $n=1$ term is identical to Eq. 4-8.

In order to investigate the probe dependence of the multi-step contribution, we examine the ratio $\sigma^{(2)}/\sigma^{(1)}$ for the (p, n) and (p, p') reactions using Eq. D-2. The single-step cross sections $\sigma^{(1)}$ for the (p, p') and (p, n) reaction are described by

$$\begin{aligned} \sigma_{(p, p')}^{(1)} &= \int d^2 b (\chi_{pp} + \chi_{pn}) e^{-(\chi_{pp} + \chi_{pn})}, \\ \sigma_{(p, n)}^{(1)} &= \int d^2 b \chi_{pn} e^{-(\chi_{pp} + \chi_{pn})}. \end{aligned} \quad (D-3)$$

The two-step cross section $\sigma^{(2)}$ are described by

$$\begin{aligned} \sigma_{(p, p')}^{(2)} &= \int d^2 b \frac{(\chi_{pp} + \chi_{pn})^2}{2} e^{-(\chi_{pp} + \chi_{pn})}, \\ \sigma_{(p, n)}^{(2)} &= \int d^2 b \left(\frac{1}{2} \chi_{pn}^2 + \chi_{pn} \chi_{pp} \right) e^{-(\chi_{pp} + \chi_{pn})}. \end{aligned} \quad (D-4)$$

In the $\sigma^{(2)}$ for the (p, n) reaction only the $\chi_{pp}^2/2$ component is excluded because no neutrons is detected from the component. Using the averaged values, which are denoted as $\bar{\chi}$ and so on, the ratio can be derived by

$$\begin{aligned} \frac{\sigma_{(p, p')}^{(2)}}{\sigma_{(p, p')}^{(1)}} &= \frac{\frac{1}{2} (\bar{\chi}_{pn} + \bar{\chi}_{pp})^2}{\bar{\chi}_{pn} + \bar{\chi}_{pp}} \simeq \frac{1}{2} \bar{\chi}_{pn} + \frac{1}{2} \bar{\chi}_{pp}, \\ \frac{\sigma_{(p, n)}^{(2)}}{\sigma_{(p, n)}^{(1)}} &= \frac{\frac{1}{2} \bar{\chi}_{pn}^2 + \bar{\chi}_{pn} \bar{\chi}_{pp}}{\bar{\chi}_{pn}} \simeq \frac{1}{2} \bar{\chi}_{pn} + \bar{\chi}_{pp} \end{aligned} \quad (D-5)$$

Consequently, it is found that the ratio of the (p, n) reaction is larger than that of the (p, p') reaction. The two-step component relative to the single-step component is expected to appear larger for the (p, n) reaction than the (p, p') reaction. In this simple model we ignore cross sections for the NN inelastic channel, such as π meson production or Δ excitation, which are opened with initial proton energy above 280 MeV. When the inelastic cross sections are taken in account, the equation 4-8 needs to be modified as

$$\begin{aligned} A_{\text{eff}} &= \frac{1}{\sigma_{\text{elastic}}} \int_0^\infty d^2 b \chi_N(b) e^{-(\chi_N(b) + \chi_{N^*}(b))}, \\ \chi_N(b) &= \int dz \sigma_{\text{elastic}} \rho(r), \\ \chi_{N^*}(b) &= \int dz \sigma_{\text{inelastic}} \rho(r). \end{aligned} \quad (D-6)$$

One must be more careful in this energy region because the fraction of the single-step scattering becomes smaller, which originates from the factor $e^{-(\chi_N(b) + \chi_{N^*}(b))}$.

E Other results : $^{13}\text{C}(p, n)$ reaction

We compared the energy spectra of the $^{13}\text{C}(p, n)$ reaction with those of the $^{12}\text{C}(p, n)$ reaction, which is shown in Fig. E-1. As is shown in the top frame of the figure, the cross section of ^{13}C is identical with that of ^{12}C at energy transfer greater than 90 MeV at 20° . Differences at energy transfer less than 90 MeV comes from one of the neutrons in ^{13}C . We describe this neutron which makes the difference as n^* . The $n^*(p, n)$ reactions are shown in the middle frame of the Fig. E-1. The energy distribution of the reaction is located around the expected position by kinematics for free NN scattering. Consequently, the peak position for the $^{13}\text{C}(p, n)$ reaction is influenced by the valence neutron. The peak shift is therefore is much smaller than that of the $^{12}\text{C}(p, n)$ reaction.

The difference between the $^{13}\text{C}(p, p')$ reaction and the $^{12}\text{C}(p, p')$ reaction is less clearly identified than that of the (p, n) reaction. The difference for the (p, n) reaction is due to one nucleon out of seven neutrons while the difference for the (p, p') reaction is due to one nucleon out of 13 nucleons. Although quality is poor, the peak position for the $n^*(p, p')$ reaction is shifted to lower ω .

As one of methods to investigate the motion of nucleons in the nucleus, the measurements of cross section and analyzing power for the (p, p') and (p, n) QES is strongly suggested. In order to clarify this issue, sufficiently small statistics uncertainty is required especially for the (p, p') reaction.

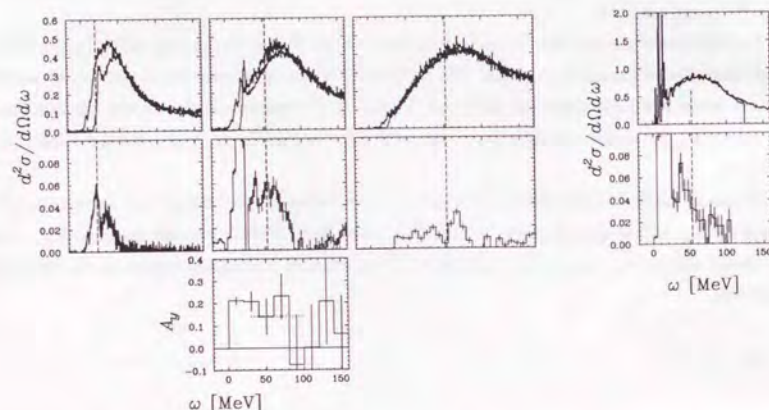


Fig. E-1: Comparison of the cross sections for the ^{13}C and ^{12}C QES. Left seven frames indicate the (p, n) reaction while the right two frames indicate the (p, p') reaction. For the (p, n) reaction, the spectra for 12° , 20° , and 28° are shown from left to right. The top frames show the cross sections for the ^{13}C and ^{12}C . The differences are derived and shown in the middle frames. Vertical dashed line indicates the positions of the kinematic of the NN scattering. The peak positions of the differences are consistent with that of the NN kinematics.

Acknowledgement

I am deeply indebted to many people who offered me encouragement, stimulating discussions, decisive suggestions and excellent technical supports in the course of the present investigation.

I wish to express my gratitude to my supervisor, Professor Hideyuki Sakai, who introduced me to this field. He has given me continuous supports, encouragement, advice, and discussions throughout the graduate course. Nothing could have delivered me the significant gains on physics and the experimental techniques than the discussions with him. I have called the discussions namely the "battles". I am also grateful to Dr. Hiroyuki Okamura for useful discussions not only on physics but on computer programming techniques as well. I wish to thank Professor Kichiji Hatanaka not only for discussions and suggestions on physics but also for continuous encouragement and general assistances in carrying out the experiments at RCNP.

Without their invaluable helps this work would not have been realized.

All of the work presented here have been done in collaboration with the members of the RCNP-E17/E58 collaboration. I acknowledge the aids of the collaborators; Professor Mark B. Greenfield, Professor Norihiko Koori, Professor Akira Okihana, Mr. Satoru Ishida, Dr. Naruhiko Sakamoto, Dr. Tomotsugu Wakasa, Mr. Tomohiro Uesaka, Mr. Yoshiteru Satou, Mr. Satoshi Fujita, Mr. Tetsuya Ohnishi, and Mr. Takamasa Nonaka. Especially, I would like to appreciate Dr. Tomotsugu Wakasa for his daily collaboration, friendship, and his support on data taking system at RCNP.

I would like to thank Professor Munetake Ichimura and Dr. Ken Kawahigashi for their useful advice and theoretical supports. I acknowledge Professor Toru Suzuki for his helpful suggestions and discussions. I also acknowledge Dr. Akira Oonishi and his collaborators for their suggestions. Thanks are due to Dr. Greg Hillhouse for his helpful advice.

Special thanks are due to all RCNP staffs and engineers for their warm-hearted encouragement not only throughout the experiments but also on the daily life. Firstly, I would like to thank to accelerator staffs for their kindness and their great efforts for providing stable beam. Especially my grateful thank is due to Professor Kazuhiko Hosono for his daily encouragement and useful advice. I am also indebted to Dr. Nobuyuki Matsuoka and Mr. Masato Yoshimura for their supports on the experiment using the spectrograph LAS. I wish to thank Professor Tetsuo Noro and Dr. Hidetoshi Akimune for helpful advice on the VDC counter. Also I would like to thank Mr. Masaru Yosoi, Dr. Yasuhiro Sakemi for discussions and their suggestions on the experiments.

I would like to thank people in RIKEN where I stayed for the analyses throughout my graduate student days. I am indebted to Dr. Yasushi Watanabe and Dr. Takashi Ichihara for their supports on computers and their computer code libraries. I am also indebted to Dr. Hiroyoshi Sakurai for his useful advice. I would like to express great regards to Dr. Nobuhisa Fukunishi and Mr. Naohito Inabe for their stimulating suggestions.

Numerical calculations were carried out with RCNPAX cluster system at RCNP and a RIKAXP cluster system at the Institute of Physical and Chemical Research (RIKEN).

I am indebted to Fellowships of the Japan Society for the Promotion of Science for Japanese Junior Scientists.

